

# PHOTOLUMINESCENCE STUDY OF NON-POLAR III-NITRIDE SEMICONDUCTORS

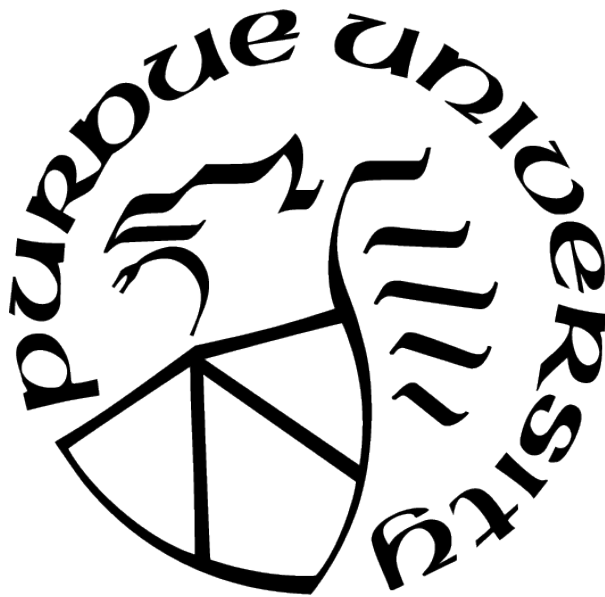
by  
Yang Cao

A Dissertation

*Submitted to the Faculty of Purdue University*

*In Partial Fulfillment of the Requirements for the degree of*

Doctor of Philosophy



Department of Physics and Astronomy

West Lafayette, Indiana

May 2022

**THE PURDUE UNIVERSITY GRADUATE SCHOOL  
STATEMENT OF COMMITTEE APPROVAL**

**Dr. Oana Malis, Chair**

Department of Physics and Astronomy

**Dr. Kenneth P Ritchie**

Department of Physics and Astronomy

**Dr. Luis Martin Kruczenski**

Department of Physics and Astronomy

**Dr. Yuli Lyanda-Geller**

Department of Physics and Astronomy

**Approved by:**

Dr. Gabor A. Csathy

## ACKNOWLEDGMENTS

I joined Professor Malis's research group in Spring 2017 to work on non-polar III-nitride semiconductors. I would like to thank her for her support during my doctoral research work. The completion of my research projects would not be possible without her guidance. I would also like to thank my committee members, Professor Kenneth P Ritchie, Professor Luis Martin Kruczenski, and Professor Yuli Lyanda-Geller for their valuable comments on my research work.

I had great pleasure to get to know and work with my lab mates, Trang Nguyen, Brandon Dzuba, Doctor Alexander Senichev, and Doctor Mohammadali Shirazi. I appreciate their friendship and encouragement to finish this dissertation.

Finally I would like to thank my family. As an international student who study and live alone overseas, their love and encouragement is always supportive during my doctoral study.

# TABLE OF CONTENTS

LIST OF TABLES . . . . .	7
LIST OF FIGURES . . . . .	8
ABBREVIATIONS . . . . .	11
ABSTRACT . . . . .	13
1 BASICS OF PHOTOLUMINESCENCE . . . . .	15
1.1 Kinetic description of recombination processes . . . . .	16
1.1.1 Monomolecular process . . . . .	18
1.1.2 Bimolecular process . . . . .	20
1.1.3 Multiple process . . . . .	23
1.2 Typical channels of radiative recombination . . . . .	26
1.2.1 Recombination of free electron-hole pairs (e-h) . . . . .	27
Direct bandgap . . . . .	27
Indirect bandgap . . . . .	30
1.2.2 Recombination of a free electron (hole) with a neutral acceptor (donor)(e- $A^0$ and $h-D^0$ ) . . . . .	32
1.2.3 Recombination of donor-acceptor pairs ( $D^0-A^0$ ) . . . . .	34
1.2.4 Recombination of free excitons (FE or X) . . . . .	36
1.2.5 Recombination of bound excitons . . . . .	42
Recombination of excitons bounded to ionized donors or acceptors ( $D^+-X$ or $A^--X$ ) . . . . .	43
Recombination of excitons bounded to neutral donors or acceptors ( $D^0-X$ or $A^0-X$ ) . . . . .	44
1.3 Experimental Setup . . . . .	44
1.3.1 Sample Placement . . . . .	45
1.3.2 Detector System . . . . .	46
Photomultiplier Tube . . . . .	46



	Avalanche Photodiode . . . . .	46
	Multichannel Detectors . . . . .	47
1.3.3	Signal Detection Methods . . . . .	47
	Phase-Synchronous Detection . . . . .	48
	Photon Counting . . . . .	48
1.3.4	Monochromators . . . . .	49
2	INTRODUCTION OF III-NITRIDE SEMICONDUCTORS . . . . .	54
2.1	Lattice Mismatch . . . . .	57
2.2	Internal Polarization Fields . . . . .	57
3	EXPERIMENTAL DETAILS . . . . .	61
3.1	Growth of nitrides . . . . .	61
3.2	Structural characterization of nitrides . . . . .	61
3.3	Steady state photoluminescence . . . . .	62
3.4	Time-resolved photoluminescence . . . . .	65
4	NON-POLAR INGAN THIN FILMS . . . . .	68
4.1	Effect of In composition on continuous-excitation PL signal . . . . .	69
4.2	Effect of temperature on continuous-excitation PL signal . . . . .	72
4.3	Summary . . . . .	76
5	NEARLY STRAIN-BALANCED NON-POLAR M-PLANE INGAN/ALGAN SUPERLATTICES . . . . .	77
5.1	Discussion of continuous-excitation PL spectra . . . . .	79
5.1.1	PL peak position . . . . .	80
5.1.2	Broadening of PL spectra . . . . .	83
5.1.3	Effect of temperature on continuous-excitation PL . . . . .	84
5.1.4	Defect band . . . . .	88
5.2	Carrier localization and recombination . . . . .	89
5.2.1	Carrier localization depth . . . . .	90
5.2.2	Thermal activation for non-radiative recombination . . . . .	93

5.2.3	Discussion of TRPL spectra . . . . .	95
5.3	Summary . . . . .	102
6	OUTLOOK OF FUTURE WORK . . . . .	104
6.1	Improvement of the growth for non-polar m-plane In containing heterostructures	104
6.1.1	Thick GaN buffer layer and InGaN underlayer . . . . .	104
6.1.2	Growth conditions for AlGaN barrier . . . . .	107
6.2	Summary . . . . .	109
	REFERENCES . . . . .	110
A	PL MEASUREMENT SETUP . . . . .	121
A.1	Sample placement . . . . .	121
A.2	Steady state PL measurement . . . . .	121
VITA	. . . . .	124

## LIST OF TABLES

4.1	A series of non-polar m-plane InGaN thin films. . . . .	68
4.2	PL energies of InGaN thin films at 80 K. . . . .	69
4.3	Calculated PL peaks at 80 K and estimated In compositions from experimental PL. . . . .	70
5.1	A series of m-plane InGaN/AlGaN superlattices. . . . .	77
5.2	Measured PL peak energies and FWHMs as well as calculated peak energies at 80 K for samples F-K. . . . .	79
5.3	Revised calculated PL peak for doped samples H, I, J and K at 80 K including exchange correction. . . . .	81

## LIST OF FIGURES

1.1	A typical recombination process resulting in photoluminescence in a bulk semiconductor. . . . .	15
1.2	An illustration of radiative and non-radiative recombination processes . . . . .	17
1.3	An illustration of a monomolecular recombination process. . . . .	18
1.4	An illustration of a bimolecular recombination process. . . . .	21
1.5	A monomolecular process and a bimolecular process present simultaneously. . .	23
1.6	A recombination process of free electron-hole pairs in a bulk direct bandgap semiconductor . . . . .	28
1.7	A recombination process of free electron-hole pairs in a bulk indirect bandgap semiconductor. . . . .	31
1.8	Recombination of a free hole with a neutral donor (left) and of a free electron with a neutral acceptor (right). . . . .	33
1.9	A diagram of a donor-acceptor pair. . . . .	35
1.10	Recombination of a donor-acceptor pair. . . . .	36
1.11	A diagram of a Wannier exciton in a 2D crystal. . . . .	37
1.12	A schematic of the dispersion curves of an exciton-polariton. . . . .	40
1.13	Czerny-Turner configuration. . . . .	50
1.14	The aperture ratio of a spectral device. . . . .	52
2.1	Band gap vs. lattice constant for III-nitride semiconductor materials [12] . . . .	54
2.2	GaN with a wurtzite structure. . . . .	55
2.3	An example of intersubband transition in a non-polar m-plane quantum well ( $\text{Al}_{0.22}\text{Ga}_{0.78}\text{N}/\text{In}_{0.12}\text{Ga}_{0.88}\text{N}$ ). Three electron energy states are confined in the conduction band. The conduction band edge is depicted by black line. The wavefunctions are offset by energy levels. . . . .	56
2.4	Schematic of the GaN c-plane and m-plane orientations. . . . .	58
2.5	Band structure of a quantum well ( $\text{AlN}/\text{GaN}$ ) grown on c-plane. The wavefunctions are offset by energy levels. . . . .	59
2.6	Band structure of a quantum well ( $\text{Al}_{0.22}\text{Ga}_{0.78}\text{N}/\text{In}_{0.12}\text{Ga}_{0.88}\text{N}$ ) grown on m-plane. The wavefunctions are offset by energy levels. . . . .	59
3.1	A diagram of the PL setup in our lab. . . . .	63
3.2	The polarization of the emitted light. . . . .	65

3.3	A diagram of a TRPL setup. . . . .	66
3.4	Faraday geometry. . . . .	66
4.1	PL spectra of InGaN thin films A-E at 80 K. The PL curves of samples A-E were reduced by a factor of 545, 1000, 17.8, 8.5, and 2.2, respectively. . . . .	70
4.2	Temperature dependence of PL spectra for sample B. . . . .	73
4.3	Temperature dependence of integrated PL intensity for sample B. . . . .	73
4.4	Temperature dependence of PL peak energy for sample B. . . . .	74
4.5	Temperature dependence of PL FWHM for sample B. The black interpolation line is a guide to the eye. . . . .	74
5.1	HAADF-STEM image of sample J. The darker layers are AlGaIn, while the lighter layers are InGaIn. . . . .	78
5.2	Sketch of structure for all samples. . . . .	79
5.3	Temperature dependence of PL peak position for sample H. . . . .	81
5.4	Polarized PL spectra at 80 K for sample H. . . . .	82
5.5	PL spectra at temperatures from 8.3K to 290K for sample G. . . . .	85
5.6	Temperature dependence curve of PL integrated intensity for sample G. . . . .	85
5.7	Temperature dependence curve of PL peak position for sample G. The red line is the calculation of the PL transition energy from Nextnano software package using self-consistent simulation for a InGaIn/AlGaIn superlattice which has similar QW and barrier thicknesses with sample G, and In composition of 17%. . . . .	86
5.8	Temperature dependence curve of PL FWHM for sample G. The red interpolation line is a guide to the eye. . . . .	87
5.9	PL spectra at temperatures from 8.3K to 290K for sample K. . . . .	88
5.10	Temperature dependence of FWHM for sample G (a) and sample H (b). Red lines are fitting curves based on the temperature dependence of total broadening (Eqn. (5.2)). . . . .	92
5.11	Arrhenius plot of IQE for sample G (a) and sample H (b). Red lines are fitting curves based on the relation of IQE and temperature (Eqn. (5.4)). . . . .	94
5.12	TRPL spectra for sample G. . . . .	96
5.13	TRPL spectra for sample H. . . . .	96
5.14	Temperature dependence of PL transient peak intensity for sample G and sample H. The lines are guides to the eye. . . . .	97
5.15	Temperature dependence of decay time $\tau_1$ and $\tau_2$ for sample G, and $\tau$ sample H. . . . .	97

5.16	The direction of magnetic field applied to the superlattices. . . . .	99
5.17	TRPL spectra in magnetic field for sample G. The inset is the magnetic field dependence of PL transient peak intensity. . . . .	100
5.18	TRPL spectra in magnetic field for sample H. The inset is the magnetic field dependence of PL transient peak intensity. . . . .	101
5.19	Magnetic field dependence of decay time $\tau_1$ and $\tau_2$ for sample G, and $\tau$ sample H. . . . .	101
6.1	PL spectra at temperatures from 8.3 K to 290 K for sample M. . . . .	105
6.2	Sketch of structure for sample L. . . . .	105
6.3	PL spectra at temperatures from 8.3 K to 290 K for sample L. . . . .	106
6.4	HAADF-STEM image of sample Z. The darker layers are AlGaN, while the lighter layers are InGaN. . . . .	108
6.5	PL spectra of samples X-Z at 80 K. The PL curves of samples X-Z were reduced by a factor of 250.63, 378.07, and 612.73, respectively. . . . .	108
A.1	A sample is mounted on the sample holder. . . . .	121
A.2	The setup for steady state PL measurement. . . . .	122
A.3	Empirical sample placement. . . . .	122
A.4	Connection of the temperature controller. . . . .	123

## ABBREVIATIONS

PL	photoluminescence
PMT	photomultiplier tube
CCD	charge-coupled device
SSPL	steady-state photoluminescence
TRPL	time-resolved photoluminescence
PLE	photoluminescence excitation spectroscopy
ODMR	optically detected magnetic resonance
e-h	radiative recombination of free electron-hole pairs
FWHM	full width at half maximum
$e-A^0$	radiative recombination of a free electron with a neutral acceptor
$h-D^0$	radiative recombination of a free hole with a neutral donor
$D^0-A^0$	radiative recombination of donor-acceptor pairs
FE or X	radiative recombination of free excitons
UPB	upper polariton branch
LPB	lower polariton branch
BE	bound exciton
$D^+-X$	recombination of excitons bounded to ionized donors
$A^--X$	recombination of excitons bounded to ionized acceptors
$D^0-X$	recombination of excitons bounded to neutral donors
$A^0-X$	recombination of excitons bounded to neutral acceptors
QW	quantum well
LED	light-emitting diodes
NRC	non-radiative recombination center
MBE	molecular beam epitaxy
PAMBE	plasma assisted molecular beam epitaxy
AFM	atomic force microscopy
XRD	x-ray diffraction
HRXRD	high-resolution x-ray diffraction

HAADF-STEM	high resolution high-angle annular dark-field scanning transmission electron microscopy
FIB	focused ion beam
MOCVD	metal organic chemical vapour deposition
LO	longitudinal-optical
IQE	internal quantum efficiency
MOVPE	metal organic vapour phase epitaxy
DLP	degree of linear polarization



## ABSTRACT

Nitride semiconductors are promising for applications in opto-electronic devices due to their wide band gap that is adjustable by appropriate choice of alloy composition. To date, many III-nitride devices have been demonstrated, such as light-emitting diodes, lasers, etc. Most opto-electronic devices make use of the optical transition from conduction band to valence band. Moreover, the large conduction band offset achieved by III-nitrides makes it possible to take advantage of transitions inside the conduction band or valence band, which provide much more freedom for band engineering.

Although many III-nitrides based opto-electronic devices have been invented and implemented in commercial use, there is still a need for more compact, rugged, higher efficiency devices with lower cost. Many challenges of III-nitride semiconductors are related to material defects, lattice mismatch and internal polarization fields. Photoluminescence is a convenient technique to characterize sample quality and optical properties. It does not destroy the samples or need any electrical contacts. Therefore, it is commonly used in qualitative analysis of III-nitrides.

This thesis focuses on non-polar m-plane III-nitrides structures, because this crystal orientation eliminates internal polarization fields in heterostructures. We first performed a photoluminescence study of a series of m-plane InGaN thin films with In compositions up to 24.5%. Evidence of large In composition fluctuations was observed. This inhomogeneity of In composition contributes to the non-monotonic temperature dependence of photoluminescence peak energy and linewidth. A large drop of internal quantum efficiency when temperature increases to room temperature was observed, which indicates the presence of a large number of non-radiative recombination centers. This is due to low temperature growth of InGaN by plasma assisted molecular beam epitaxy. The InGaN film with 11% has a linewidth close to theoretical calculations for InGaN with random In distribution, and much smaller than many reported polar c-plane InGaN films with comparable In compositions, which suggests improved material quality. This In composition was selected for the design of InGaN/AlGaN superlattices.

In order to avoid the disadvantage of strain buildup, we designed nearly strain-balanced non-polar m-plane InGaN/AlGaIn structures with In composition of about 9%. Steady-state photoluminescence and time-resolved photoluminescence were performed on these structures. A significant discrepancy between measured and calculated PL peak positions was observed. This is likely due to the In composition fluctuations and quantum confinement in quantum wells. The broadening mechanism of the PL in the superlattices was investigated. The low-temperature linewidth of undoped superlattices is comparable to many previously reported values for m-plane InGaN/GaN quantum wells. Similar to InGaIn films, the internal quantum efficiency drops dramatically when temperature reaches room temperature. Regions with high In compositions act as localization centers for excitons. An average localization potential depth of 21 meV was estimated for undoped superlattices. This small potential depth does not reduce the degree of polarization of emitted light, and contributes to the narrow linewidth. A fast decay time of 0.3 ns at 2 K was observed for both doped and undoped superlattices. This value is much smaller than that for polar c-plane InGaIn/GaN superlattices. The localization of excitons was found to be strong and not affected by magnetic field at low temperatures. Compared with undoped superlattices, the doping sheets reduce decay pathways of excitons in doped superlattices.

# 1. BASICS OF PHOTOLUMINESCENCE

Luminescence is the process of light emission by a material following excitation. Since external excitation is required, luminescence is not an equilibrium process. If the excitation source is electrical injection, this specific luminescence is called electroluminescence. If the excitation source is optical, the luminescence is called photoluminescence (PL).

A simple typical process of photoluminescence in a bulk semiconductor is shown in Figure 1.1. The electrons are excited from the valence band to the conduction band. Then they decay non-radiatively to the bottom of the conduction band. Finally, a radiative transition takes place when the electrons recombine with the holes in the valence band. The energy of the emitted photon is equal to the difference of the energies of the electron and hole before recombination. As we can see, the emitted photons can provide information about the band

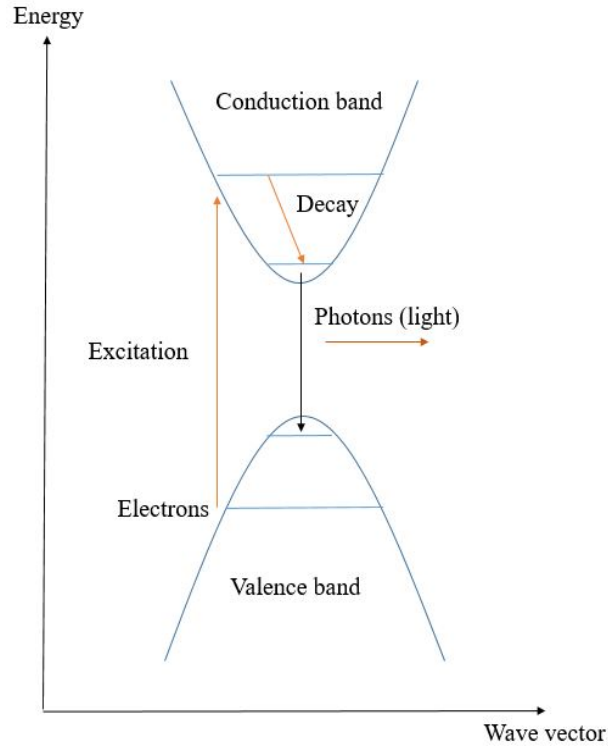


**Figure 1.1.** A typical recombination process resulting in photoluminescence in a bulk semiconductor.

structure of the material. Because of the non-radiative decay inside the conduction band,

the radiated photons have lower energies (i.e larger wavelength) compared with the absorbed photons. Therefore, the absorption spectrum and emission spectrum are always different [1].

## 1.1 Kinetic description of recombination processes

Typical photoluminescence spectroscopy includes steady-state photoluminescence (SSPL), time-resolved photoluminescence (TRPL), photoluminescence excitation spectroscopy (PLE), and optically detected magnetic resonance (ODMR). Here, we mainly discuss the processes involved in SSPL and TRPL.

SSPL is taken when the luminescence intensity stays constant after the excitation is switched on and after an initial equilibration time, while TRPL is taken after the excitation is turned off. They provide valuable information about the recombination processes and related recombination centers.

As mentioned at the beginning of this chapter, PL is a radiative recombination process. But this is not the only possible transition when an excitation is applied. In general, non-radiative recombination processes happen as well, where the emitted energy is commonly transformed into heat or vibrations of the crystal. For some specific material, the non-radiative recombination processes can also cause photochemical changes or even create a lattice defect [2]. In order to better describe the general recombination kinetic equations for PL, we will consider both radiative and non-radiative recombination processes (Figure 1.2) in the following discussion. Each recombination process is characterized by a lifetime. We can define the inverse number of it as the recombination rate, which is the transition probability per unit time. Thus the total recombination rate from an excited state to the ground state can be expressed as

$$\frac{1}{\tau} = \frac{1}{\tau_{nr}} + \frac{1}{\tau_r} \quad (1.1)$$

where the lifetime of the radiative and non-radiative recombination processes is represented by  $\tau_r$  and  $\tau_{nr}$ , respectively. Then, a term showing the luminescence efficiency, which is

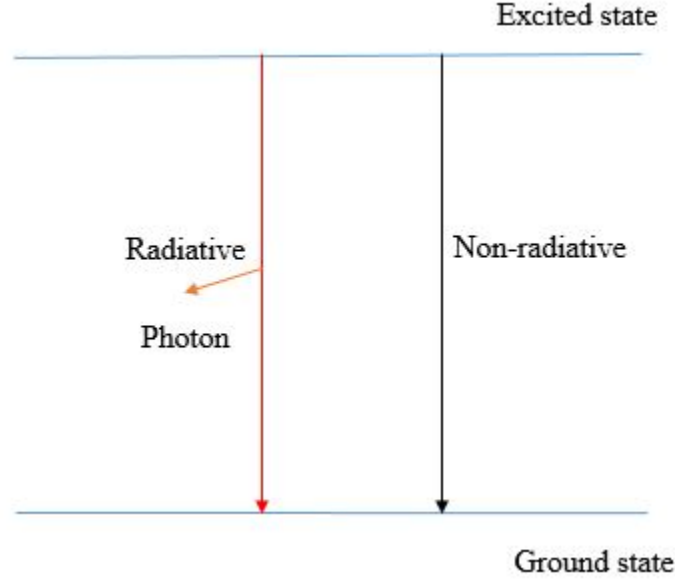


**Figure 1.2.** An illustration of radiative and non-radiative recombination processes

commonly referred to as quantum efficiency or luminescence quantum yield, can be defined as [2]

$$\eta = \frac{\frac{1}{\tau_r}}{\frac{1}{\tau_{nr}} + \frac{1}{\tau_r}} = \frac{\tau}{\tau_r} \quad (1.2)$$

The quantum efficiency is typically lower than 1. In general, a material which has a quantum efficiency of the order of 0.1 is called a strong luminescence material [2]. As discussed at the beginning of this chapter, most excited electrons experience a redistribution prior to the recombination with the holes. Therefore, if we consider the difference between the excitation energy  $h\nu_{ex}$  and energy of the luminescence photon  $h\nu_{lumi}$ , we can define the power efficiency as

$$\eta_{power} = \eta \frac{h\nu_{lumi}}{h\nu_{ex}} \quad (1.3)$$

So the power efficiency is lower than the quantum efficiency. It is not easy to directly measure the quantum efficiency. Instead, people usually measure the temperature dependence of the luminescence intensity, which is approximately proportional to the quantum efficiency.

So far we have covered the simplest recombination process for PL. In reality, the process may be much more complex. Next we will introduce the following common processes: monomolecular process, bimolecular process and multiple processes.

### 1.1.1 Monomolecular process

The monomolecular process is the recombination process occurring in localized luminescence centers. Most materials are not perfect and contain a number of defects and impurities. They always act as luminescence centers. Here we take as an example the recombination in impurity centers to discuss the kinetic equation of the monomolecular process. As shown in Figure 1.3, we can derive the following equation to describe the monomolecular process

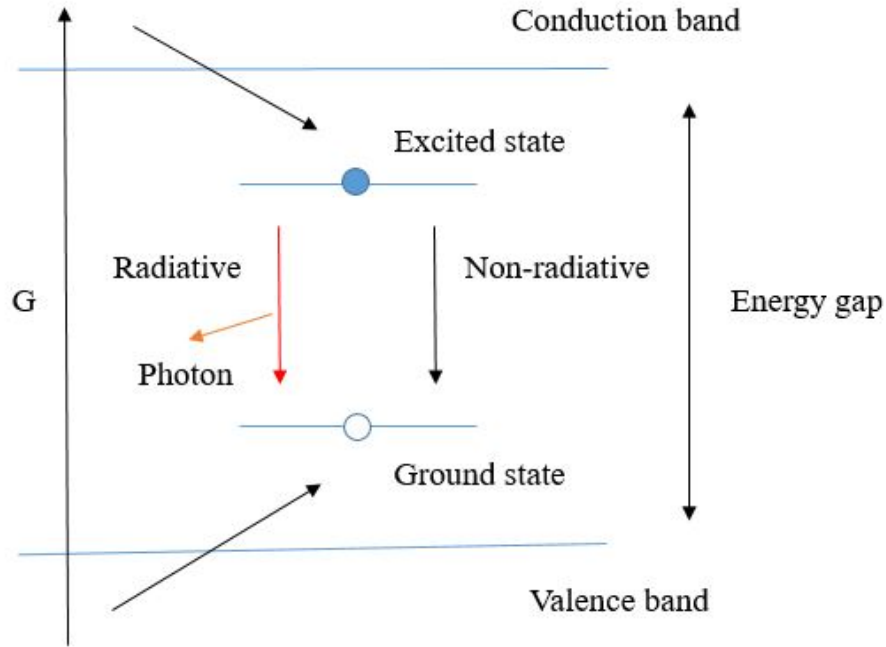


**Figure 1.3.** An illustration of a monomolecular recombination process.

$$\frac{dn}{dt} = G - \frac{n}{\tau} = G - \frac{n}{\tau_{nr}} - \frac{n}{\tau_r} \quad (1.4)$$

where  $n$  is the concentration of the excited electrons in the luminescence centers, and  $G$  denotes the concentration of absorbed photons per unit time.  $G$  is often called the generation term.

For SSPL, the term on the left hand side in Eqn. (1.4) is 0 in the steady state. Then we can rewrite the generation term  $G$  as

$$G = \frac{n(0)}{\tau} = \frac{n(0)}{\tau_{nr}} + i(0) \quad (1.5)$$

where  $n(0)$  is the concentration of the electrons in the steady state, and  $i(0)$  denotes the steady-state luminescence intensity. For the sake of simplicity, let us assume there is no reflection loss from the sample surface. The excitation radiation intensity  $I_{ex}$  is commonly defined as the surface density of incident photons per unit time. So if we consider an excited luminescence surface area  $\Delta S$ , we can derive the generation term  $G$  as

$$G = \frac{I_{ex}\Delta S}{\Delta S\alpha^{-1}} = \alpha I_{ex} \quad (1.6)$$

where  $\alpha$  is the absorption coefficient, and thus the inverse quantity,  $\alpha^{-1}$ , is the depth of the subsurface layer where absorption takes place. Then from Eqn. (1.6), we can obtain the expression for the stationary luminescence intensity

$$i(0) = G - \frac{n(0)}{\tau_{nr}} = \alpha I_{ex} - \frac{\tau_r}{\tau_{nr}} i(0) \quad (1.7)$$

Recalling Eqn. (1.2), we can rewrite  $i(0)$  as

$$i(0) = \eta \alpha I_{ex} \quad (1.8)$$

Therefore, the steady-state luminescence intensity is directly proportional to the excitation intensity for a monomolecular process. This relation provides a very important guideline to interpret experimental data. A linear increase in luminescence intensity when excitation intensity increases indicates that the examined luminescence has a microscopic origin related to a localized center. This can help exclude other types of recombination processes.

For TRPL, the excitation is switched off at  $t = 0$ , and then  $G = 0$ . So the solution of Eqn. (1.4) is

$$n(t) = n(0)e^{-\frac{t}{\tau}} \quad (1.9)$$

And the time dependence function of luminescence intensity is

$$i(t) = \frac{n(t)}{\tau_r} = i(0)e^{-\frac{t}{\tau}} \quad (1.10)$$

This shows that the decay curve of PL intensity in TRPL measurement is single-exponential for monomolecular process. The recombination lifetime can be obtained by fitting the curve. If there are more than one efficient recombination centers, the decay is multiple-exponential,  $i(t) = \sum i(0)_j e^{-\frac{t}{\tau_j}}$ .

### 1.1.2 Bimolecular process

Here we introduce a process where free electron-hole pairs are generated when the excitation energy is larger than the band gap. We need to consider the concentrations of both electrons and holes, and hence this process is usually called bimolecular recombination process. We do not consider any impurity atom or lattice defect around the position of the generated photocarriers. Therefore the electron-hole pairs diffuse along the edges of the conduction band and valence band and the recombination happens between the electrons and their nearest holes where there is a largest overlap of their wavefunctions. As in the case of the monomolecular process, both radiative and non-radiative recombination processes can occur in a bimolecular process (Figure 1.4). Similar with what we have for the monomolecular process, the bimolecular process can be described as

$$\frac{dn}{dt} = G - \beta np \quad (1.11)$$

where  $n$  and  $p$  are the concentrations of electrons and holes.  $G$  is still the generation term.  $\beta$  denotes the bimolecular recombination coefficient, which is a sum of bimolecular non-radiative ( $\beta_{nr}$ ) and bimolecular radiative ( $\beta_r$ ) recombination coefficients. Thus  $\beta_r np$  actually



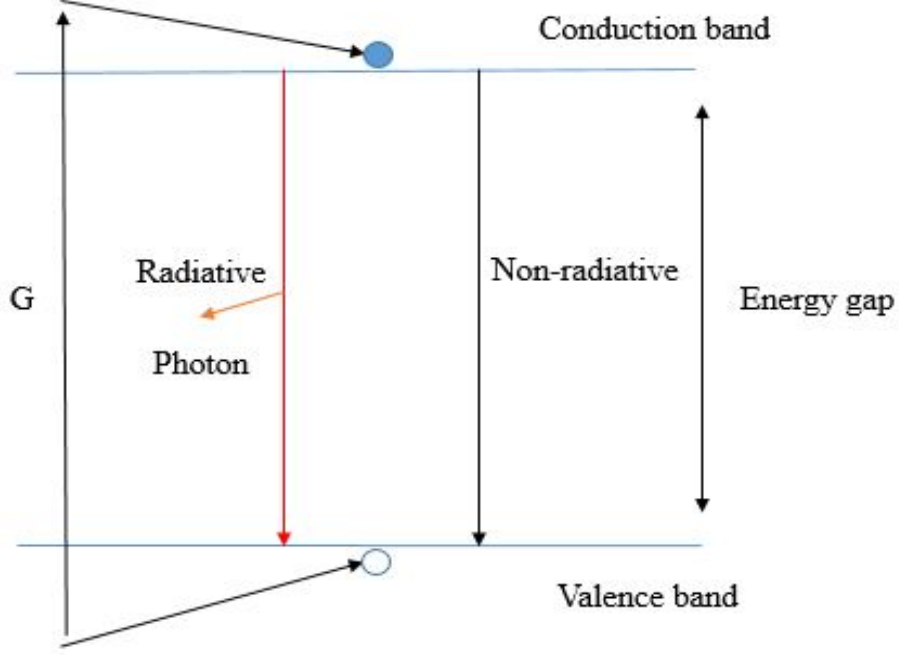


**Figure 1.4.** An illustration of a bimolecular recombination process.

represents the luminescence intensity of a bimolecular process. In order to simplify the following discussion, we consider an intrinsic semiconductor. Hence the concentration of electrons is approximately the same as that of holes. Then Eqn. (1.11) can be written as

$$\frac{dn}{dt} = G - \beta n^2 \quad (1.12)$$

For SSPL,  $\frac{dn}{dt}$  is 0 in Eqn. (1.12). Then we have

$$i(0) = \beta_r n^2(0) = G - \beta_{nr} n^2(0) = G - \frac{\beta_{nr}}{\beta_r} i(0) \quad (1.13)$$

where  $n(0)$  is the steady-state concentration of electrons and  $i(0)$  is the stationary luminescence intensity in the steady state. By introducing the excitation radiation intensity, similarly with the discussion for a monomolecular process, we get

$$i(0) = \frac{\beta_r}{\beta_{nr} + \beta_r} \alpha I_{ex} \quad (1.14)$$

Here we find that the steady-state luminescence intensity is still a linear function of the excitation intensity for a bimolecular process.

We have to keep in mind that so far we have only considered the steady state in our discussion. SSPL is generally achieved by the use of a continuous excitation radiation source, like a semiconductor laser, an incandescent lamp, etc. However, it may be preferable to use powerful laser pulses for examining a bimolecular process, because a bimolecular recombination process always requires a much higher density of electron-hole pairs. Thus, without the use of a continuous excitation source, the relation between the luminescence intensity and the excitation intensity will be different from Eqn. (1.14).

Based on Eqn, (1.12), we can solve the differential equation to get  $n(t)$  [2]

$$n(t) = \sqrt{\frac{G}{\beta}} \frac{1 - e^{-2t\sqrt{G\beta}}}{1 + e^{-2t\sqrt{G\beta}}} + \text{constant} \quad (1.15)$$

Suppose we have a rectangular pulse with a duration  $\tau_{pulse}$  and the initial condition is  $n(0) = 0$  at time  $t = 0$ . The pulse duration is sufficiently short, so  $2t\sqrt{G\beta}$  would be much smaller than 1. Then we can use the expansion  $e^{-x} \approx 1 - x$  to get

$$n(t) \approx \sqrt{\frac{G}{\beta}} \frac{t\sqrt{G\beta}}{1 - t\sqrt{G\beta}} \approx Gt \quad (1.16)$$

Thus the luminescence intensity can be written as

$$i(t) = \beta_r n^2(t) \approx \beta_r \alpha^2 t^2 I_{ex}^2 \quad (1.17)$$

Here, we find that the luminescence intensity is no longer proportional to the excitation intensity but the square of it. Normally an excitation with a duration of the order of nanoseconds or tens of picoseconds is short enough so that we can employ Eqn. (1.17) [2].

For TRPL,  $G = 0$  when the excitation is switched off at  $t = 0$ . So the solution of Eqn. (1.12) is

$$n(t) = \frac{n(0)}{\beta n(0)t + 1} \quad (1.18)$$

The time dependence function of PL intensity is

$$i(t) = \beta_r n^2(t) = \frac{i(0)}{(\beta t \sqrt{\frac{i(0)}{\beta_r}} + 1)^2} \quad (1.19)$$

Here the luminescence decay does not have an exponential function anymore, and the intensity is approximately proportional to  $\frac{1}{t^2}$ .

### 1.1.3 Multiple process

In real cases, both monomolecular and bimolecular recombination can happen at the same time (Figure 1.5). Thus, under an excitation of  $G = \alpha I_{ex}$ , the excited electrons can be

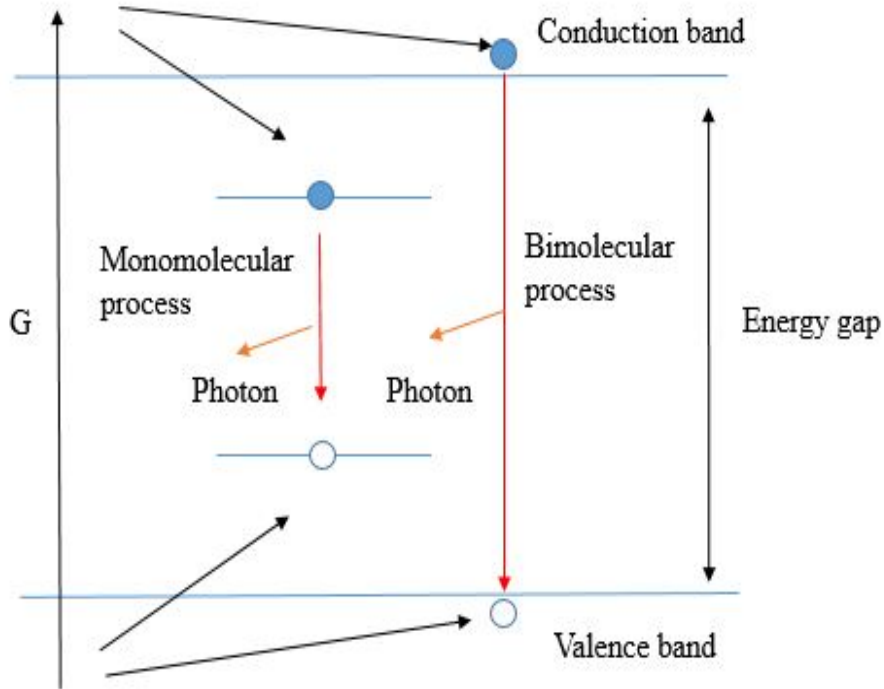


**Figure 1.5.** A monomolecular process and a bimolecular process present simultaneously.

divided into 2 groups. One group of electrons will experience a bimolecular recombination process with a coefficient  $\beta$ . The other group of electrons will reach the bottom of the conduction band, which is described by a rate  $k$ , and get captured by the impurity centers

with a rate  $a$ . In order to simplify the following discussion, we only consider an intrinsic semiconductor and ignore the non-radiative process. Then we can describe the processes by the equations as follows:

$$\frac{dn_0}{dt} = \alpha I_{ex} - \beta n_0^2 - k n_0 \quad (1.20)$$

$$\frac{dn_t}{dt} = k n_0 - a(N_0 - N)n_t \quad (1.21)$$

$$\frac{dN}{dt} = a(N_0 - N)n_t - \frac{N}{\tau} \quad (1.22)$$

where  $n_0$  denotes the density of generated electrons after excitation.  $n_t$  is the concentration of the electrons at the bottom of the conduction band to be captured by impurity centers.  $N$  is the concentration of excited centers.  $N_0$  is the total density of impurity atoms.  $\tau$  is the lifetime of the monomolecular recombination process.

For SSPL,  $\frac{dn_0}{dt}$ ,  $\frac{dn_t}{dt}$ , and  $\frac{dN}{dt}$  are all 0. Thus we can obtain

$$\frac{N}{\tau} = \frac{a n_t N_0}{1 + a n_t \tau} \quad (1.23)$$

$$n_0 = \frac{k}{2\beta} \left( \sqrt{1 + \frac{I_{ex}}{\frac{k^2}{4\alpha\beta}}} - 1 \right) \quad (1.24)$$

$$a n_t \tau = \frac{\frac{k^2}{2\beta} \left( \sqrt{1 + \frac{I_{ex}}{\frac{k^2}{4\alpha\beta}}} - 1 \right)}{\frac{N_0}{\tau} - \frac{k^2}{2\beta} \left( \sqrt{1 + \frac{I_{ex}}{\frac{k^2}{4\alpha\beta}}} - 1 \right)} \quad (1.25)$$

Here, the term  $\frac{k^2}{4\alpha\beta}$  has the same unit as the excitation  $I_{ex}$ . It is governed by the material properties. Therefore, we can use it to classify the excitation source into weak excitation and strong excitation.

If the excitation intensity is much smaller than  $\frac{k^2}{4\alpha\beta}$ , the excitation can be called "weak excitation". By the use of  $\sqrt{1+x} \approx 1 + \frac{x}{2}$  for  $x \ll 1$ , we have

$$n_0 \approx \frac{\alpha I_{ex}}{k} \quad (1.26)$$

$$I_b = \beta n_0^2 = \frac{\alpha^2 \beta}{k^2} I_{ex}^2 \quad (1.27)$$

$$an_t N_0 \approx \frac{N_0 \alpha I_{ex}}{N_0 - \alpha \tau I_{ex}} \quad (1.28)$$

$$an_t \tau \approx \frac{\tau \alpha I_{ex}}{N_0 - \alpha \tau I_{ex}} \quad (1.29)$$

$$I_m = \frac{N}{\tau} = \alpha I_{ex} \quad (1.30)$$

where  $I_b$  and  $I_m$  denote the luminescence intensity of the bimolecular process and monomolecular process, respectively. The result shows that the luminescence intensity from the monomolecular process is proportional to the excitation intensity, while the luminescence signal from the bimolecular process is not. All absorbed energy,  $\alpha I_{ex}$ , is basically converted to the monomolecular process luminescence. Hence, the bimolecular process luminescence is significantly weaker than the monomolecular process luminescence under a weak excitation, which also means not all impurity centers get excited. Then we can derive the following condition for the weak excitation case

$$an_t \tau << 1 \quad (1.31)$$

If the excitation intensity is much larger than  $\frac{k^2}{4\alpha\beta}$ , the excitation can be called "strong excitation". And based on the relation shown above, we also have

$$an_t \tau >> 1 \quad (1.32)$$

Then the luminescence intensity of the monomolecular process is

$$I_m = \frac{N}{\tau} = \frac{an_t N_0}{1 + an_t \tau} \approx \frac{an_t N_0}{an_t \tau} = \frac{N_0}{\tau} \quad (1.33)$$

Here we clearly see that the monomolecular luminescence intensity reaches a maximum, which means the monomolecular process becomes saturated. Furthermore, we can obtain

$$n_0 \approx \frac{k}{2\beta} \sqrt{\frac{I_{ex}}{\frac{k^2}{4\alpha\beta}}} \quad (1.34)$$

$$I_b = \beta n_0^2 \approx \alpha I_{ex} \quad (1.35)$$

Now the bimolecular process luminescence intensity is proportional to the excitation intensity, which means it is much larger than the luminescence intensity from the monomolecular process. In this case the bimolecular recombination process becomes dominant. However, we need to keep in mind that a very high excitation may introduce new luminescence channels and thus new kinetic equations need to be derived [3].

In this section, we introduced the theoretical analysis of kinetic equations for monomolecular and bimolecular processes. These 2 different types of process have different excitation dependence of PL intensity. When both processes exist, which process is dominant is dependent on the intensity of excitation. In this thesis, we take both steady state PL and time-resolved PL for our samples. Due to weak excitation applied in the measurements, monomolecular process is dominant for PL signal. Therefore, multiple-exponential is used to fit the decay curve to obtain time constants based on the PL decay spectra from TRPL measurements.

## 1.2 Typical channels of radiative recombination

We have briefly introduced radiative recombination processes in the previous sections. Now we will give more detail about some typical channels of radiative recombination in crystalline semiconductors.

When the excitation source is not a strong one, like an incandescent lamp, a gas-discharge tube, or a continuous-wave gas laser with the output power of the order of 0.01-10 W/cm<sup>2</sup>, the low-fluence or weak excitation leads to the following recombination processes [2]:

1. radiative recombination of free excitons (FE or X);
2. radiative recombination of free excitons with simultaneous emission of an LO phonon (FE-LO or X-LO);
3. radiative recombination of a bound exciton (BE);
4. radiative recombination of donor-acceptor pairs ( $D^0-A^0$ );
5. radiative recombination of a free hole with a neutral donor or a free electron with a neutral acceptor ( $h-D^0$  and  $e-A^0$ );
6. radiative recombination of free electron-hole pairs (e-h).

If the excitation source is strong enough, for example, a pulsed laser with an output power of the order of 1 kW-10 MW/cm<sup>2</sup>, there are additional recombination processes [2]:

1. radiative decay of an excitonic molecule (EM or XX);
2. luminescence from inelastic collisions of excitons (X-X collisions);
3. luminescence from electron-hole liquid (EHL);
4. luminescence from electron-hole plasma (EHP);
5. luminescence from Bose-Einstein condensation of excitons or excitonic molecules.

Here we will focus on some of the simplest channels.

### 1.2.1 Recombination of free electron-hole pairs (e-h)

This process is actually the bimolecular process introduced in previous sections. However, here we will discuss it in more detail.

#### Direct bandgap

Let us start with a discussion for a bulk direct bandgap semiconductor. As shown in Figure 1.6, an electron with energy  $E_2$  recombines with a hole with energy  $E_1$ . They need

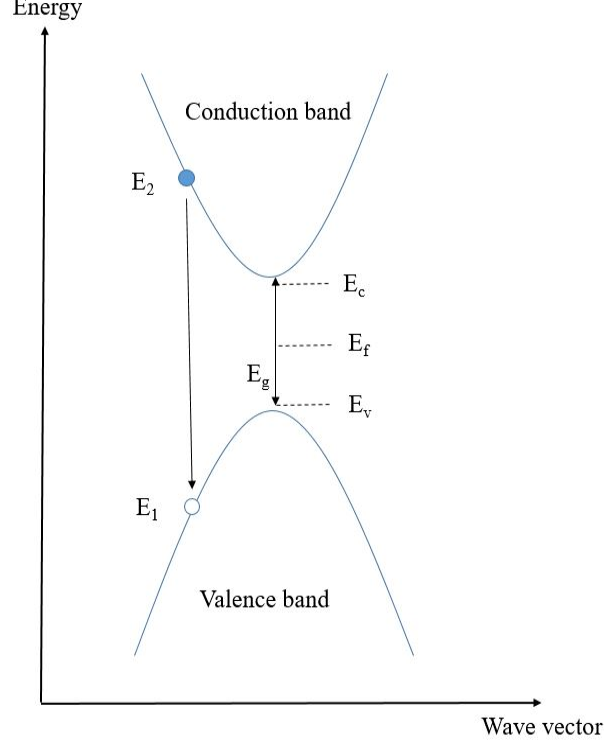


**Figure 1.6.** A recombination process of free electron-hole pairs in a bulk direct bandgap semiconductor

to have the same wavenumber so that the transition is vertical. The energy of the emitted photon is  $h\nu = E_2 - E_1$ . The luminescence intensity is given by the probability density  $I_p$  of the radiative emission, and  $I_p$  is influenced by the joint density of states  $\rho$  of electron and hole in the corresponding bands, the radiative lifetime  $\tau_r$  [4], and the probability of occupation of conduction and valence band states  $f_e$ . Thus, the probability density is derived as

$$I_p \approx \frac{f_e \rho}{\tau_r} \quad (1.36)$$

Furthermore, we can express  $f_e$  as the product of occupancy factors  $f_c$  and  $f_v$

$$f_e = f_c f_v = f(E_2)[1 - f(E_1)] \quad (1.37)$$

where  $f_c$  and  $f_v$  represent the occupation of electrons in the conduction band and occupation of holes in the valence band, respectively. For the sake of simplicity, we consider the process



taking place at low temperature and low fluence excitation. Hence, the semiconductor can be treated to be in thermal equilibrium, so that the Fermi level stays in the middle of the band gap. According to Fermi-Dirac distribution

$$f(E) = \frac{1}{e^{\frac{E-E_f}{k_B T}} + 1} \quad (1.38)$$

and considering a wide band gap and the low temperature,  $k_B T \ll \frac{E_g}{2} \approx E_2 - E_f \approx E_f - E_1$

$$1 - f(E_1) \approx e^{\frac{-(E_f - E_1)}{k_B T}} \quad (1.39)$$

$$f(E_2) \approx e^{\frac{-(E_2 - E_f)}{k_B T}} \quad (1.40)$$

Therefore, we obtain

$$f_e \approx e^{\frac{-h\nu}{k_B T}} \quad (1.41)$$

The densities of states in the conduction band  $\rho_c$  and the valence band  $\rho_v$  can be derived as [5]

$$\rho_v = \frac{(2m_h)^{\frac{3}{2}}}{2\pi^2 \hbar^3} (E_v - E)^{\frac{1}{2}}, E_v > E \quad (1.42)$$

$$\rho_c = \frac{(2m_e)^{\frac{3}{2}}}{2\pi^2 \hbar^3} (E - E_c)^{\frac{1}{2}}, E_c < E \quad (1.43)$$

where  $m_e$  and  $m_h$  denote the effective mass of an electron and a hole in the corresponding bands. Thus the joint density of states  $\rho$  can be described as

$$\rho = \frac{(2m_r)^{\frac{3}{2}}}{\pi \hbar^2} (h\nu - E_g)^{\frac{1}{2}}, h\nu > E_g \quad (1.44)$$

where  $m_r$  is the reduced mass of an electron-hole pair, given by

$$\frac{1}{m_r} = \frac{1}{m_e} + \frac{1}{m_h} \quad (1.45)$$

Now the formula for the probability density  $I_p$  of the radiative emission can be expressed as

$$I_p \approx \left[ \frac{(2m_r)^{\frac{3}{2}}}{\pi \hbar^2 \tau_r} e^{\frac{-E_g}{k_B T}} \right] (h\nu - E_g)^{\frac{1}{2}} e^{\frac{-(h\nu - E_g)}{k_B T}} \quad (1.46)$$

This formula gives us an idea of how the related emission spectrum looks like.  $(h\nu - E_g)^{\frac{1}{2}}$  characterizes the joint density of states, and  $e^{\frac{-(h\nu - E_g)}{k_B T}}$  describes the occupancy of those states. Given a plot of luminescence intensity vs  $h\nu - E_g$ , the curve is not symmetric, which stems from the kinetic energy of the e-h recombination and can be described by an exponential distribution function [2]. A good agreement between theoretical emission curve and experimental result has been found for InSb at low temperature [6]. The full width at half maximum (FWHM) can be derived as [2]

$$FWHM \approx 1.8k_B T \quad (1.47)$$

$FWHM \approx 1\text{-}20$  meV if the temperature is between 4 and 100 K. With the increase of the temperature, the electron-hole pairs can move to states which are further from the extremes of the corresponding bands. Thus photons with higher energy can be emitted, while the low-energy onset of the curve will stay almost the same due to the restriction of the band gap. This is why the curve becomes broader when the temperature increases.

## Indirect bandgap

Now let us move on to bulk indirect bandgap semiconductors (Figure 1.7). In this case we need to take into consideration the involvement of phonons. In order to simplify the discussion, we treat low temperature cases and assume that phonon dispersion relations are defined for any wavenumber so that an appropriate phonon can always be found to ensure the recombination takes place. Thus, we need to do an integral to get the probability density  $I_p^{in}$

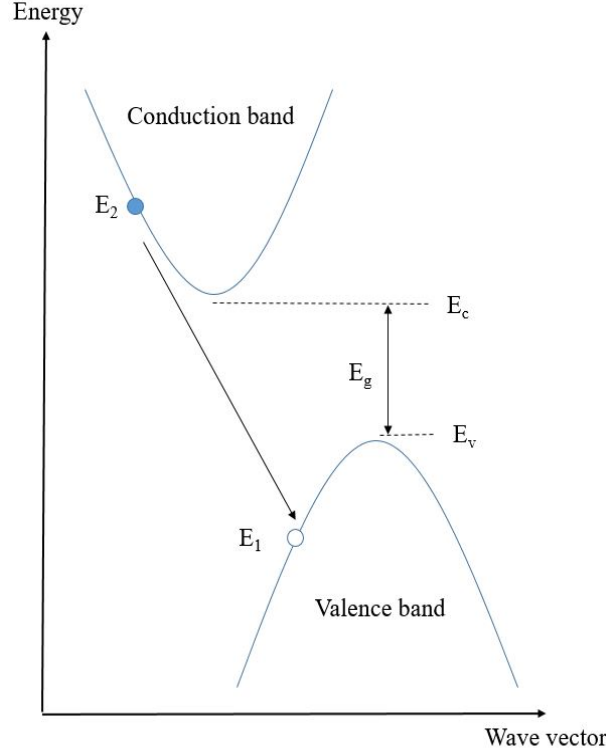


**Figure 1.7.** A recombination process of free electron-hole pairs in a bulk indirect bandgap semiconductor.

of the radiative emission. The integration is over all possible pairs of states in the conduction band and valence band.

$$\begin{aligned}
 I_p^{in} &= \frac{1}{\tau_r} \int_0^{\hbar\nu + \hbar\omega - E_g} \rho_c(E_e) f_c(E_e) \rho_v(E_h) f_v(E_h) dE_e \\
 &= \int_0^{\hbar\nu} \sqrt{(E_e)(\hbar\nu - E_e)} f_c(E_e) f_v(\hbar\nu - E_e) dE_e
 \end{aligned} \tag{1.48}$$

where the energy conservation is  $E_2 - E_1 = \hbar\nu + \hbar\omega$ ,  $E_e = E_2 - E_c$  for the electron,  $E_h = E_v - E_1$  for the hole, and  $\hbar\nu = \hbar\nu + \hbar\omega - E_g$ .  $\hbar\omega$  is the energy of a phonon, which is involved to ensure the conservation of momentum. Recalling the analysis done for the direct bandgap case and making use of  $\int_0^a \sqrt{x(a-x)} dx \approx a$  [2], we have

$$I_p^{in} \approx [\hbar\nu - (E_g - \hbar\omega)]^2 e^{\frac{-(\hbar\nu - (E_g - \hbar\omega))}{k_B T}} \tag{1.49}$$

Here we see the energy of the phonon has been involved. The lineshape is still most influenced by the exponential factor.

In general, the e-h recombination is hard to observe in practice. A very narrow bandgap and low exciton binding energy are needed. The crystal needs to be pure and the measurement is usually taken at slightly elevated temperatures [2], when some excitons are excited and thermal luminescence quenching is not yet efficient. Thus, for most semiconductors, other recombination channels such as exciton recombination are more likely to happen and then the luminescence spectrum is always not from e-h recombination. InSb is just one of the rare exceptions whose e-h recombination can be triggered to generate the related PL spectrum. [2]

### 1.2.2 Recombination of a free electron (hole) with a neutral acceptor (donor)(e-A<sup>0</sup> and h-D<sup>0</sup>)

When a semiconductor is doped with some material, impurity atoms are introduced in it. These impurity atoms form acceptors or donors. The donor or acceptor levels usually exist inside the band gap. When an electron (or a hole) diffuses in the conduction band (or valence band), it can also interact with an acceptor (or a donor), besides the recombination with a hole (or an electron). Thus, some specific luminescence is emitted. We have to state that only if free electron-hole pairs are generated by the excitation, can e-A<sup>0</sup> or h-D<sup>0</sup> transitions happen. For the sake of simplicity, we talk about shallow neutral donors and acceptors in an intrinsic semiconductor (Figure 1.8).

We first focus on the recombination of a free electron with a neutral acceptor. Usually the hole at the acceptor level can be regarded as an immobile quasi-particle with an infinite effective mass.[2] If we compare Figure 1.6 and Figure 1.8, it is obvious that e-h transition and e-A<sup>0</sup> have some similarity. Thus we should have a similar formula for the probability density  $I_p^{e-A^0}$  of the radiative emission

$$I_p^{e-A^0} \approx [h\nu - (E_g - E_A)]^{\frac{1}{2}} e^{\frac{-[h\nu - (E_g - E_A)]}{k_B T}} \quad (1.50)$$

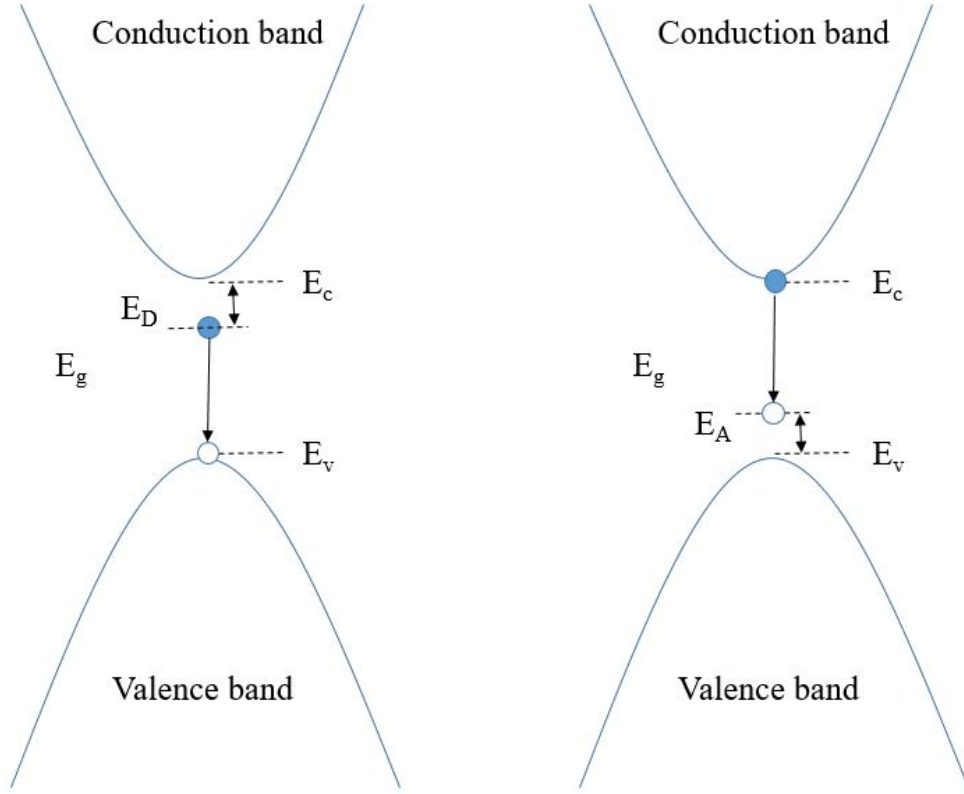


**Figure 1.8.** Recombination of a free hole with a neutral donor (left) and of a free electron with a neutral acceptor (right).

The electrons trapped at the acceptor level after recombination will continue to recombine with holes in the valence band, but this transition is always non-radiative. Then the acceptor state becomes available again and the luminescence process can happen again under optical excitation.

We can also obtain a similar formula for the probability density  $I_p^{h-D^0}$  of the radiative emission for a  $h-D^0$  transition

$$I_p^{h-D^0} \approx [h\nu - (E_g - E_D)]^{\frac{1}{2}} e^{\frac{-[h\nu - (E_g - E_D)]}{k_B T}} \quad (1.51)$$

Therefore, the lineshape of an  $e-A^0$  or  $h-D^0$  emission spectrum is very similar to that of an  $e-h$  transition, except the low-energy onset. This kind of lineshape is referred to as Maxwell-Boltzmann lineshape [2]. As long as at least one of the recombination particles is

free, the luminescence spectral line has a Maxwell-Boltzmann shape, which is asymmetric and has a high-energy tail that becomes broader with the increase of temperature. Hence, this kind of lineshape reflects the kinetics of the free quasi-particle.

Finally we need to emphasize that the low temperature and high purity are the key conditions to obtain such a lineshape. If the material is not pure enough, there are slightly varying donor and acceptor levels, which leads to more broadened lines. The low temperature avoids the ionization of donors. In indirect semiconductors, there are very few free electrons and holes compared with excitons, thus both  $e-A^0$  and  $h-D^0$  radiative recombination processes are always difficult to observe.

### 1.2.3 Recombination of donor-acceptor pairs ( $D^0-A^0$ )

In some semiconductors, there are both neutral donors and acceptors. Therefore, a radiative recombination process of donor-acceptor pairs is possible. By the approximation of effective mass, we are able to consider a neutral acceptor as a nucleus with an "extra" hole orbiting it [2]. Similarly, the neutral donor can be considered in the same way as a nucleus with an electron orbiting it (Figure 1.9). Light will be emitted when the electron recombines with the hole (Figure 1.10). The donor and acceptor will be ionized immediately after the recombination process. Then free electron-hole pairs produced by the excitation will neutralize them very quickly. Hence we need to consider the Coulomb interaction between these ionized acceptors and donors. If the ionized donors and acceptors are considered as point charges, the energy of the photon  $h\nu$  emitted in the recombination can be written as

$$h\nu = E_g - E_A - E_D + \frac{e^2}{4\pi\epsilon_r\epsilon_0 R}(-J(R)) \quad (1.52)$$

where  $E_A$  represents the energy difference between the acceptor level and the top of valence band.  $E_D$  represents the energy difference between the donor level and the bottom of conduction band.  $J(R)$  is a correction term for the overlap of the wavefunctions when the distance  $R$  between the donor and acceptor is too small. This term will disappear if  $R$  is large enough, which usually means it is much larger than the lattice constant. Different

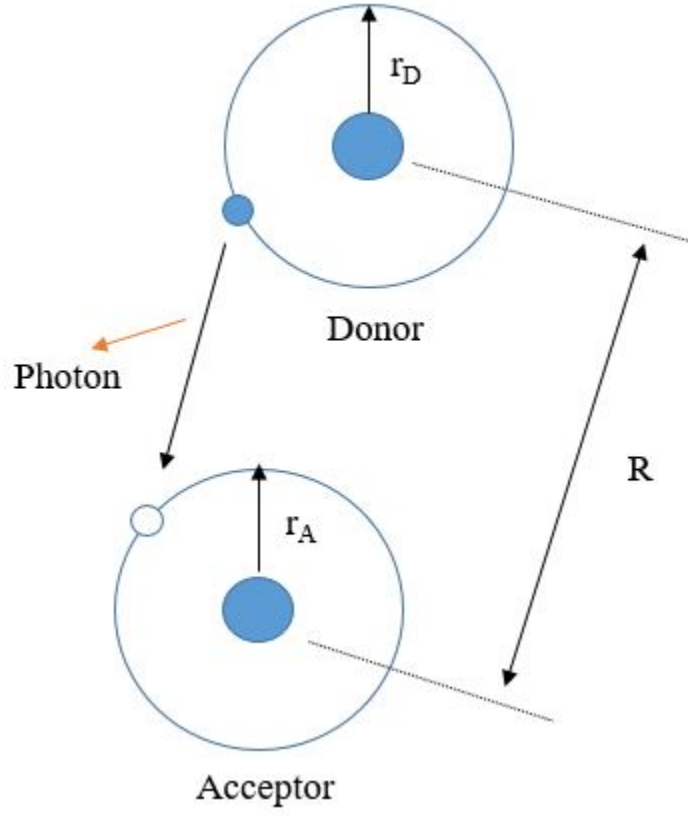


**Figure 1.9.** A diagram of a donor-acceptor pair.

distances between the donor and acceptor then result in sparse lines on the high energy end in the PL spectrum due to  $D^0-A^0$  transitions [7].

In general, when the semiconductor material has weak electron-phonon coupling, it is hard to obtain a PL spectrum showing resolved lines of  $D^0-A^0$  transitions even if key experimental conditions, such as narrow slits and low temperatures, are applied. Concentration of dopants is another important factor. If it is too low, the neutral donor and acceptor are likely to be too far from each other, which makes it difficult to create recombination. If the donor and acceptor concentrations are too high, the interaction between the donor and acceptor may not be regarded as simple Coulomb interaction anymore, and a so-called "concentration quenching" is likely to happen [2]. Hence, a moderate doping level is needed. This doping level depends on the choice of semiconductor materials. Sometimes, the excitation needs to

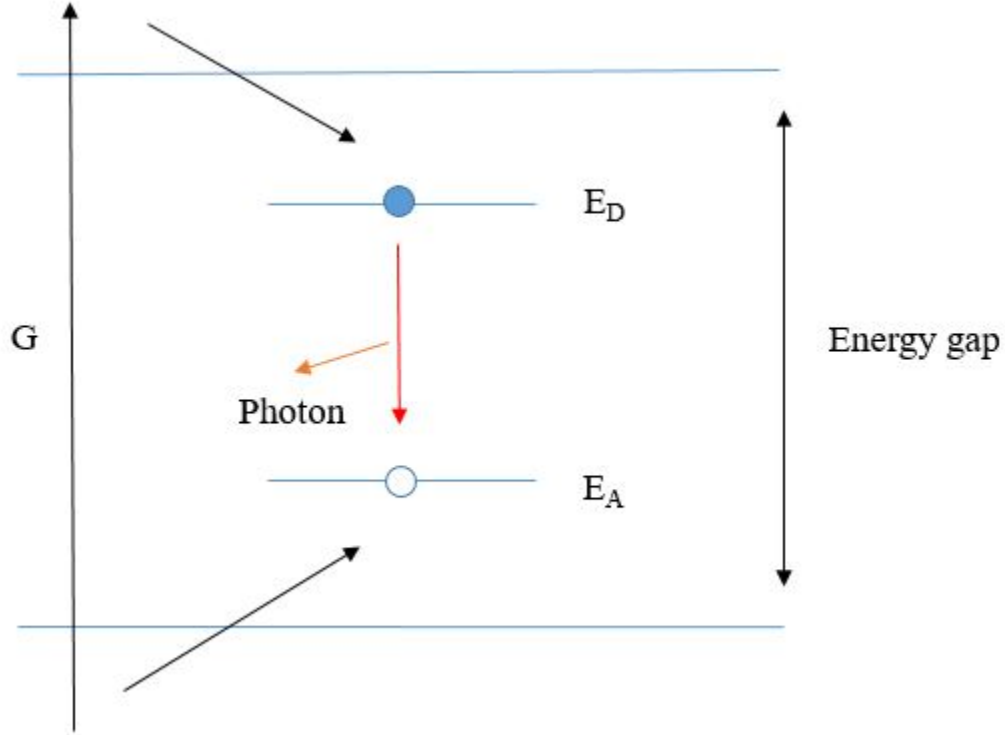


**Figure 1.10.** Recombination of a donor-acceptor pair.

be elevated a little to obtain a better spectrum. Therefore, such a PL spectrum has not been observed so far for all semiconductor materials [2].

#### 1.2.4 Recombination of free excitons (FE or X)

In this subsection, we will give a basic introduction to the radiative recombination of free excitons (FE or X). The most common recombination channel in an ideal pure semiconductor material is exciton recombination. If we consider the electron-hole pair as a bound "particle", where an electron and its hole are attracted to each other by Coulomb interaction, we only need to consider one quasi-particle instead of two, and this new "particle" is called an exciton. The internal energy is thus lower than the band gap and represents the lowest excitation energy needed to create excitons.

There are 3 major kinds of excitons: Frenkel exciton, charge transfer exciton, and Wannier exciton.



A Frenkel exciton is an exciton localized in a specific atom or molecule. It is always created by an excitation whose spatial extension is restricted only in a single unit cell. Therefore, the Frenkel exciton is also called a small-radius exciton. It always exists in molecular crystals.

A charge transfer exciton always exists in ionic crystals. When an excitation is applied, the electrons are transferred from a lattice anion to a nearest cation, then a maximum of the electron charge density is generated. This kind of exciton generally has a larger radius than a Frenkel exciton.

A Wannier exciton is an electron-hole pair whose radius can be larger than multiples of the lattice constant. Thus, it is also called a large-radius exciton. The wavefunction of a Wannier exciton is usually not localized, and the exciton can thereby move freely in the crystal. Therefore, a Wannier exciton is also called a free exciton. Wannier excitons are always generated in semiconductors. Hence, we will mainly focus on Wannier excitons.

Since the hole is usually heavier than the electron, the common way to discuss a Wannier exciton is to consider an electron rotating around a hole (Figure 1.11). The Coulomb potential is given by

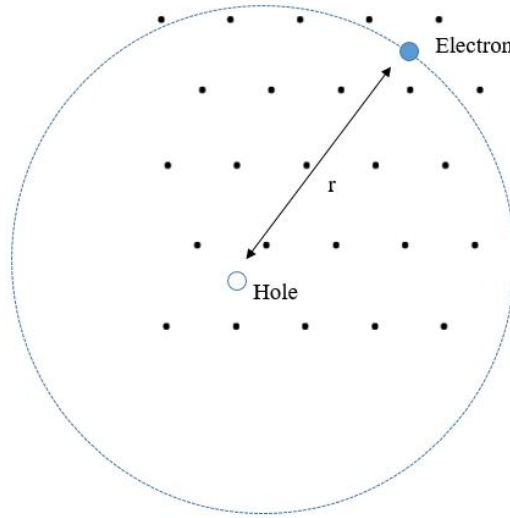


**Figure 1.11.** A diagram of a Wannier exciton in a 2D crystal.

$$U(r) = -\frac{e^2}{4\pi\epsilon_0\epsilon r} \quad (1.53)$$

where  $r$  is the distance between the electron and hole in an exciton, and  $\epsilon$  represents the dielectric constant of the semiconductor material. This configuration resembles the hydrogen atom. By the use of effective mass approximation, where the hole and electron are regarded as point charges with corresponding charges and effective masses, we can treat a Wannier exciton using a modified Bohr model.

First, let us deduce the Bohr radius of a Wannier exciton. It results from a rescaling of the Bohr radius of a hydrogen atom. Unlike the huge difference between the electron and the hydrogen nucleus masses, the electron and hole in a Wannier exciton have comparable masses. Thus the stability of a Wannier exciton is not as strong as that of a hydrogen atom, which results in a larger radius of the electron orbit. Then the Bohr radius of a Wannier exciton  $a_B^W$  can be written as

$$a_B^W = \frac{m_0}{m_r} \epsilon a_B \quad (1.54)$$

where  $m_0$  is the free electron mass and  $m_r$  is the reduced mass ( $\frac{m_e m_h}{m_e + m_h}$ ) of the effective masses of electron ( $m_e$ ) and hole ( $m_h$ ) in the exciton.  $a_B$  denotes the Bohr radius of a hydrogen atom, approximately 0.05 nm. Then the radius of the  $n^{th}$  orbit in the exciton is given by

$$r_n = n^2 \frac{m_0}{m_r} \epsilon a_B \quad (1.55)$$

Here we have to state that the semiconductor material may have different dielectric constant  $\epsilon$  under different conditions. Whether the static value or high-frequency value of the dielectric constant is applied depends on whether the volume of the exciton is large enough that the dielectric constant is homogeneous. Actually this issue has not been clarified yet up to now [2]. In order to get an idea of the order of magnitude of the exciton ground state radius, we can use 10 as the typical value of the dielectric constant, and usually the ratio of the free electron mass to the reduced mass is about 0.1. Then the ground state radius is about 5 nm.

Second, let us discuss the ionization energy of a Wannier exciton. The ionization energy of a free exciton  $E_X$  is given by

$$E_{Xn} = \frac{1}{n^2} \frac{m_r}{m_0} \frac{Ry(H)}{\epsilon^2} \quad (1.56)$$

where  $Ry(H)$  denotes the ground state energy of one hydrogen atom, which is about 13.6 eV. By the use of the typical values for  $\epsilon$  and  $\frac{m_r}{m_0}$  mentioned above, the typical value of the ground state energy of a Wannier exciton is about 13 meV. Therefore, its order of magnitude is tens of meV.

A Wannier exciton can move freely inside a crystal. Thus it is likely to collide with phonons. Only if the Coulomb potential is strong enough can the exciton be stable and not break up under the collision with phonons. In general, the ionization energy of the ground state should be larger than  $k_B T$ . Thus, in semiconductors, excitons typically exist only at low temperatures. For example,  $k_B T = 10$  meV, temperature is about 110 K.

The exciton wavefunction has the same translational symmetry as the crystal lattice, and its spatial localization extent is given by the envelope wavefunction. The total energy of a free exciton involves its kinetic energy, and is described by

$$E_n(\mathbf{K}) = E_g - E_{Xn} + E_k = E_g - \frac{1}{n^2} \frac{m_r}{m_0} \frac{Ry(H)}{\epsilon^2} + \frac{\hbar^2 K^2}{2(m_e + m_h)} \quad (1.57)$$

where  $K$  is the wavenumber of the free exciton. This dispersion relation shows that some discrete exciton levels are introduced within the band gap. At  $\mathbf{K} = \mathbf{0}$ , the energy of exciton is no longer the same as the top of the valence band.

It is easy to realize that the crystal has to be pure enough to allow the existence of free excitons. Otherwise impurities will trap excitons when they move inside the crystal. Therefore, both purity of the crystal and low temperature are 2 key factors to observe luminescence from free exciton recombination.

The form of the energy of a free exciton gives us an idea of how the emission spectrum may look like. Nevertheless, the solid state is different from a gas of non-interacting hydrogen atoms. Since the excitons can interact with the emitted photons, the luminescence of free excitons is much more complicated. Our focus is on nitrides, which are direct semiconductors with wide band gap, here we mainly introduce a kind of luminescence which is common in III-V type semiconductors: resonant luminescence.

The energy of the emitted photon can be described by

$$E(K) = h\nu = \frac{\hbar c K}{\sqrt{\epsilon_\infty}} \quad (1.58)$$

In direct semiconductors, the energy of the emitted photons can be equal to that of the free excitons at some specific wavenumber. Thus, the emitted photons can be resonantly reabsorbed when they travel inside the crystal. Actually, the absorption coefficient of this process is usually larger than  $10^4 \text{ cm}^{-1}$  [8]. So we can imagine a simple situation that the emitted photon is reabsorbed and transferred back to an exciton, and then another recombination takes place. The emitted photon is re-absorbed again and so on. Maybe this description is oversimplified, but at least it gives us an idea that it may be better to treat the exciton and emitted photon together as they form a new quasi-particle named as an exciton-polariton.

Since the energy of the emitted photon and the energy of the exciton can be equal to each other, we have to consider possible interactions between them. Hence, their dispersion curves will split in the vicinity of the point where interaction happens, as shown in Figure 1.12. Around the interaction point, there is a mixed exciton-photon state, and far from the

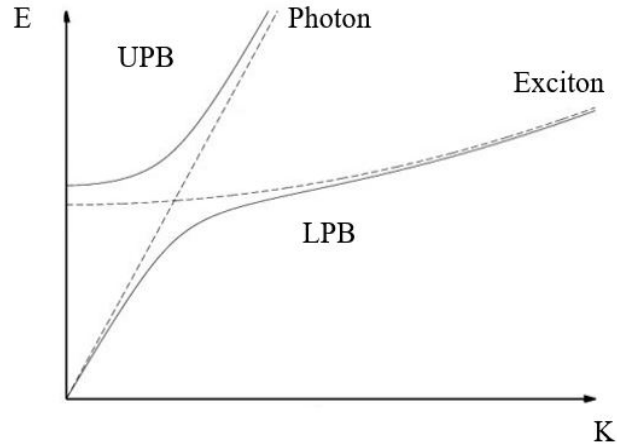


**Figure 1.12.** A schematic of the dispersion curves of an exciton-polariton.

interaction point, the curves behave very similar to a bare photon or exciton. The 2 branches are thereby called the upper polariton branch (UPB) and lower polariton branch (LPB).

For the sake of simplicity, we can consider a common situation where the polaritons are created via absorbing photons with higher energy. For LPB, the process starts from a high energy state which is far from the interaction point. Then by the emission of phonons, the energy of the exciton goes down to the interaction point. According to the dispersion curve shown in Figure 1.12, the process will slow down when the energy is close to the interaction point. There will be a similar process in the UPB. Therefore, an accumulation happens at the interaction point in both UPB and LPB. The lifetime has an order of  $10^{-9}$  s [2]. Then the recombination of the polaritons will happen after the lapse of the lifetime. The emitted photon will have energy very close to  $E_g - E_X$ . In general, there will be 2 peaks due to LPB and UPB respectively in the PL spectrum, and the LPB peak is more intense than the UPB peak, which is very common in many materials. This phenomenon is explained by Koteles *et al.* [9], who assumes that all excitons will accumulate mainly on the LPB branch after being thermalized. Thus, there will be only one peak in the PL spectrum if excitons just accumulate on the LPB branch. However, the material is always not pure enough. Acceptors and donors always exist in the material. The effective scattering cross-section of acceptors is always small due to its Bohr radius [2], so acceptors are not likely to collide with exciton-polaritons while donors are. When there are donors with a concentration higher than  $10^{15}$   $\text{cm}^{-3}$  [2], the scattering of exciton-polaritons by donors can not be ignored. Then some excitons will accumulate on the UPB branch and the related peak will show up in the PL spectrum. Since the LPB-related luminescence is still more or less dominant, the LPB peak intensity is generally higher than the UPB peak.

When the material is pure enough, LPB peak and UPB peak will not split. Koteles *et al.* has observed the splitting process of these 2 peaks in nominally undoped GaAs epilayers as the material purity was decreased [9]. So this provides an efficient method to assess the semiconductor purity. Nowadays this PL impurity analysis is an irreplaceable method in the microelectronics industry.

### 1.2.5 Recombination of bound excitons

In this subsection we will elaborate on bound excitons. Impurities are always likely to exist in materials regardless of growth technique. Then free excitons may be trapped by those impurities to form bound excitons (BE). The recombination related to bound excitons is extrinsic luminescence. Once bound excitons are generated, the recombination of bound excitons will dominate over the recombination of free excitons. A main factor for this phenomenon is that free excitons are more likely to be trapped by impurities than to directly have a recombination. We have calculated in previous sections that a typical value of a Wannier exciton Bohr radius  $a_X$  is about 5 nm. Thus the capture cross-section is

$$\sigma_X \approx \pi a_X^2 \approx 10^{-12} \text{ cm}^2 \quad (1.59)$$

Then the lifetime  $\tau_{trap}$  for a free exciton being trapped is described as

$$\tau_{trap} \approx \frac{1}{Nv\sigma_X} \quad (1.60)$$

where  $N$  is the impurity concentration and  $v$  is the speed of free exciton. This expression makes sense since higher impurity concentration, larger capture cross-section and higher moving speed make free excitons easier to get trapped. Let us take some typical values:  $N=10^{11} \text{ cm}^{-3}$ ,  $v=10^6 \text{ cm/s}$  (at around 2 K). Then the lifetime is around 1 ns.

This is comparable to the lifetime of FE recombination in direct semiconductors and much smaller than that in indirect semiconductors. Therefore, the recombination of bound excitons is much more likely to happen. In some low temperature measurements, the recombination of free excitons is completely suppressed.

Another factor which enhances the recombination of bound excitons is the so-called "giant oscillator strength". This is described by Rashba and Gurgenshili [10]. This term shows how the unit cells within a volume of about  $a_X^3$  around the impurity contributes to the recombination of excitons. The "giant" means those unit cells act like "antenna" to help the excitation energy transfer and the trapping of free excitons.

Because of the 2 effects described above, the PL of bound excitons is a very sensitive probe for the study of impurities in semiconductors.

Next I will introduce 2 common specific recombination channels of bound excitons: recombination of excitons bounded to ionized donors(acceptors) and neutral donors (acceptors). Since shallow donors or acceptors are common in our study for nitrides, here we mainly focus on the recombination of excitons bounded to shallow donors or acceptors.

### **Recombination of excitons bounded to ionized donors or acceptors ( $D^+-X$ or $A^--X$ )**

This recombination happens when free excitons get trapped by ionized donors or acceptors. A dissociation energy  $D_1$  will be released in this process. Then the energy of the emitted photon is

$$h\nu_{BE} = E_g - E_X - D_1 \quad (1.61)$$

Thus we know that in a PL spectrum, the separation between the low-energy threshold of FE line and the maximum of BE line provides information about the dissociation energy. If we consider the bounded exciton and the impurity as a whole complex, the dissociation energy acts like the binding energy we discussed previously for a free exciton. Thus, this energy is similarly related to the ratio  $\sigma$  of the effective mass of the electron  $m_e$  and hole  $m_h$ . Obviously, the exciton bounded to a hole or an acceptor can only be stable at some specific values or the complex will be easily destroyed. For example, for an exciton bounded to a donor, the hole needs to be heavy enough, or the kinetic energy of the hole will easily break the complex. By the use of an analogy with a  $H_2^+$ , a critical ratio  $\sigma_c$  for  $D^+-X$  is obtained around 0.43 while it is about 2.33 for  $A^- - X$ [2].

Therefore, we are able to conclude that  $A^- - X$  and  $D^+ - X$  can not exist at the same time in a given material. Since the hole is usually heavier than the electron,  $A^- - X$  is less likely to happen. Also, if the ratio  $\sigma$  is between 0.43 and 2.33, there is likely no  $A^- - X$  or  $D^+ - X$ .

## Recombination of excitons bounded to neutral donors or acceptors ( $D^0$ -X or $A^0$ -X)

Similar with what we have discussed in the previous subsection, the energy of the recombination of excitons bounded to neutral donors or acceptors is now given by

$$h\nu_{BE} = E_g - E_X - D_2 \quad (1.62)$$

$$h\nu_{BE} = E_g - E_X - h\omega - D_2 \quad (1.63)$$

where Eqn. (1.62) is for direct semiconductors while Eqn. (1.63) is for indirect semiconductors.  $D_2$  denotes the dissociation energy emitted in the trapping process. In analogy with a hydrogen molecule  $H_2$ , when the ratio  $\sigma$  goes to infinity, the dissociation energy is  $0.33E_D$  for a heavy hole and  $0.055E_D$  for a light hole [2]. In a PL spectrum,  $D_2$  for  $D^0$ -X ( $A^0$ -X) are provided by the separation between the X line and  $D^0$ -X ( $A^0$ -X) line. A major difference between the recombination of excitons bounded to neutral and ionized donors or acceptors is that there is an important law for  $D^0$ -X and  $A^0$ -X recombination. This law is called Haynes' rule. It claims that the dissociation energy is also influenced by the identity of the impurity atoms.

Based on the discussion of different recombination channels in this section, exciton recombination is the most commonly and easily observed process in crystalline semiconductors. According to our experimental conditions, we believe that the PL spectra discussed in this thesis come from the exciton recombination.

### 1.3 Experimental Setup

Photoluminescence spectroscopy is the experimental technique to detect and record the spectrum of luminescence radiation. A monochromator can be used to select a suitable excitation wavelength. The spectral content of the radiative emission is analyzed with a grating spectrometer. A typical setup for photoluminescence measurement is composed of a laser as an excitation source, a sample holder, a grating monochromator as a dispersive



element, a photo multiplier tube as a detector, an optical cryostat, filters, and collecting lenses.

### 1.3.1 Sample Placement

In the typical PL setup, a reflection geometry is used for sample illumination and light collection. The PL is collected by a condenser lens that must have a large numerical aperture to collect the emission light from a wide solid angle, because luminescence is a weak secondary radiative process [2]. The larger the portion of the emitted power we are able to collect, the better spectral analysis we can obtain. In order to avoid the possible reflection of the excitation source into the detector, the sample is always rotated to move the reflection light out of the detection cone. Therefore the most challenging part of the reflection geometry is the alignment to achieve both optimum excitation power density on the sample and maximum signal collection. If the sample is a very thin layer which has high quality surface, the sample can be even rotated to collect the emission through the edge. In this case, the sample itself can act like a waveguide to cause a coupled luminescence and the luminescence can be concentrated at the edge for output. This kind of geometry can avoid coupling the reflected light into the detection system as well. However, one problem of it is the possible stimulated emission due to the unintentional achievement of population inversion. This may distort the emission spectrum [11]. One possible way to avoid or reduce this effect is to limit the area of the excited region, but sometimes this is still not effective enough. However, this geometry is great if the stimulated emission and the optical gain need to be investigated. Another geometry for PL measurements is a transmission geometry, which means the sample is excited on one side and the signal is collected on the other side. Nevertheless, the emission spectrum will be likely distorted, because of the significant reduction by light scattering and re-absorption in the sample. Therefore the transmission geometry is rarely used.

### 1.3.2 Detector System

The most commonly used photodetector for PL spectroscopy is a photomultiplier tube (PMT). Today, a charge-coupled device (CCD) or an avalanche photodiode is sometimes used to replace a PMT. Here we give a brief introduction of these three types of detectors.

#### Photomultiplier Tube

A photomultiplier tube is a glass tube which is evacuated. It contains an array of dynodes, an anode and a photocathode. It works on the external photoelectric effect and secondary emission of electrons. A photon ejects an electron from the photocathode, and the photoelectrons are accelerated and focused onto the first dynode.  $n$  secondary electrons will be released by each of the primary electrons during this process from the dynodes. The secondary electrons will act as primary electrons for the next dynode, so the process will be repeated. If we have  $k$  dynodes, the number of the output electrons will be  $n^k$ , which is called the current amplification or photomultiplier gain. The typical value of this parameter is  $10^5$ - $10^7$ . Then these electrons will hit the anode and the resulting current is recorded.

Besides the possible high gain mentioned above, a photomultiplier can also have a large spectral range of sensitivity, typically between 150 nm and 1100 nm. For some specific PMT, it can even go up to 1400 nm [2].

#### Avalanche Photodiode

An avalanche photodiode makes use of the internal photoelectric effect. Typically it is composed of p, i, and n semiconductors with same material in series under high reverse bias. If a photon whose energy is larger than the band gap is absorbed, a pair of electron and hole is generated. This pair will be dissociated in the intrinsic layer by the strong electric field. The electron and hole will then be accelerated in different directions. Once the carriers reach higher energy than the band gap due to acceleration, more electron-hole pairs will be created and the same process will happen again. The number of carriers then increases in an avalanche.

Compared with the PMT, the avalanche photodiode has smaller size and better robustness. It also has a much wider spectral range than the PMT. The long wavelength cut-off is determined by the band gap of the photosensitive semiconductor material used in the photodiode. The drawback of an avalanche photodiode is the gain, which is only in the range of 10-500. This is because the working process is sometimes not stable enough to avoid avalanche breakdown and damage to the diode. In addition, it is possible to have a higher noise level due to the possible random process of symmetrical amplification in opposite directions.

## **Multichannel Detectors**

A multichannel detector contains a linear or 2-dimensional array of detectors. This is different from the PMT and avalanche photodiodes. The PMT and avalanche photodiodes are both single channel detector, which means the photon flux is only detected at a given time and a single area. The multichannel detectors are able to detect the photon flux at many areas at the same time, which can significantly increase the signal to noise ratio. For example, if we have a multichannel detector containing  $n$  elements in a linear array and the sensitivity of each element is the same as that of a single detector, then the required recording time will be just one  $n^{th}$  of that by a single detector. If we integrate the spectrum by the same time as we do with a single detector, the signal to noise ratio will be increased. This increase is beneficial for recording of the spectra when the signal flux is extremely low.

Two of the most common types of multichannel detectors are photodiode arrays and charge-coupled device (CCD) cameras.

### **1.3.3 Signal Detection Methods**

There are 2 general detection methods: phase-synchronous detection and photon counting. Since these methods are most used for single channel detectors, they are explained in the following in the case of single channel detectors.

## Phase-Synchronous Detection

This method is aimed to extract weak signals buried in various types of noise. It operates on the same principle as a lock-in amplifier. It uses 2 main components: a mixer and an integrator. The mixer adds a reference signal to the input signal to obtain a product signal of these 2 signals. Generally, the reference signal has an amplitude of unity. If the reference signal has the same frequency with the input signal and the phase shift is 0 or any integer multiple of  $2\pi$ , the product signal will be a positive only pulse. This is why this method is called synchronous detection. Then the product signal passes through the integrator, and a DC output voltage is obtained. The amplitude of this DC voltage is proportional to that of the input signal. If the input signal has a different frequency from the reference signal, the product signal will have both positive and negative components, and after a long enough time, the DC output voltage will be averaged 0. Therefore, we can select the signal component that we want.

In reality, sometimes, if the frequency of the input is an odd multiple of that of the reference signal, a DC voltage will be also included in the output of the mixer [2]. The general solution is to extend the time constant of the integrator. However, once the time constant becomes too large, the detector will take much more time to finish the measurement. An optimum time constant needs to be obtained by the experimenter's experience.

As mentioned earlier, this detection method is also sensitive to the phase shift. Nowadays, most detectors can tune the phase automatically to obtain a maximum output signal.

## Photon Counting

If the incoming light flux is too low, the phase-synchronous detection method usually does not work well any more. The reason is the generated signal on the detector is discrete now and has no continuous components. Then most detectors will just regard the signal as noise and ignore it. Hence, we need to introduce another detection method: photon counting.

Photoelectrons are generated when photons hit the detector. The number of the discrete pulses per unit time is proportional to the number of incident photons. First, an amplifier is used to multiply the input signal about 1000 times and low frequency components are filtered

out. Second, the components which are below a certain adjustable discrimination level are eliminated by a discriminator. In general, the thermionic emission signal will be filtered out in this process. Third, the number of pulses of the output signal from the discriminator is counted by a counter and then the digital information is sent to a digital to analogue converter. Finally, an analogue signal is obtained and recorded.

The photon counting method usually has many requirements for the apparatus. In general, a high quantum efficiency, an appropriate distribution of pulses, and an appropriate choice of the discrimination level are required. Also, this method has an excessive sensitivity to environmental noise, like noise from other labs, high-frequency perturbations from other equipment in the lab, etc. So shielding should be made as good as possible. Thus, if the phase-synchronous detection method and photon counting both work, people always choose to use the former one.

#### **1.3.4 Monochromators**

A monochromator is used to disperse the analyzed optical signal. The most commonly used dispersion elements are a grating or a prism. A narrow (quasi)-monochromatic part of the spectrum will be cut out by the exit slit, which is located at the output focal plane. If the exit slit is replaced by a detector, the monochromator is also called a spectrograph. There are 2 ways to tune a monochromator: manual scan or automatic scan by rotating the dispersion element. Nowadays, most spectrographs have 2 output channels. One is a slit for scanning monochromator mode and the other is a lateral output. The most common configuration for placing the dispersion element is shown in Figure 1.13. It is called Czerny-Turner type. The aim is to compensate the spherical aberration, astigmatism and coma.

In order to describe the properties of a monochromator, we focus on the following quantities: dispersion, resolving power and throughput.

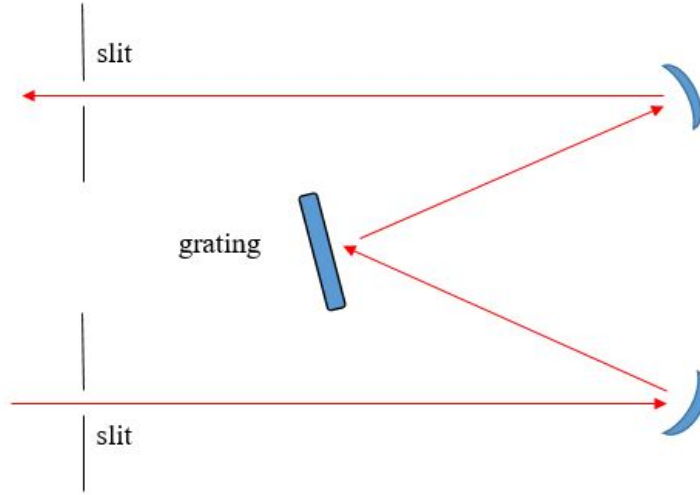


**Figure 1.13.** Czerny-Turner configuration.

Suppose that we have 2 incoming light beams with different frequencies. The difference of the wavelength is  $d\lambda$ . When they leave the dispersion element, the angular difference is  $d\theta$ . Then an angular dispersion is defined as

$$D = \frac{d\theta}{d\lambda} \quad (1.64)$$

In the spectrum, the separation of the related 2 spectral lines is  $dl$ . As mentioned earlier, the slit or detector is placed in the focal plane. Thus we may have the following relation between the separation  $dl$  and the focal length  $f$

$$dl = f d\theta \quad (1.65)$$

Finally we can define the linear dispersion  $L$

$$L = \frac{dl}{d\lambda} = fD \quad (1.66)$$

Its inverted value (so called reciprocal linear dispersion) is most used, and from this value we can obtain the spectral bandwidth  $\Delta\lambda$  if we know the slit width  $w$

$$\Delta\lambda = \frac{w}{L} \quad (1.67)$$

A typical value for the reciprocal linear dispersion is 1-10nm/mm.

Based on Eqn (1.67), we can reduce the slit width to obtain a smaller bandwidth, which means a higher spectral resolution. The resolving power  $R$  is typically defined as

$$R = \frac{\lambda}{\Delta\lambda} \quad (1.68)$$

It is limited just by diffraction, which is able to decrease the resolution. The main diffraction happens at the input slit and the dispersion element. It is also related to the size of the beam. If the diffraction at the input slit is negligible, we can deduce a so-called ultimate resolving power by taking Rayleigh criterion into account

$$R_u = \frac{\lambda}{\Delta\lambda} = \frac{Wd\theta}{1.22\Delta\lambda} = \frac{WD}{1.22} \quad (1.69)$$

where  $W$  is the lateral size of the beam. The above equation shows a close relation between the ultimate resolving power and the angular dispersion.

If we set a too small slit width, the diffraction at the input slit may not be negligible. Part of the input light may not be able to meet the dispersing element after the input slit. So the brightness of the final spectrum may drop significantly, which is fatal for low level luminescence. Moreover, that part of light may hit other components inside the device, causing many unwanted reflections. These reflections will increase the background signal and the signal to noise ratio will be reduced. An optimum value of the input slit width is given by [2]

$$w_{opt} = \frac{2f\lambda}{W} \quad (1.70)$$

Because of diffraction, light beams with different wavelengths may have the same diffraction angle. The different diffraction orders may overlap with each other, which is likely to cause

wrong interpretation of the spectrum from inexperienced experimenter. So a band-pass or edge filter for restricting the detected signal is always put in front of the input slit to solve the problem.

Throughput is an important quantity related to detection sensitivity. It can be defined by the use of the brightness  $B$  of an emitter, which is

$$B = \frac{\phi_i}{S \cos \theta \Delta \omega} \quad (1.71)$$

where  $\phi_i$  is the radiant flux emitted by an area  $S$  of the emitter.  $\theta$  is the angle between the normal to  $S$  and the radiation direction.  $\Delta \omega$  is a pertinent solid angle, which could be approximated by (Figure 1.14)

$$\Delta \omega = \frac{W^2}{f^2} \quad (1.72)$$

Then, the throughput is defined as

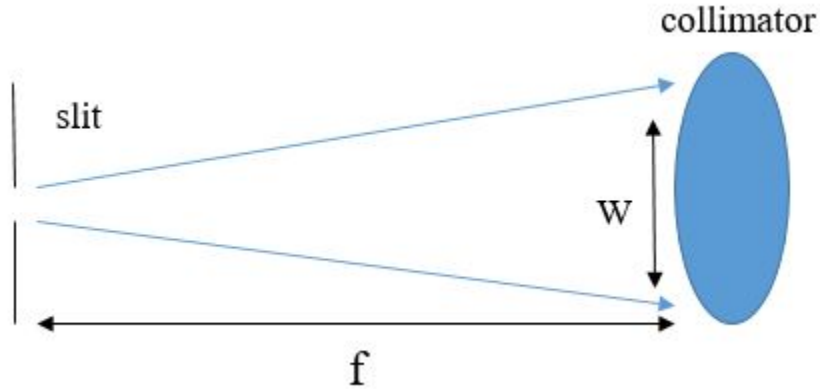


**Figure 1.14.** The aperture ratio of a spectral device.

$$\varphi_m = \frac{k(\lambda)\phi_i}{B} = k(\lambda)S \cos \theta \frac{W^2}{f^2} \approx k(\lambda)S \cos \theta \frac{A}{f^2} \quad (1.73)$$

where  $k(\lambda)$  is the coefficient related to the transmittance of all optical elements in the monochromator.  $A$  is the effective area of the dispersion element. A large throughput is



always preferred if the signal is not very strong. However, the throughput is actually inversely proportional to the resolving power as

$$\varphi_m = \frac{k(\lambda)hDW^2\lambda\cos\theta}{Rf} \quad (1.74)$$

where  $h$  is the height of the illuminated part of the entrance slit. Thus, for an experimenter, a compromise should be found based on experience.

In this thesis, steady state PL of nitride heterostructures was measured using a custom-made setup. This setup employs the reflection geometry for sample placement. The detector consists of a photomultiplier tube. The phase-synchronous detection method is used to collect PL signal. Time-resolved PL was also measured using a setup at National High Magnetic Field Laboratory. This setup has a detector made of an avalanche photodiode. The photon counting detection method is used to collect the PL signal after the excitation is switched off. The PL peak signal is selected by a monochromator before collection. More experimental detail will be introduced in Chapter 3.

## 2. INTRODUCTION OF III-NITRIDE SEMICONDUCTORS

III-nitrides are the compounds of group III elements with nitrogen. Typical III-nitride semiconductor materials are GaN, InN, AlN and their ternary and quaternary alloys. The band gaps of AlN, GaN, and InN are 6.2 eV, 3.4 eV, and 0.7 eV, respectively [12]. Thus, the direct

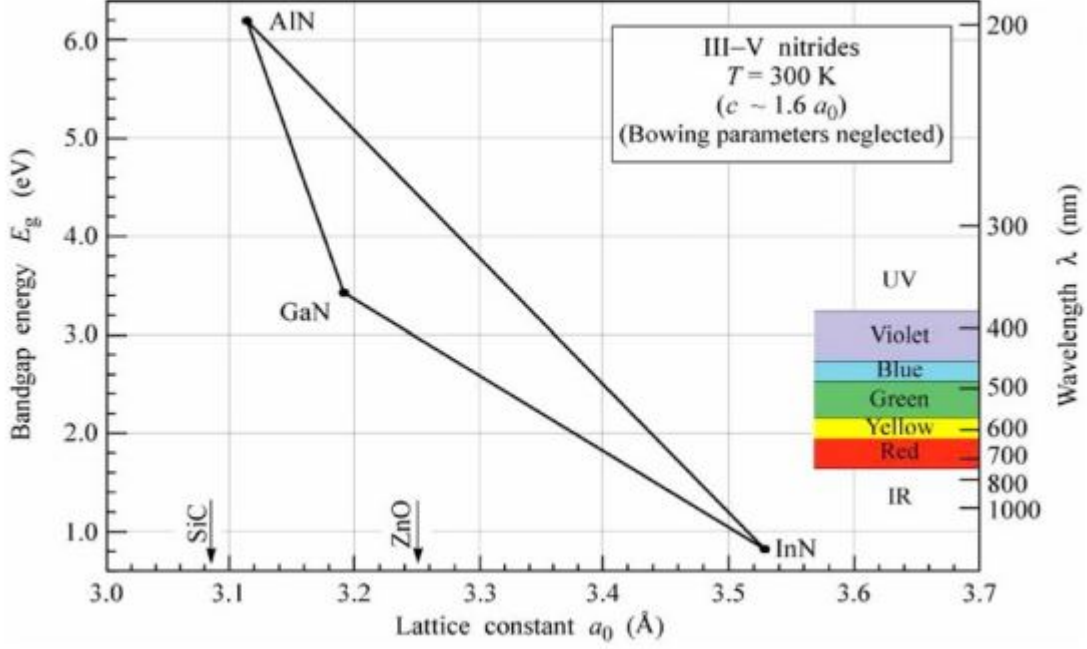


**Figure 2.1.** Band gap vs. lattice constant for III-nitride semiconductor materials [12]

band gap of III-nitride alloys system has a wide spectral coverage, ranging from deep ultra-violet to infrared region (Figure 2.1). Besides this characteristic, III-nitride materials also have high electron mobility, high thermal and chemical stability, high thermal conductivity, high breakdown voltage, high saturated drift velocity, etc [13], [14]. All of these exceptional properties make III-nitride semiconductor materials promising in various applications in optoelectronic devices. Wurtzite, zincblende and rocksalt are 3 possible structures of III-nitrides. Since the wurtzite structure is the most stable among them, most nitride devices have the wurtzite structure (Figure 2.2). To date, many III-nitride based devices have been demonstrated. In power and radio frequency electronics, III-nitrides are better alternatives

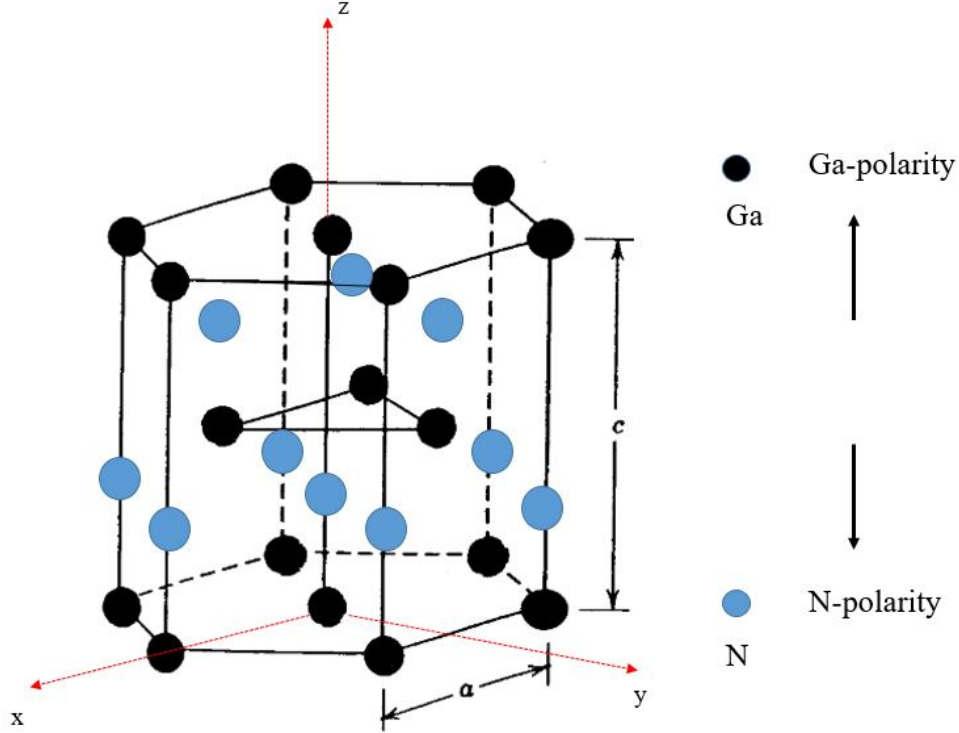


**Figure 2.2.** GaN with a wurtzite structure.

compared with silicon devices. GaN based field effect transistors have been demonstrated to have a 25 percent lower power loss than Si metal-oxide semiconductor field-effect transistors [15]. A large breakdown voltage up to 2000 V of GaN based heterojunction field effect transistors has been realized [16]. III-nitrides also lead to the development of solid state lighting industry. They are widely used to build light-emitting diodes (LED). Isamu Akasaki, Hiroshi Amano and Shuji Nakamura were awarded the Nobel prize in 2014 for the invention of III-nitrides based efficient blue LED. White LEDs with low cost and high efficiency have been realized by combining blue III-nitrides LED with yellow phosphor [17].

Many III-nitride devices make use of the transitions between the valence band and conduction band, i.e. interband transition. Intersubband transitions are also commonly used in some opto-electronic devices. Due to the large band gap range of III-nitride alloys, it is possible to build quantum wells with large conduction band offset or valence band offset. Thus, more than one electron energy level can be confined inside the quantum wells. The transitions between the confined energy levels inside the quantum wells are called intersubband

transitions (Figure 2.3). Since this kind of transition is mainly within the infrared region, it is

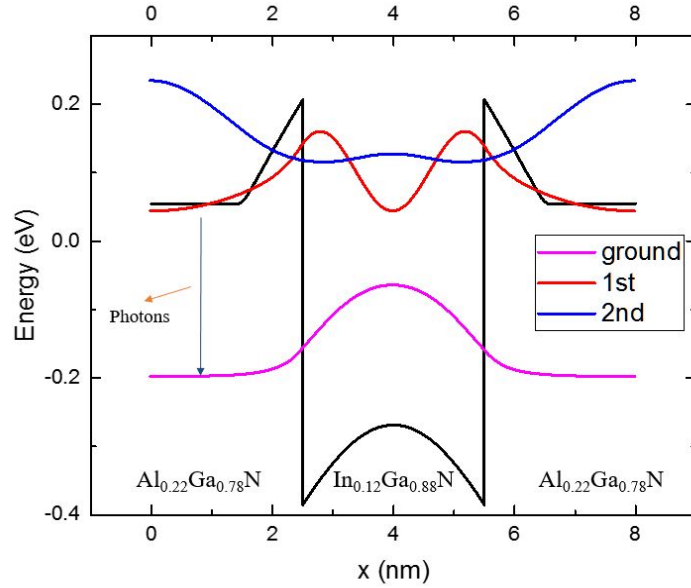


**Figure 2.3.** An example of intersubband transition in a non-polar m-plane quantum well ( $\text{Al}_{0.22}\text{Ga}_{0.78}\text{N}/\text{In}_{0.12}\text{Ga}_{0.88}\text{N}$ ). Three electron energy states are confined in the conduction band. The conduction band edge is depicted by black line. The wavefunctions are offset by energy levels.

widely used in the design of infrared devices. The use of intersubband transitions offers more freedom of the design of operation wavelength by adjustment of quantum wells and the band offset. Furthermore, the large energy of III-nitride longitudinal optical phonons (around 90meV [18]) is also beneficial for the implementation of intersubband devices and expands the possible operation wavelength range in the far infrared region. Near-infrared intersubband transitions have been demonstrated using III-nitride quantum wells, like  $\text{AlN}/\text{GaN}$  superlattices [19]. Kotani *et al.* reported mid-infrared intersubband transitions in m-plane  $\text{GaN}/\text{AlGaIn}$  heterostructures [20]. Edmunds *et al.* demonstrated far-infrared intersubband transitions in m-plane  $\text{GaN}/\text{AlGaIn}$  superlattices [21].

Although many III-nitride based optoelectronic devices have been invented and implemented in commercial use, there is still a need for more compact, rugged, higher efficiency devices with lower cost. There are many unique growth and fabrication challenges in the

research on III-nitride semiconductors. The most important challenges are related to lattice mismatch between different compounds and the internal polarization fields.

## 2.1 Lattice Mismatch

Due to different lattice constants of different III-nitride materials, lattice mismatch exists in heterostructures. The lattice mismatch usually leads to strain inside heterostructures, which affects the homogeneity of the sample structure. For instance, significant alloy inhomogeneity and interface roughness can be generated by strain for Al contents above 50% in AlGa<sub>N</sub> alloys [22]. Many kinds of defects like dislocations are generated, and eventually macroscopic cracks take place. Unfortunately, there is no lattice-matched alloy composition in GaN/AlGa<sub>N</sub> system [23], [24]. AlInN/GaN system can offer nearly lattice-matched structure, but clusters with high In composition have been observed in the samples [25]. Therefore we proposed a nearly strain-balanced structure of InGa<sub>N</sub>/AlGa<sub>N</sub> system to reduce the effect of strain. The implementation of strain balance will be discussed in the following chapters.

In addition to the lattice mismatch inside heterostructures, the lattice mismatch also exists between GaN and the substrate. For example, Sapphire is commonly used as the substrate to grow GaN. It has a different lattice constant with GaN. The lattice mismatch between Sapphire and GaN can generate a high defect density in the heterostructures, which hinders the vertical transport in devices [23]. In order to resolve this issue, free-standing GaN substrates were developed. Nowadays, commercially-available free-standing GaN can lower the density of defects drastically [26]. In this thesis, we used free-standing GaN substrates for all of our samples.

## 2.2 Internal Polarization Fields

Based on the wurtzite structure of GaN, heterostructures can be grown on 4 different kinds of planes [27]. We will focus on m-plane and c-plane (Figure 2.4) in the following discussion. Because of the low cost of c-plane substrates, many III-nitride devices are grown on c-plane. In a wurtzite structure, electric dipoles exist along the c-axis due to the low crystal symmetry and partly ionic nature of the chemical bond between neighboring group

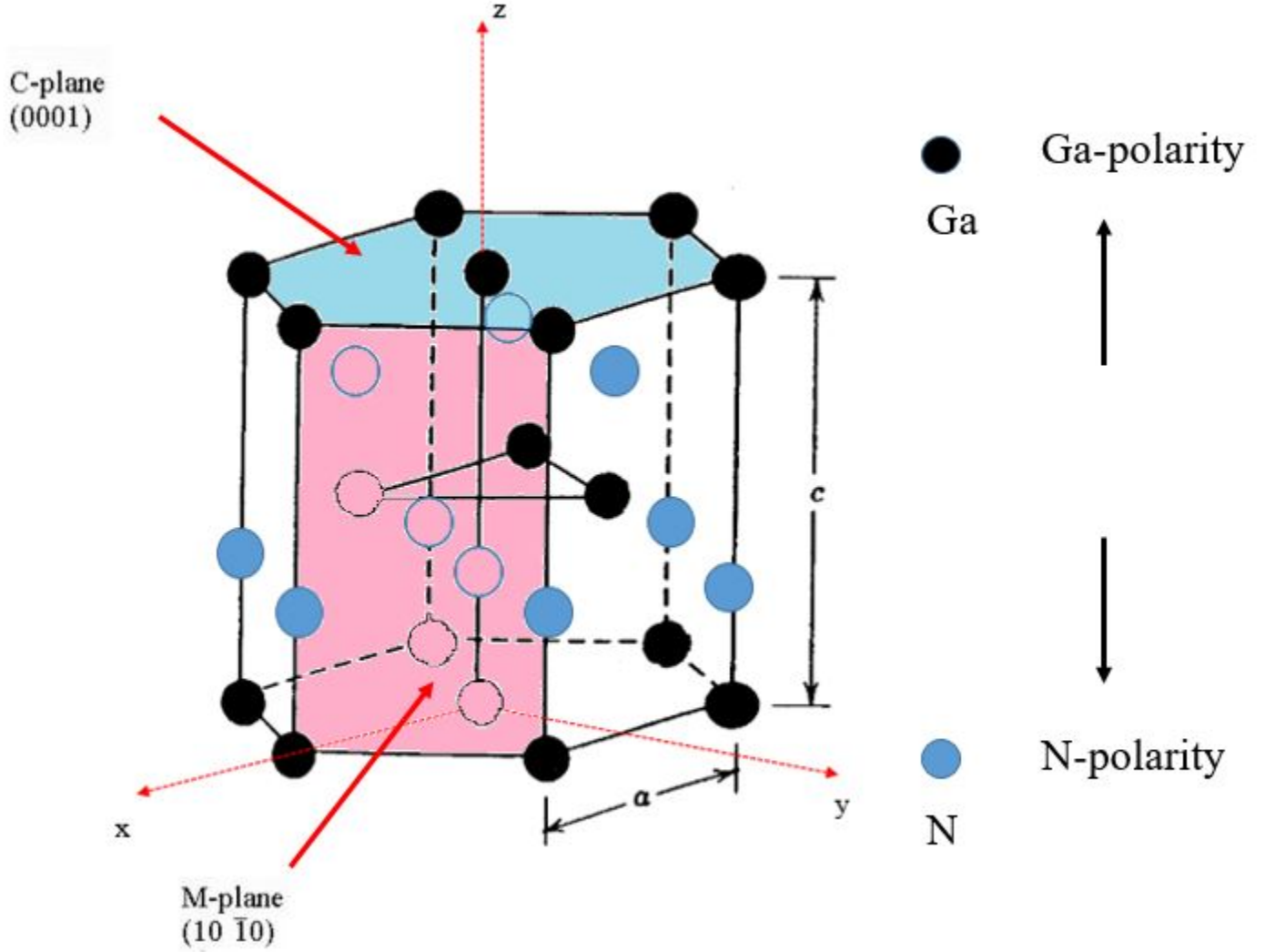


**Figure 2.4.** Schematic of the GaN c-plane and m-plane orientations.

III elements and Nitrogen atoms. In general, different III-nitride materials have different values of the electrical dipole. The discontinuity of dipoles at the heterojunction interface leads to accumulation of many bound charges, which results in an electrostatic field along the  $c$ -direction. This field is called spontaneous polarization field. Besides this field, another field which is called piezoelectric polarization field also exists due to the strain inside the crystal. The sum of these 2 kinds of polarization fields is called internal polarization field. It will strongly affect the band structure. The  $c$ -plane quantum wells are not rectangular any longer but triangular as shown in Figure 2.5.

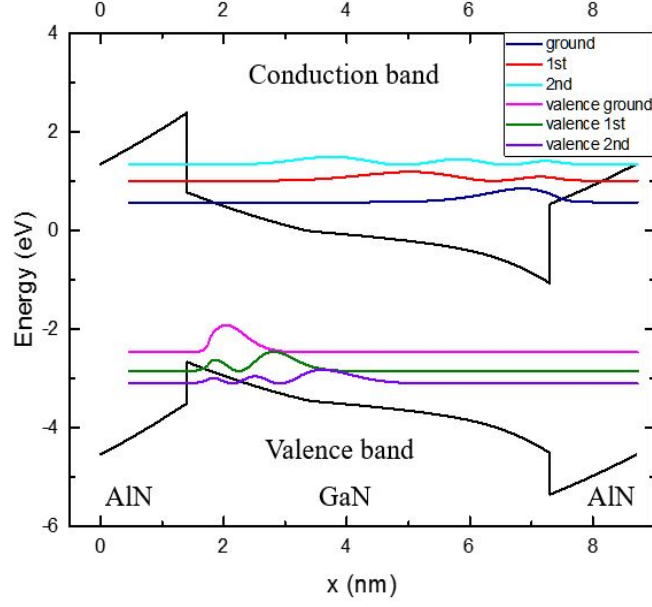


**Figure 2.5.** Band structure of a quantum well (AlN/GaN) grown on c-plane. The wavefunctions are offset by energy levels.

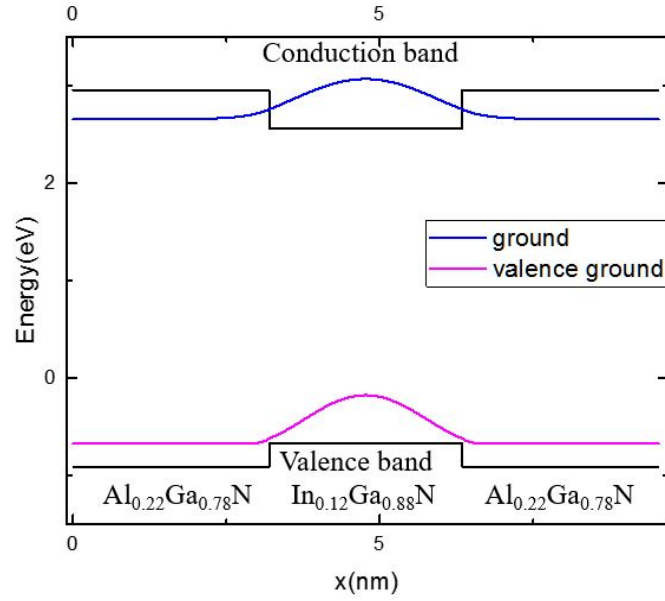


**Figure 2.6.** Band structure of a quantum well ( $\text{Al}_{0.22}\text{Ga}_{0.78}\text{N}/\text{In}_{0.12}\text{Ga}_{0.88}\text{N}$ ) grown on m-plane. The wavefunctions are offset by energy levels.

As seen in Figure 2.5, the tilted band structure reduces the overlap of wavefunctions, which significantly affects both interband and intersubband transitions, since the probability of transition between 2 energy levels is proportional to that overlap, according to Fermi's

golden rule. Furthermore, the triangle quantum well profile restricts the confinement of energy levels. The band engineering of intersubband devices is strongly affected by internal fields.

One popular solution to avoid the drawbacks of the internal polarization fields is to grow the device on m-plane (Figure 2.4) to obtain a non-polar quantum well (Figure 2.6) [28]. Then a symmetric band structure is obtained and the overlap of wavefunctions can be maximized. The absence of the polarization field has the potential to improve the performance of all nitride devices. However, many challenges appear in the growth of homogeneous samples on m-plane since the growth conditions are completely different from those for c-plane samples growth. Because of the adatom mobility difference between the c and the a-direction, the growth dynamics are different in the growth of m-plane structures.



### 3. EXPERIMENTAL DETAILS

#### 3.1 Growth of nitrides

All nitride structures investigated in this thesis were grown by Plasma Assisted Molecular Beam Epitaxy (PAMBE) at Purdue Birck Nanotechnology Center. The MBE system is equipped with conventional effusion cells for Indium, Gallium, and Aluminum. A Veeco Unibulb radio-frequency plasma source operated at 300 W forward power with 0.5 sccm of nitrogen ( $\text{N}_2$ ) flow is used to supply active nitrogen flux of  $\sim 6 \times 10^6$  atoms/ $\text{cm}^2 \cdot \text{s}$ . An effusion cell was used to provide Silicon for delta-doping.

Commercially available non-polar m-plane semi-insulating GaN substrates from Nanowin, Inc. were used in our growths. They have root-mean-square roughness less than 0.3 nm over  $16 \mu\text{m}^2$ , measured by atomic force microscopy (AFM). The size of the substrates is about  $5 \times 10 \text{ mm}^2$ . The nominal threading dislocation density is less than  $5 \times 10^6 \text{ cm}^{-2}$ . The miscut is  $-0.5^\circ \pm 0.2^\circ$  towards the c-axis.

The substrates were prepared by sonication in trichloroethylene, acetone, and methanol, rinsed with deionized water, and dried with  $\text{N}_2$  gas [29]. They were Ga-mounted to c-plane GaN host wafers that fit a standard MBE sample holder. WSi was pre-deposited on the backside of those host wafers to provide good thermal coupling and temperature uniformity [30]. The growth starts with a  $\sim 150 \text{ nm}$  GaN buffer layer grown at  $720^\circ\text{C}$  under Ga-rich conditions to achieve a smooth surface [30]. In order to obtain different In compositions, we adjusted the growth temperature of In containing nitrides in the range of  $450^\circ\text{C}$ – $635^\circ\text{C}$  [31].

#### 3.2 Structural characterization of nitrides

We used high-resolution x-ray diffraction (HRXRD) to obtain structural information about our samples. A PANalytical X'Pert-MRD high-resolution x-ray diffractometer equipped with a 4-bounce Ge monochromator was used to collect  $\omega - 2\theta$  spectra and reciprocal-space maps. The HRXRD diffraction patterns were simulated with the software package Epitaxy 4.5a from PANalytical to extract layer thicknesses and alloy compositions.

HRXRD structural information was confirmed and supplemented with high resolution high-angle annular dark-field scanning transmission electron microscopy (HAADF-STEM) data. The focused ion beam (FIB) in situ lift-out technique performed by a Thermo Scientific Helios G4 UX Dual Beam instrument was used to prepare the microscopy samples. At the end of the preparation process, the samples were polished at 500 V and 48 pA with the ion beam to further thin down the specimen and reduce the areas damaged by the high energy ion beam. Before loading into the microscope column, each sample was cleaned with a Fischione Ar plasma cleaner for 1 h to reduce possible specimen contamination. HAADF-STEM images were taken with an Aberration Corrected Thermo Scientific Themis Z electron microscope at 300 kV and 0.23 nA [31].

### 3.3 Steady state photoluminescence

In our lab, I designed and built a PL setup which can implement steady state PL measurements at temperatures ranging from 8 K to room temperature. I used a fluorescence spectrophotometer manufactured by Carry Eclipse. It contains a Xenon flash lamp, red-sensitive photomultiplier tube detectors and Schwarzschild collection optics. The Xenon flash lamp is intense enough to provide an excellent sensitivity. It provides excitation wavelength within the range from 190 nm to 1100 nm. The collection optics can capture a very large portion of the output signal to have a high signal to noise ratio. The detectors are capable of measuring a broad spectrum up to 900 nm without losing UV components. By the combination of all these things, the system is immune to environmental light.

Besides the Xenon flash lamp, I also set up a 325 nm He-Cd CW laser (Model 45-MRS-302-120) manufactured by Melles Griot Lasers Group as an alternative excitation source. The laser power is about 10 mW with an estimated excitation carrier density of  $6.3 \times 10^{11} \text{ cm}^{-3}$ . This is weak excitation so the band structure is not affected by it [32] and excitons can survive [33].

A brief layout of the setup is shown in Figure 3.1. The shutter can be turned on or off to choose the Xenon flash lamp or the 325 nm CW laser. The sample is placed in a reflection geometry. The optical excitation is incident on the sample, and the PL signal is collected

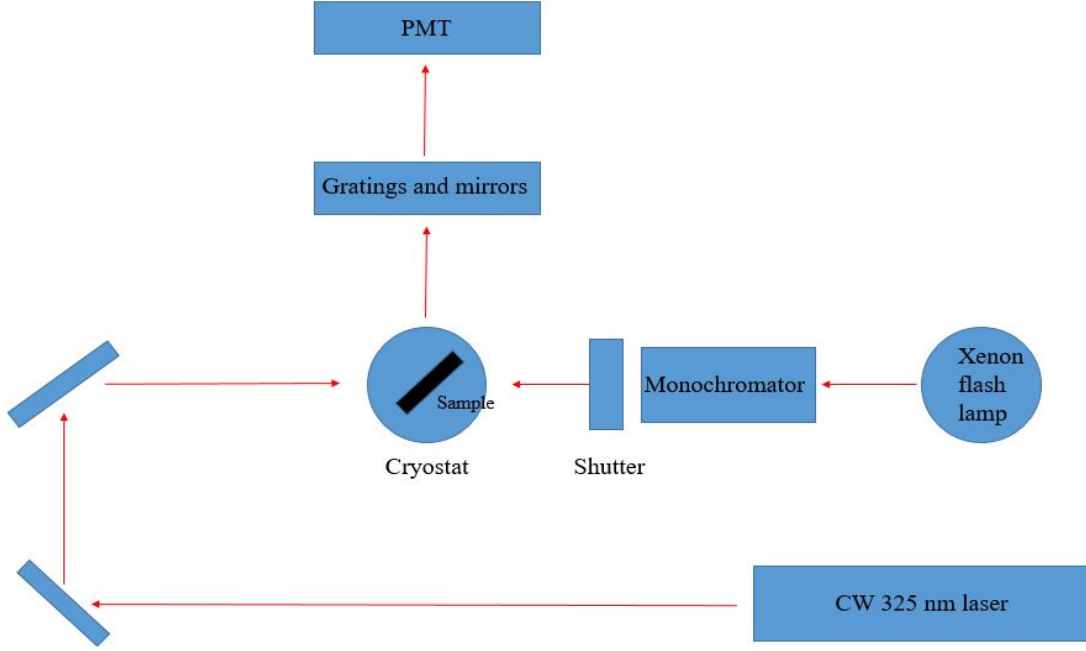


**Figure 3.1.** A diagram of the PL setup in our lab.

on the direction of reflection. The slit size of the detector can be adjusted according to experimental needs. The size options are 1.5 nm, 2.5 nm, 5 nm, and 10 nm. The larger slit size is selected, the more signal will be collected, but the smaller the resolution of PL spectrum will be. The detector also provides the ability to adjust the signal collection time to insure sufficient PL signal.

The samples were placed in a cryostat manufactured by Janis Research Company for low temperature measurements. Liquid Nitrogen or liquid Helium system is used to cool down the sample to either 80 K or 8 K. The temperature of the sample is measured by Temperature Controller Model 325 manufactured by LakeShore. The thermal sensor (manufactured by LakeShore, Model DT-470-SD-12A) is placed on the cold finger about 0.5 cm away from the sample. It is attached firmly to the sample holder to insure accurate temperature measurement of the sample. The temperature controller can be set to heat the sample so the temperature dependence of steady state PL measurement is available in the range from 8 K/80 K to room temperature or even higher.

The measurement procedures using Xenon flash lamp and He-Cd CW laser are slightly different. When the Xenon flash lamp is selected, the beam size of the excitation source can be adjusted by changing the size of slit. The slit size can be set as 1.5 nm, 2.5 nm, 5 nm, or 10 nm. An appropriate slit size needs to be set to make sure that the beam size is big enough to trigger PL signal as strong as possible. On the other hand, the slit size can not be too large to create too much reflection inside cryostat, which results in noise in PL spectrum. The PMT detector uses the phase-synchronous detection method to collect luminescence signal. It is coupled with the Xenon flash lamp, so the environmental light will not affect the PL spectrum and it does not need to be blocked in the measurements. The reflection of the excitation light from the surface of the sample will not affect the PL spectrum either.

When the He-Cd laser is selected, the beam size can not be adjusted, but it is big enough to trigger strong PL signal. Because the PMT detector is not coupled with the laser, the placement of the sample needs to be adjusted carefully or the PL spectrum will be affected. First, as introduced in [A.1](#), the sample placement needs to be adjusted to make sure the reflected light does not go into the detector. Based on my experimental experience, the best angle between the incident light and sample surface is about 43 degrees. Second, the environmental light needs to be blocked sufficiently to avoid it appearing in the PL spectrum.

For non-polar nitride heterostructures, the in-plane strain is anisotropic and the effective mass of holes changes depending on direction [\[34\]](#). This leads to the breaking of the crystal symmetry, which results in polarized PL signal. The polarization of the emitted light perpendicular to c-axis in the epilayer plane is shown in [Figure 3.2](#). Since the excitation sources used in our PL setup are unpolarized, a polarized PL measurement can be taken by inserting a linear polarizer in front of the detector. The sample is mounted with horizontal c-axis and the polarizer will be rotated to obtain the PL spectrum polarized along c-axis or perpendicular to c-axis. The degree of linear polarization (DLP) perpendicular to the c-axis is calculated as follows [\[35\]](#)

$$DLP = \frac{I_{\perp} - I_{\parallel}}{I_{\perp} + I_{\parallel}} \quad (3.1)$$

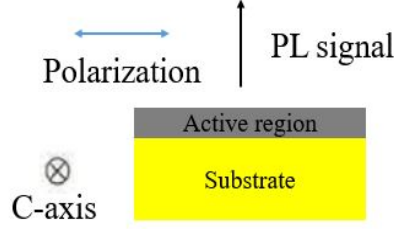


**Figure 3.2.** The polarization of the emitted light.

where  $I_{\perp}$  and  $I_{\parallel}$  denote the peak intensity in the PL spectrum polarized perpendicular to c-axis and along c-axis, respectively. DLP can be used to estimate the strain status of non-polar nitride heterostructures.

The excitation energy from the He-Cd laser is enough to pump electrons from valence band to conduction band in GaN. Considering the better monochromaticity and directionality of the laser, I mainly use the He-Cd laser in the PL study of (In)GaN/(In)AlGaN heterostructures.

### 3.4 Time-resolved photoluminescence

The recombination rate equations related to TRPL have been introduced in 1.1. In TRPL measurement, the sample is usually pumped by ultrashort laser pulses and the PL decay curve is measured after the excitation is shut off. A brief layout of a TRPL setup is shown in Figure 3.3. The PL decay is strongly dependent on the emission energy [2], so the excitation wavelength is generally selected as the peak wavelength in steady state PL measurement, and a monochromator or narrow-band interference filter is usually inserted in front of the detector. Perfect linear response to the PL signal, fast speed, and a high sensitivity are always required for a TRPL setup. Thus, a photomultiplier or photodiode is used to collect PL signal. However, a photomultiplier must contain many dynodes to achieve a high sensitivity. The statistical fluctuations of secondary emitted electrons will lead to a

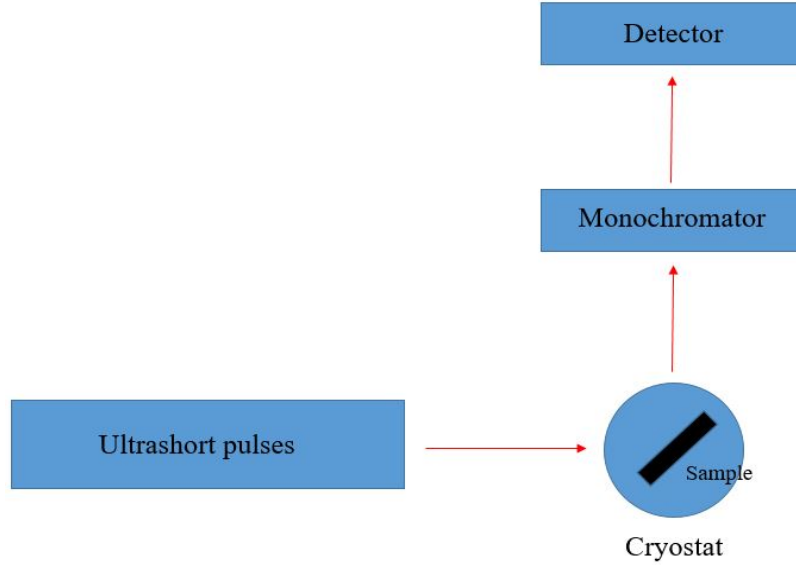


**Figure 3.3.** A diagram of a TRPL setup.

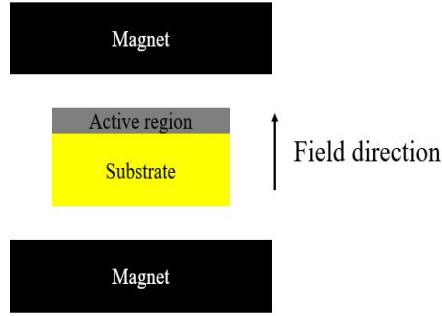


**Figure 3.4.** Faraday geometry.

worse time resolution. The decay time of our samples has a magnitude of nanosecond or sub-nanosecond. Therefore, a photodiode is used in our TRPL measurement.

Due to the short decay time of our samples, an excitation source with high frequency is required to accumulate enough statistics in a reasonable time for detection of PL decay curve. The frequency should be larger than 1 MHz [2]. Therefore, high-repetition laser pulses are used in our TRPL measurement. In order to not affect the band structure of our samples, weak excitation is applied, which results in non-intense PL signal. So a time-correlated photon counting method is used to generate PL decay spectrum from the non-intense signal.

This method is based on the fact that the number of emitted photons decreases in the decay process. The detail of how photo counting method generates PL spectrum has been introduced in [1.3.3](#)

Our TRPL measurements in this research work were performed in the group of Professor Khodaparast at National High Magnetic Field Laboratory. They were performed in a Helium flow-through cryostat from 2 K to 100 K temperature range. The excitation source is 784 nm pulses provided by a Mira 900 Ti:sapphire oscillator with a repetition rate of 80 MHz. A non-linear crystal was used to upconvert those pulses to 384 nm. Light emitted at the PL peak was selected using a monochromator and then collected from the sample in a reflectivity geometry using an avalanche photodiode. A Faraday geometry ([Figure 3.4](#)) was used for TRPL measurements in magnetic fields, where the direction of the field is perpendicular to the epilayer plane. A time correlated single photon counting system (PicoHarp 300) was used to determine the time between excitation pulse and emission of PL photons.

## 4. NON-POLAR INGAN THIN FILMS

In this chapter, we discuss our continuous-excitation PL investigation of non-polar InGaN layers. We have mentioned in Chapter 2 that we proposed a nearly strain-balanced structure. The way we design such a structure is to use the thickness weighted method:

$$\sum \epsilon_i t_i = 0 \quad (4.1)$$

where  $\epsilon_i$  is the strain and  $t_i$  is the thickness of each layer. This relation allows many combinations of different In compositions and thicknesses to achieve nearly balanced strain. However, current growth techniques can not provide non-polar m-plane In containing material with good structural quality for all indium compositions. Although intense research has been done on the growth of polar c-plane nitrides, the current optimized growth methods for c-plane nitrides can not be directly applied to the growth for m-plane nitrides, due to different growth dynamics and challenges of epitaxial growth [22], [28], [30], [36]. More research is needed to improve the growth for m-plane nitrides. On the other hand, there are much fewer published PL studies of non-polar m-plane In containing nitrides compared to c-plane nitrides. Among those PL studies of m-plane nitrides, most of them are using Metal Organic Chemical Vapour Deposition (MOCVD). So it is attractive to investigate PL of non-polar m-plane PAMBE grown InGaN. Therefore, we grew a series of InGaN thin films to investigate the effect of increasing In composition on PL.

**Table 4.1.** A series of non-polar m-plane InGaN thin films.

Sample	In composition (HRXRD)	Layer thickness	Buffer layer thickness
A	6.4%	25.5 nm	150 nm
B	11.0%	26.5 nm	155 nm
C	16.2%	29.4 nm	155 nm
D	21.0%	32.0 nm	155 nm
E	24.5%	31.5 nm	100 nm

These InGaN thin films have different In compositions within range from 6% to 26%. The structural information obtained from HRXRD is listed in Table 4.1. We measured steady



state PL spectra for these samples. The excitation source is a 325 nm continuous-wave He-Cd laser.

#### 4.1 Effect of In composition on continuous-excitation PL signal

Table 4.2 provides experimental PL peaks and FWHM of samples A-E at 80 K. In order to extract the peak energy and FWHM, we subtracted a linear background from the PL spectra and fit the corrected PL curve with a Gaussian function [37]. Figure 4.1 shows PL

**Table 4.2.** PL energies of InGaN thin films at 80 K.

Sample	Exp. peak position	Exp. FWHM
A	3.131 eV	68 meV
B	3.002 eV	53 meV
C	2.756 eV	83 meV
D	2.637 eV	78 meV
E	2.410 eV	105 meV

spectra of samples A-E at 80 K. All curves were normalized to their respective maximum. To the best of our knowledge, this is the first time when PL of non-polar m-plane PAMBE grown InGaN with average In composition up to 24.5% is reported.

To calculate the band gap of relaxed InGaN, we used the following formula [38], [39],

$$E_{In_xGa_{(1-x)}N} = xE_{InN} + (1-x)E_{GaN} - bx(1-x) \quad (4.2)$$

where  $b$  is the bowing parameter, which was taken to be 1.43 eV [38]. The band gap of GaN,  $E_{GaN}$ , and InN,  $E_{InN}$ , are 3.5 eV and 0.778 eV, respectively. They are calculated using the Varshni relation [40]:

$$E_g(T) = E_g(0) - \frac{\alpha T^2}{T + \beta} \quad (4.3)$$

where  $E_g(0)$  is the band gap at 0 K. This Varshni relation gives the band gap at a temperature,  $T$ .  $E_g(0)=3.51$  eV,  $\alpha=0.909$  meV/K,  $\beta=830$  K, and  $E_g(0)=0.78$  eV,  $\alpha=0.245$  meV/K,  $\beta=624$  K, are recommended by Vurgaftman *et al.* for GaN and InN, respectively [39].

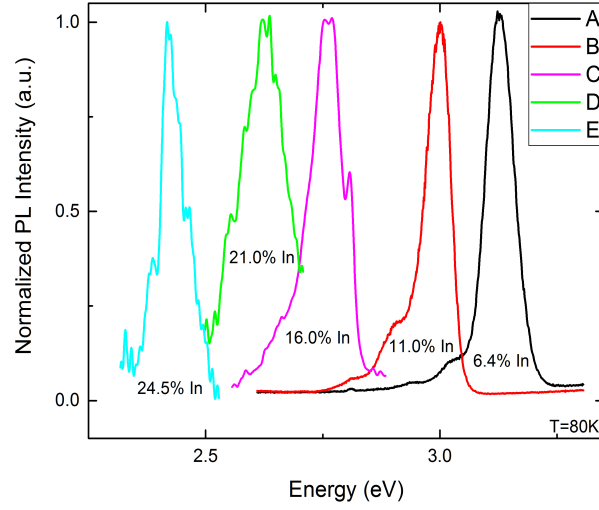


**Figure 4.1.** PL spectra of InGaN thin films A-E at 80 K. The PL curves of samples A-E were reduced by a factor of 545, 1000, 17.8, 8.5, and 2.2, respectively.

The band gap of strained InGaN was calculated by Nextnano software package using a self-consistent simulation.

As introduced in Section 1.2 of Chapter 1, the measured PL is likely from recombination of excitons. Therefore, all calculated PL transition energies were corrected to include the exciton binding energy. The estimation of the energy shift is 23.12 meV.

**Table 4.3.** Calculated PL peaks at 80 K and estimated In compositions from experimental PL.

Sample	Cal. peak position (relaxed InGaN)	Cal. peak position (strained InGaN)	Estimated In composition from Exp. PL (strained InGaN)
A	3.217 eV	3.280 eV	11%
B	3.037 eV	3.137 eV	15%
C	2.842 eV	2.979 eV	24%
D	2.668 eV	2.836 eV	28%
E	2.517 eV	2.662 eV	30%

All calculation results are listed in Table 4.3. The calculated peak energies of relaxed and strained InGaN are based on the nominal In compositions from HRXRD.

From HRXRD reciprocal space mapping, samples A-D are coherently strained on the GaN substrate, while sample E is partially relaxed [30]. However, we find that there is a discrepancy between calculations and experiments, by comparing Table 4.2 and Table 4.3. The experimental PL transition peaks are systematically smaller than theoretically calculated peak energies of either relaxed or strained InGaN films. The calculated energy of relaxed InGaN is closer to the experimental PL peaks, even though the samples were found to be strained. If we calculated the In compositions (shown in last column of Table 4.3) based on the experimental PL peaks, the In compositions are larger than the values from HRXRD. The composition difference ranges from 4%-7%. One possible reason is that the strain effect on the band gap is overestimated in our simulation. However, a more likely explanation is the inhomogeneous distribution of In [41]. Regions with high In compositions act as localization centers, and PL signals are due to the recombination of excitons located in these regions at low temperatures. However, In compositions extracted from HRXRD are averages over the entire film. They do not represent the In compositions of the regions where PL signals are produced. Therefore, we believe that In composition fluctuations can be as large as 7% in InGaN films with In composition larger than 21%.

From Figure 4.1, we find that the PL peak intensity of samples C-E is much weaker than that of samples A and B. PL curves of samples C-E look less smooth than those of samples A and B. This indicates that much more non-radiative recombination takes place in InGaN films with more than 16% In. We note that strong PL signal at 80 K has been observed for MOCVD grown polar c-plane InGaN films with In composition larger than 11% [42], which shows the non-radiative recombination is not dominant. One possible reason is the differences between band structures of polar InGaN and non-polar InGaN. As introduced in Section 2.2 of Chapter 2, c-plane InGaN has a tilted band structure, while m-plane InGaN has a symmetric band structure. Although the band tilting separates wave functions of electrons and holes, it helps localization of both electrons and holes, which prevents them from getting trapped by non-radiative recombination centers. On the other hand, the growth process by PAMBE may introduce more non-radiative recombination centers in our m-plane

InGaN films, especially for high In compositions. The requirement of decreasing growth temperatures for large In incorporation leads to accumulation of defects. The possible partial release of the strain when the critical thickness of the epilayers is reached introduces higher density of defects [30], which can act as non-radiative recombination centers.

A model was proposed to calculate the relation between the FWHM of PL peak and the In composition [42], [43]. This model assumes the random In distribution in InGaN films obeys a binomial distribution. It ignores any alloy inhomogeneities in the growth or lateral direction. Other broadening mechanisms, such as broadening from alloy clusters or defects, are also excluded. The theoretical calculation from this model shows that as In composition increases, FWHM increases when In composition is less than 15%, reaches a maximum when In composition is around 15%, and decreases when In composition is larger than 15% [42]. This is different from our experimental results. From Table 4.2, sample B has the smallest FWHM among all samples. The In composition of sample A is less than that of sample B, but its FWHM is about 15 meV larger. Samples C-E have much larger FWHM than samples A and B. Experimentally for In composition larger than 16%, the FWHM increases as In composition increases. The calculated FWHM for InGaN with 11% In is 42 meV, which is close to experimental FWHM of sample B (53 meV). The FWHM of sample B is the closest to the calculated value among all samples. Furthermore, sample B has the strongest PL peak intensity of all samples. We attribute this to the improved material quality of sample B. The material quality of samples C-E may be the reason why their PL signals are very weak at 80 K compared with polar c-plane InGaN films with similar In compositions. Although the FWHM of our m-plane samples is comparable to some reported values for c-plane thin films with similar In compositions [42], many other c-plane InGaN thin films are reported to have 3-4 times broader FWHM than the theoretical calculation [44]–[46].

## 4.2 Effect of temperature on continuous-excitation PL signal

We measured PL spectra of each sample within a temperature range of 80 K to 280 K. Figure 4.2 provides the temperature dependence of PL curves for sample B. We observed similar temperature dependence spectra for other samples. At 80 K, the tiny shoulder around

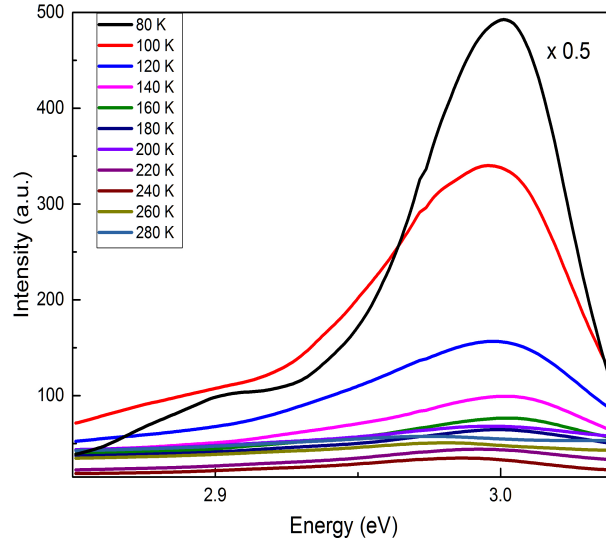


**Figure 4.2.** Temperature dependence of PL spectra for sample B.

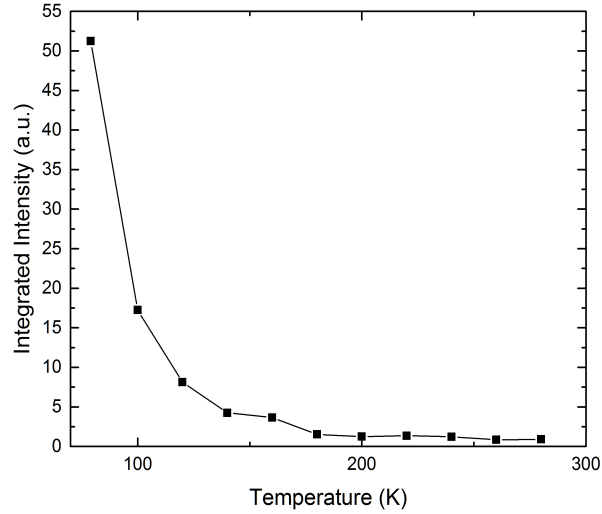


**Figure 4.3.** Temperature dependence of integrated PL intensity for sample B.

2.9 eV is attributed to longitudinal-optical (LO) assisted emission. It is obvious in Figure 4.2 that PL intensity decreases dramatically as temperature increases. The internal quantum efficiency (IQE) of a material is important for its application in design and fabrication of optical devices. Usually IQE is estimated from integrated PL intensity [47]. It is defined

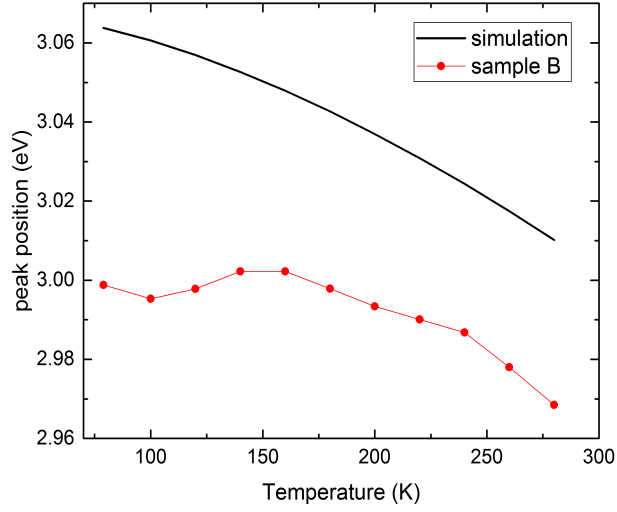


**Figure 4.4.** Temperature dependence of PL peak energy for sample B.

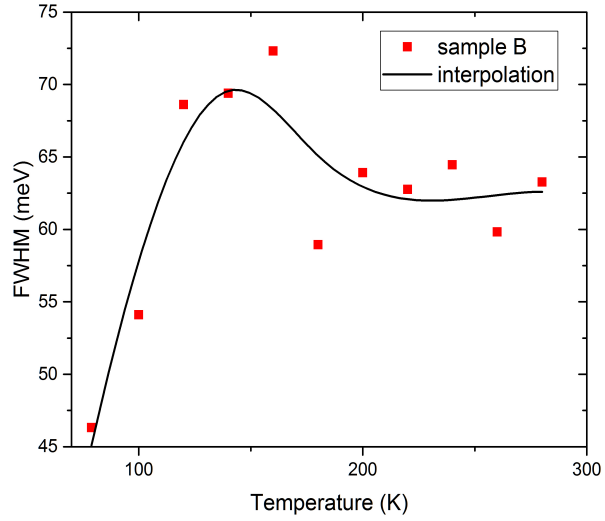


**Figure 4.5.** Temperature dependence of PL FWHM for sample B. The black interpolation line is a guide to the eye.

as the ratio of the integrated PL intensity at room temperature relative to that at lowest temperature. By numerical integration over the measured energy range, we calculated the integrated PL intensity and plotted it in Figure 4.3 for sample B. From 80 K to 280 K,

its IQE drops almost 96%. This indicates that non-radiative recombination increases significantly and becomes the main recombination process when temperature is close to room temperature. For polar c-plane InGa<sub>N</sub> films with similar In compositions, strong PL signal is still reported at room temperature [47]. As discussed earlier in this chapter, one possible reason is the difference in band structures between c-plane and m-plane nitrides ( see Section 2.2 of Chapter 2). The band tilting in c-plane nitrides increases localization of excitons and prevents them from getting trapped by non-radiative recombination centers even at high temperature, which consequently enhances IQE. Another possible reason is that our growth process for m-plane InGa<sub>N</sub> films (PAMBE) introduces more non-radiative recombination centers than other growth techniques for c-plane InGa<sub>N</sub> films such as MOCVD.

Figure 4.4 plots the temperature dependence of PL peak energy for sample B. The simulation curve is obtained using Eqn. (4.2) and Eqn. (4.3). We found the experimental temperature dependence curve is not monotonic as the simulation curve indicates. A similar phenomenon was reported for many c-plane InGa<sub>N</sub> films [46], [48]. The curve was referred to an "S-shape" curve and was attributed to the localization centers in InGa<sub>N</sub> films. At low temperatures, excitons are more likely localized in those localization centers and produce radiative recombination centers. As temperature increases, those excitons may still stay in the original localization centers, or become delocalized. If excitons stay in the original localization centers all the time as temperature increases to room temperature, the temperature dependence curve of PL peak energy should be similar with our simulation for the band gap change. If excitons delocalize after the temperature is larger than some threshold, they will relocalize in some other localization centers which have different localization depth from the original localization centers and then emit PL. In this situation, PL peak energy will have a different temperature dependence curve from the simulation. For different In compositions, the distribution and properties of localization centers are different. Thus, the temperature dependence of peak energy may vary in InGa<sub>N</sub> films with different In compositions.

Figure 4.5 shows the temperature dependence of FWHM for sample B. It is comparable to reported temperature dependence curves of MOCVD grown polar c-plane InGa<sub>N</sub> films with similar In composition. The temperature dependence curve is expected to be a monotonic curve, since impurity scattering increases as temperature increases. However, due

to the exciton relocation process discussed above, the FWHM decreases slightly when temperature approaches room temperature.

### 4.3 Summary

Continuous-excitation PL of PAMBE grown non-polar m-plane InGa<sub>N</sub> thin films has been investigated. This is the first report of PL spectra of m-plane InGa<sub>N</sub> films with In composition up to 24.5%. The experimental PL peak energies are found systematically smaller than calculated band gap energies of either relaxed or strained InGa<sub>N</sub> films. For In composition larger than 16%, m-plane InGa<sub>N</sub> films have very weak PL signals at 80 K, while c-plane InGa<sub>N</sub> films have been reported to have strong PL signal. As temperature increases, IQE of our m-plane InGa<sub>N</sub> films drops dramatically, and the PL peak energy does not follow the theoretical expectations. The PAMBE grown non-polar m-plane InGa<sub>N</sub> film with 11% has a FWHM close to the theoretical calculation for InGa<sub>N</sub> with random In distribution, and much smaller than many reported polar c-plane InGa<sub>N</sub> films with similar In compositions.

We believe that inhomogeneity of In distribution exists in non-polar m-plane InGa<sub>N</sub> thin films. The composition fluctuation can be as large as 7% in InGa<sub>N</sub> with In composition larger than 21%. The recombination of excitons in regions with high In composition contributes to the PL signals. As temperature increases, relocation of excitons takes place. The symmetric band structure of m-plane nitrides helps reduce FWHM of PL peak, but affects localization of excitons. The growth process for m-plane InGa<sub>N</sub> films by PAMBE may introduce more non-radiative recombination centers than growth processes by other techniques such as MOCVD.

M-plane InGa<sub>N</sub> thin films with 11% In are believed to have improved material quality for our PAMBE growth conditions. They can be grown coherently on GaN and have smooth morphology [30]. Therefore, we selected to choose In composition around 11% for the design of nearly strain-balanced InGa<sub>N</sub>/AlGa<sub>N</sub> superlattices.



## 5. NEARLY STRAIN-BALANCED NON-POLAR M-PLANE INGAN/ALGAN SUPERLATTICES

From the PL investigation of a series of non-polar m-plane InGaN films, we found our optimal growth conditions by PAMBE improved material quality of InGaN thin films with approximately 11% In. Considering the thickness weighted method we use for strain-balance design and the growth of AlGaN, we eventually choose 9% as the In composition. In order to minimize alloy inhomogeneity and interface roughness, Al composition was selected to be 18.8%. Then QW thickness and barrier thickness were selected to nearly balance the tensile strain of AlGaN barriers with the compressive strain of InGaN QWs. Finally, the superlattices achieve balanced strain along  $(\bar{1}2\bar{1}0)$  direction (a-direction) and less than 0.3% tensile strain along (0001) direction (c-direction). Table 5.1 provides detail of structural

**Table 5.1.** A series of m-plane InGaN/AlGaN superlattices.

Sample	Al/In composition	Barrier/QW thickness	Doping profile
F	16.5%/0	3.30 nm/3.00 nm	undoped
G	18.8%/9.0%	6.40 nm/3.15 nm	undoped
H	18.8%/8.7%	6.40 nm/2.95 nm	10 s delta-doped
I	18.8%/8.5%	4.84 nm/2.20 nm	10 s delta-doped
J	18.8%/9.3%	6.40 nm/2.95 nm	20 s delta-doped
K	18.8%/9.1%	6.40 nm/2.60 nm	20 s delta-doped

information obtained from HRXRD for the series of superlattices discussed in this chapter. The superlattices consist of 15 QWs separated by AlGaN barriers.

Sample F is actually a GaN/AlGaN superlattice added for reference. Sample I has a thinner QW than other samples, so its barrier thickness is also reduced to achieve the nearly balanced strain. The doping material is Silicon. We utilize delta-doping in our superlattices to provide electrons as donors. This doping method consists of a roughly 0.2 nm thin (one monolayer) doped Si layer in the barriers. The doping position is about 1 nm away from each interface of barrier and QW. The doping time indicates the deposition time of a single delta-doping layer and it is used to represent the doping level. The dopant density of a 10 seconds doping is about  $2 \times 10^{14} \text{ cm}^{-2}$ . Sample K also has an additional 100 nm doped

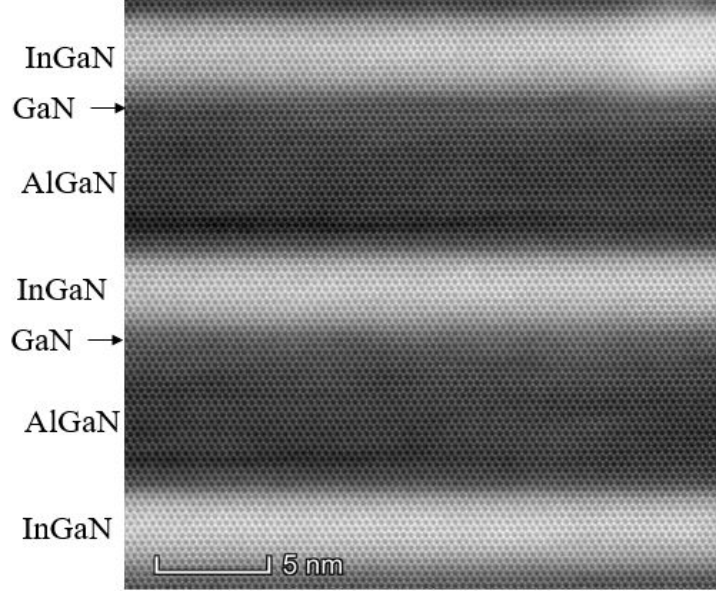
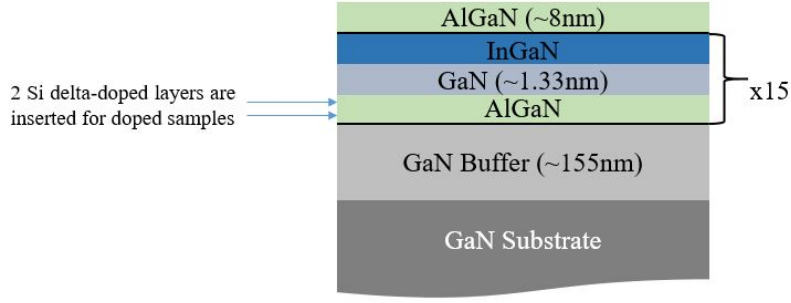
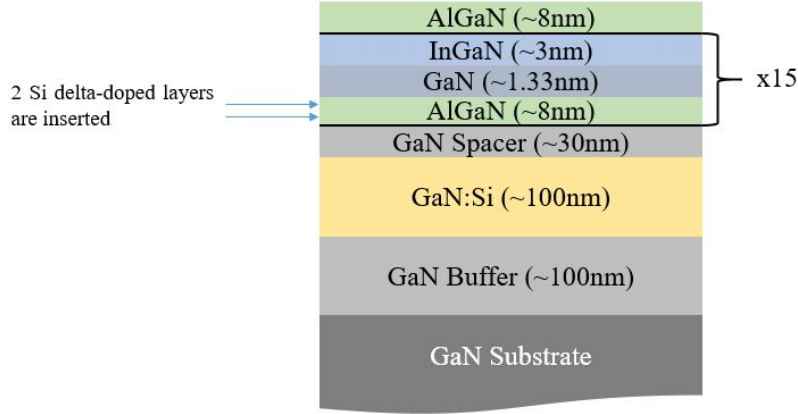


**Figure 5.1.** HAADF-STEM image of sample J. The darker layers are AlGaN, while the lighter layers are InGaN.

GaN layer with a doping density of  $8 \times 10^{14} \text{ cm}^{-3}$  underneath the active region. A 155 nm GaN buffer layer is grown between the substrate and the quantum well region for all the samples except sample K, which has a 100 nm buffer layer. Sample F also has an 18 nm GaN cap layer. After careful examination of HAADF-STEM images (Figure 5.1), we do not find formation of dislocation for these superlattices, but presence of an unintentional around 1.3 nm GaN layer was identified on top of each barrier for all InGaN/AlGaN superlattices. This is due to excess Ga accumulation during barrier growth and preferential incorporation of Ga in QWs. Figure 5.2 shows the sketch of the structure for the samples in Table 5.1. For many reported non-polar m-plane InGaN/GaN QWs grown by Metal Organic Vapour Phase Epitaxy (MOVPE), the formation of semi-polar QWs is identified at the step bunches [49], [50]. We did not find such semi-polar facet formation in HAADF-STEM images of our superlattices.



(a) Sketch of structure for samples F, G, H, I and J.



(b) Sketch of structure for sample K.

**Figure 5.2.** Sketch of structure for all samples.

**Table 5.2.** Measured PL peak energies and FWHMs as well as calculated peak energies at 80 K for samples F-K.

Sample	Exp. peak position	Cal. peak position	Exp. FWHM
F	3.53 eV	3.547 eV	70 meV
G	3.07 eV	3.293 eV	73 meV
H	3.06 eV	3.297 eV	117 meV
I	3.12 eV	3.348 eV	99 meV
J	3.07 eV	3.280 eV	172 meV
K	3.09 eV	3.303 eV	133 meV

## 5.1 Discussion of continuous-excitation PL spectra

We measured steady state PL spectra for the superlattices in Table 5.1. The excitation source is a 325 nm continuous-wave He-Cd laser. The estimated excitation carrier density is

$6.3 \times 10^{11} \text{ cm}^{-3}$ . The photon energy of the laser is smaller than the band gap of our barriers, and the excitation is weak. Therefore, the carrier diffusion from AlGaIn barriers will be avoided, and the monomolecular process will be the dominant process in our PL measurements. Table 5.2 provides measured PL peak energies and FWHMs as well as calculated peak energies at 80 K for all samples in Table 5.1. We extracted PL peak information from obtained PL spectra and calculated PL peak energies in the same way we did for strained InGaIn thin films in Chapter 4. The exciton binding energy correction was also included in the calculation.

### 5.1.1 PL peak position

From simulations, the In composition and QW size determine PL peak position. Samples G, H, J, and K have similar In compositions and QW sizes, so their measured PL peak energies are close to each other, even though their doping profiles are different.

For the InGaIn/AlGaIn superlattices in Table 5.2, there is a significant discrepancy between the calculated and measured PL peak energy. The discrepancy is larger than what we observed earlier for the strained InGaIn thin films.

We first consider the exchange effect in QWs. The excited electrons are likely in the ground state of QW. In doped superlattices, the electrons provided by the donors are also likely in the ground state. The exchange effect can lead to an energy shift of the ground state, which is given by [51]

$$E_{exchange} = -\frac{e^2}{2\epsilon\epsilon_{stat}} \int_{-\infty}^{\infty} dz \int_{-\infty}^{\infty} dz' \int_0^{k_F} dk' \frac{e^{-k'|z-z'|}}{2\pi k'} \psi^2(z') \psi^2(z) \quad (5.1)$$

where  $k_F = \sqrt{2\pi\sigma}$  is the Fermi wavevector.  $k'$  is the in plane wavevector.  $\epsilon_{stat}$  is the static dielectric constant.  $\psi$  is the wave function. The energy shift  $E_{exchange}$  is less than 0, because the system reaches a stable state with lower energy. Our original calculation with Nextnano software does not consider this energy shift. So we calculated this energy correction and revised the calculated peak position at 80 K for samples H, I, J and K. The results are listed in Table 5.3. A better agreement between experimental energies and calculation is obtained. Furthermore, we applied this exchange effect in the calculation of

**Table 5.3.** Revised calculated PL peak for doped samples H, I, J and K at 80 K including exchange correction.

Sample	Exp. peak position	Cal. peak position (revised)
H	3.06 eV	3.074 eV
I	3.12 eV	3.187 eV
J	3.07 eV	3.087 eV
K	3.09 eV	3.109 eV

PL peak at other temperatures. Here we take sample H as an example for this revised calculation. We plotted the temperature dependence curves of both experimental PL peak energy and revised calculated peak energy in Figure 5.3. We find that the exchange effect

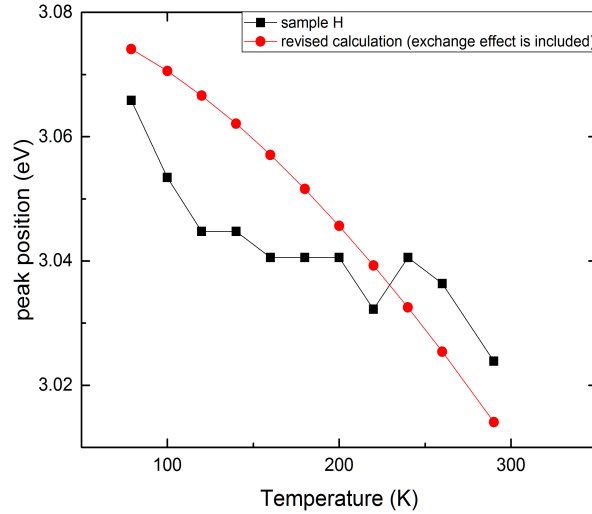


**Figure 5.3.** Temperature dependence of PL peak position for sample H.

energy correction reduces the discrepancy at other temperatures as well.

However, the exchange effect energy correction is almost 0 for sample G. This is because the density of the excited electrons is too low to generate a significant energy shift in this undoped superlattice. Furthermore, there is no such significant discrepancy between calculation and experiment for undoped GaN/AlGaN superlattices (sample F). This indicates

that the exchange effect energy shift may not be the dominant reason to cause the energy discrepancy. The incorporation of In is more likely the main reason.

In Chapter 4, we have shown that for the observed discrepancy In composition fluctuations in InGaN can be as large as 7% for high In composition. The growth of QW structures may increase the fluctuations and the quantum confinement in QWs likely enhances the effect of those fluctuations on PL transition energies. We found that our measured PL energies correspond to an average In composition of about 17%, which is almost twice as the In composition obtained from HRXRD. We believe that there are regions with 17% In in our QWs.

In the calculation for band gap of InGaN films, we realized that the band gap of relaxed InGaN is closer to measured PL peak energy than that of strained InGaN. So whether our InGaN/AlGaN superlattices are strained or not may also contribute to the discrepancy between calculated PL peak energy and measured PL peak energy. In order to check the strain status, we performed polarized PL measurements. Here we take sample H as an example. Figure 5.4 shows the measured polarized PL spectra for it at 80 K.

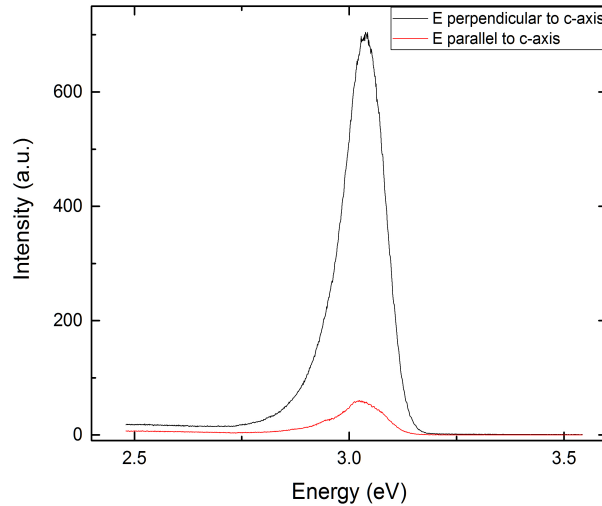


**Figure 5.4.** Polarized PL spectra at 80 K for sample H.

The calculated DLP of sample H at 80 K is approximately 83%, which is comparable to previously reported results [35], [52], [53]. This indicates that our QWs are bi-axially strained, which agrees with what we observed for InGaN thin films in Chapter 4.

The presence of strain will affect the band gap of the QW, usually resulting in a larger band gap. However, it is hard to precisely estimate how much larger band gap the strain may lead to. For example, inaccuracies of deformation potentials may cause large errors for the calculation results. Therefore, we believe the overestimation of strain for the band gap of the InGaN QW is a possible alternative explanation for the discrepancy between experiments and calculations.

### 5.1.2 Broadening of PL spectra

Although the incorporation of In in the QW is likely to cause the discrepancy between experiments and calculations in terms of PL peak energy, it turns out that the In incorporation does not affect the inhomogeneous broadening mechanism of the superlattice structure. Sample F is an undoped GaN/AlGaN superlattice and it has similar Al composition and QW thickness as sample G, which is an undoped InGaN/AlGaN superlattice. They have similar FWHM at 80 K (Table 5.2), which suggests that the inhomogeneous broadening mechanism is similar for undoped InGaN/AlGaN and GaN/AlGaN superlattices. Samples G, H and J have similar Al and In compositions, QW thicknesses, but different doping profiles. By comparing the FWHM of these 3 samples, it is obvious that FWHM increases as doping amount increases. We attribute the additional broadening to the rapidly increased impurity and electron-electron scattering as the dopant density increases. Nevertheless, additional inhomogeneity and surface roughness caused by Si delta-doping cannot be excluded as possible sources for the broadening. Moreover, the simulation indicates that the density of ionized donors is only about  $10^{13} \text{ cm}^{-2}$ , which is around 1/20 of the impurity density. Thus, both  $D^+-X$  and  $D^0-X$  occur in the doped superlattice. The dissociation energy will be very close to each other since the donor in these 2 recombination channels is the same. And due to the resolution limit in our PL system, we can not resolve the fine structure of the PL spectrum

from QWs. So the complex of recombination channels induced by Si delta-doping is also a possible cause for the broadening.

Sample I has a thinner QW than the other superlattices. In general, the smaller QW thickness leads to more impurity and electron-electron scattering inside the QW, which results in larger FWHM. However, sample I has an approximate 18 meV smaller FWHM than sample H, which has a similar structure and doping profile with sample I except QW thickness. We speculate that this situation is due to faster recombination. It has been reported that the QW thickness affects the recombination rate significantly, and the recombination rate is larger in a smaller QW [54]. The faster recombination reduces the possibility that excitons get trapped by different localization centers. Due to the In fluctuation, localization centers are not uniform inside QW. PL transitions from different localization centers contribute to the FWHM of the resultant PL curve. The fewer the localization centers where excitons get trapped to produce PL signal, the smaller the broadening of the PL spectrum. However, we cannot completely exclude the effect of thin QW on alloy composition and interface roughness, which are also important sources for broadening.

In conclusion, the broadening of PL spectra in InGa<sub>N</sub>/AlGa<sub>N</sub> superlattices is complex. Many possible sources contribute to the broadening.

### 5.1.3 Effect of temperature on continuous-excitation PL

In order to investigate the effect of temperature on PL signal, we took steady state PL measurement within a temperature range of 8.3 K to 290 K. Figure 5.5 provides the PL curves at different temperatures for sample G. We observed similar spectra for the other superlattices.

We find that the PL intensity drops significantly as temperature increases. To estimate IQE, we calculated the integrated PL intensity by numerical integration over the measured energy range, and plotted it in Figure 5.6. The plot shows that IQE drops about 91% as temperature increases to room temperature. We observed a similar behavior in the PL investigation of InGa<sub>N</sub> thin films. So we believe the cause is the same for InGa<sub>N</sub> thin films and InGa<sub>N</sub>/AlGa<sub>N</sub> superlattices. As temperature increases, a large number of excitons begin to



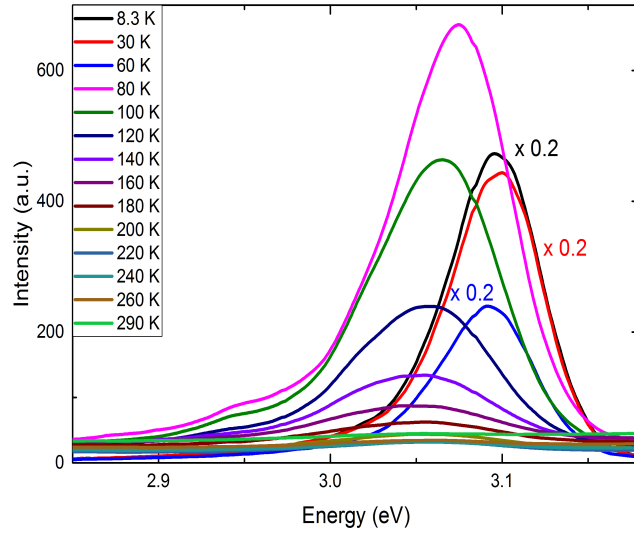


**Figure 5.5.** PL spectra at temperatures from 8.3K to 290K for sample G.

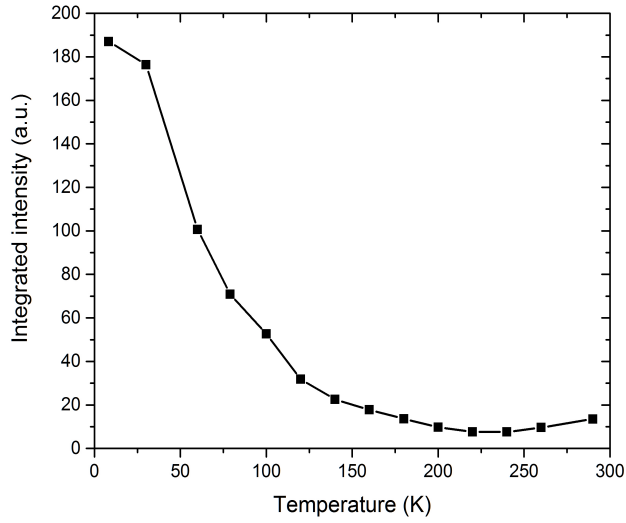


**Figure 5.6.** Temperature dependence curve of PL integrated intensity for sample G.

get trapped by non-radiative recombination centers, and non-radiative recombination process becomes dominant, leading to a sharp decrease of IQE. However, we notice that several studies of single or multiple non-polar m-plane QWs grown by MOCVD with comparable In compositions are reported to have a less than 90% IQE drop when temperature increases

to room temperature [34], [41], [49], [55]–[60]. So we believe our PAMBE growth technique introduces larger densities of non-radiative recombination centers than MOCVD. The additional non-radiative recombination centers are likely due to the lower growth temperature.

At low temperatures for sample G, there are small peaks on the low energy side of the main PL peak. These peaks are also observed in PL spectra of InGaN thin films. They are related to electron-phonon coupling, so the main peak is called "zero-phonon" line while those tiny peaks are called "phonon replicas". The peak position difference between the main peak and the tiny peak is about the LO phonon energy, which is about 90 meV. In doped superlattices (samples H-K), we do not see those phonon replica. This is because the Si doping blocks the LO assisted emission.

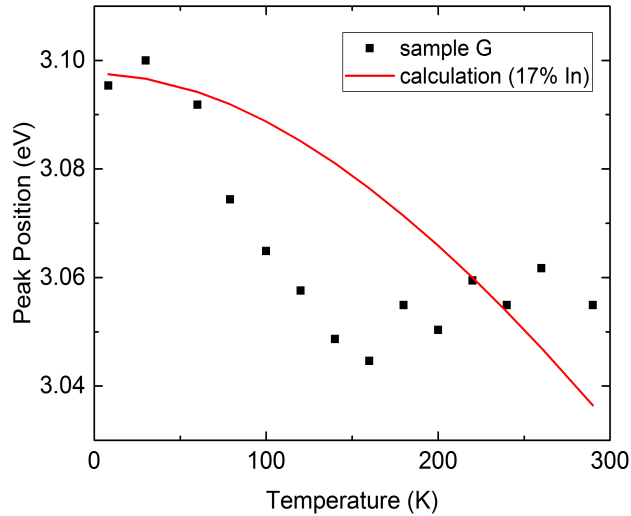


**Figure 5.7.** Temperature dependence curve of PL peak position for sample G. The red line is the calculation of the PL transition energy from Nextnano software package using self-consistent simulation for a InGaN/AlGaN superlattice which has similar QW and barrier thicknesses with sample G, and In composition of 17%.

We plot the temperature dependence of PL peak position and FWHM for sample G in Figure 5.7 and Figure 5.8, respectively. The dependence curves are not monotonic, which is also observed for other superlattices. This phenomenon is consistent with what was observed for InGaN thin films in Chapter 4. Therefore, the non-monotonic temperature dependence is

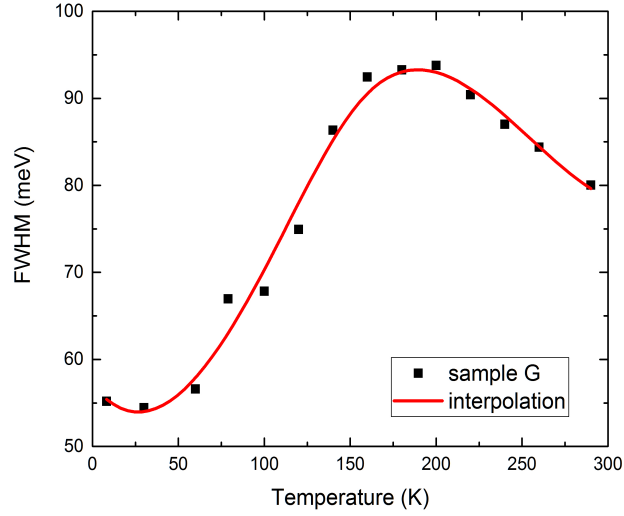


**Figure 5.8.** Temperature dependence curve of PL FWHM for sample G. The red interpolation line is a guide to the eye.

also likely due to the exciton localization in high-indium regions of QWs, and redistribution and relocation of excitons as temperature increases.

At low temperatures, the FWHM of sample G is just slightly larger than that of the InGaN thin films with comparable In composition (Samples A and B). QW interface roughness is likely the source of the excess broadening of the superlattice PL peak relative to the thin film PL peak. The low-temperature PL peak of sample G is found to be narrower than some reported low-temperature PL peaks for non-polar m-plane InGaN/(Al)GaN QWs. For example, a five-period m-plane InGaN/GaN superlattice grown by MOCVD was reported to have a PL peak at 3.038 eV with a FWHM of 121 meV at 10 K [34]. We find that our low-temperature PL results for non-polar m-plane InGaN/AlGaN superlattices grown by PAMBE are favorably comparable to previous published results for m-plane InGaN/(Al)GaN superlattices grown by MOCVD [34], [41], [49], [55].

#### 5.1.4 Defect band

In the PL spectra of many c-plane InGaN/GaN QWs or superlattices, a broad peak located around 490 nm (2.531 eV) is usually present [61]–[64]. This broad peak is believed to come from the defect band in QWs [61]. The origin of the defect band is not clear so far [62]. The presence of a defect band in c-plane InGaN/GaN QW is a big problem for designing and making some devices, since the defect band can significantly reduce the IQE of the device. There is research trying to find a method to suppress the defect band. A recent publication reports that doping above and below the active region can effectively suppress the defect band and attribute the improvement to the increase of band tilting from the doping [62]. It is claimed that the additional tilting of the band structure helps block

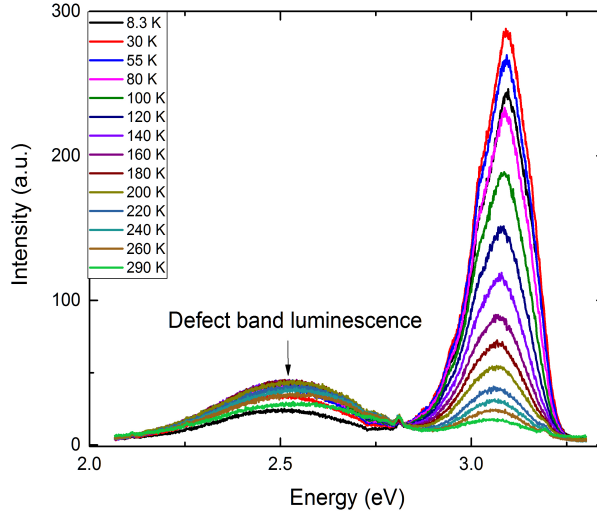


**Figure 5.9.** PL spectra at temperatures from 8.3K to 290K for sample K.

the recombination happening in the defect band. The band structure of undoped c-plane QW is not tilted enough to avoid the wave functions overlap with the defects that lead to decrease of IQE. The doping will enhance the band tilting, resulting in suppression of the defect band luminescence.

However, our PL results of non-polar m-plane superlattices show that the sufficient band tilting is not the cause for suppression of defect band luminescence. The effect of doping

on band tilting is negligible for m-plane samples. Our m-plane superlattices have symmetric band structures which are only slightly tilted no matter whether they are doped or not, but we do not observe PL signal from defect band at any temperature for all superlattices except sample K. Different from other superlattices, sample K has a doped GaN layer inserted below the GaN buffer layer (Figure 5.2(b)). We observed a defect band related peak in PL spectra of sample K, but the peak is very small (Figure 5.9). The ratio of this peak intensity relative to the main PL peak intensity is much smaller than reported results for c-plane QWs [61]–[64]. This little peak is likely due to the excess doping from the doped GaN layer. Therefore, the suppression of defect band luminescence in doped c-plane QWs is probably not related to the enhanced band tilting. Furthermore, the absence of defect band recombination is an important advantage of m-plane superlattices compared to c-plane ones.

## 5.2 Carrier localization and recombination

The carrier recombination lifetime is essential for design of III-nitride devices. A longer lifetime always allows for more non-radiative recombination, like Auger recombination, resulting in a lower IQE. High light output, large gain, and high injection currents can be achieved by a short recombination lifetime [65]. The carrier localization also plays an important role in III-nitride devices performance. A strong localization will prevent carriers from getting trapped by defect-related non-radiative recombination centers [52]. However, if the localization originates from the band fluctuation, the emission spectrum may be broadened. If localization potentials are too deep, the degree of polarization of the emitted light will be reduced [66]. A deep localization potential also contributes to accelerated device aging [65], [67].

Carrier localization and recombination lifetime are related. Whether the lifetime is long or short is affected by the character of localization sites. To date, extensive studies of recombination and localization for polar c-plane InGa<sub>N</sub>/(Al)Ga<sub>N</sub> QWs have been performed, while much fewer studies were published for non-polar m-plane QWs. Moreover, the non-polar m-plane structures reported in most studies were grown by MOCVD [34], [41], [49], [52], [55]–[60], [65], [66]. Therefore, in this section, we would like to discuss the PL investigation of

the carrier recombination and localization in our designed nearly strain-balanced non-polar m-plane InGaN/AlGaIn superlattices grown by PAMBE.

We will focus on doped and undoped superlattices, so we select sample G and sample H. Besides steady state PL, we performed TRPL on them in a temperature range from 2 K to 100 K. TRPL directly measures the decay of PL emission, which is very helpful for understanding of the carrier recombination processes [68], [69]. The excitation energy used in TRPL was selected to be the steady state PL peak energy.

### 5.2.1 Carrier localization depth

It is generally accepted that the localization process of excitons is necessary to produce PL signal [58]. The localization centers can be formed by many possible sources. Figure 5.1 indicates that there are no dot-like states in our superlattices. We have concluded that our superlattices are bi-axially strained from measurement of DLP, so localization centers do not originate from nanoscopic sites with relaxed strain. We found the incorporation of In leads to a large discrepancy between experimental results and calculation for InGaIn/AlGaIn superlattices, and the discrepancy indicates the inhomogeneous distribution of In composition. Due to absence of electric fields in non-polar m-plane band structures, electrons are likely to be bounded to holes to form localized excitons by Coulomb interaction [58]. This process can be enhanced by In composition fluctuation. Some previous reported studies of non-polar m-plane InGaIn/(Al)GaIn QWs also found that excitons localize in regions with high In composition [52], [70]. Therefore, we believe In rich regions act as localization centers in our nearly strain-balanced superlattices.

Localization is important for the FWHM of PL signal and its temperature dependence. Thus, we can investigate the localization of excitons from the temperature dependence of PL peak FWHM. The FWHM consists of homogeneous broadening and inhomogeneous broadening. The homogeneous broadening comes from the scattering of the excitons by acoustic phonons and the interaction of the excitons with the LO phonons. The scattering between excitons and acoustic phonons has a linear temperature dependence, and the interaction of

excitons with LO phonons is proportional to Bose–Einstein distribution [71]. Therefore, the total broadening has a temperature dependence as follows

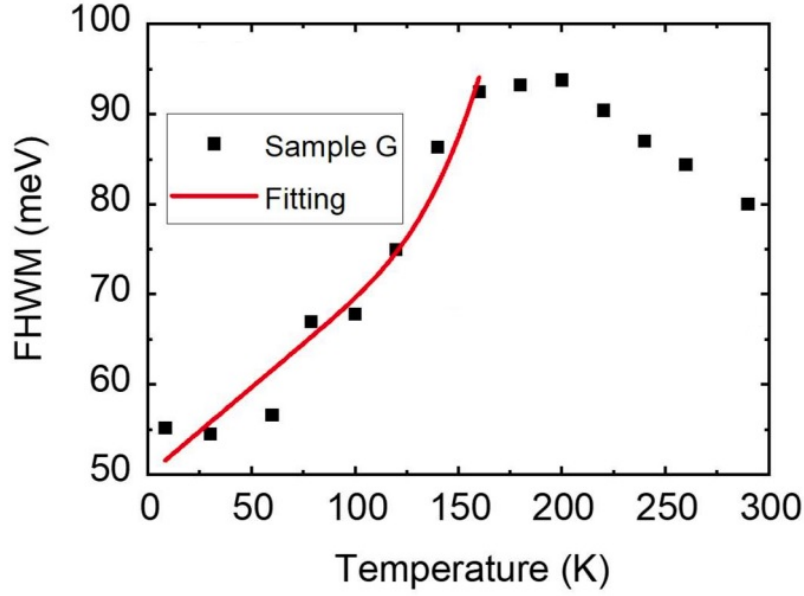
$$\Gamma(T) = \frac{\alpha}{e^{\frac{E_{LO}}{kT}} - 1} + \Gamma_{ih} + \beta T \quad (5.2)$$

where  $E_{LO}$  represents LO phonon energy, which is taken to be 90 meV [18].  $\Gamma_{ih}$  denotes the inhomogeneous broadening. We assume the In distribution is random and the depth of localization centers has a Gaussian distribution [72], [73]. Then the PL intensity under weak excitation is proportional to the following expression [73]

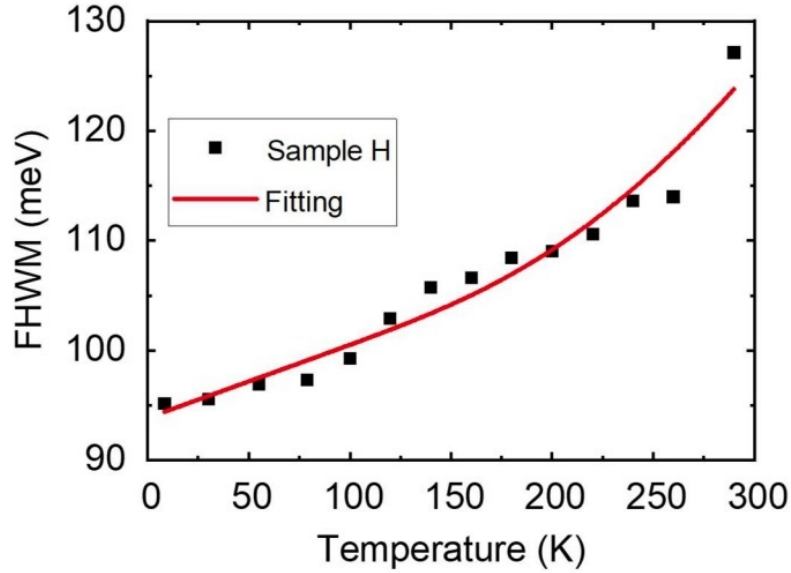
$$\int_{-\infty}^{\infty} \frac{1}{\sqrt{2\pi}\sigma} e^{-\frac{E}{kT}} g_0(E - E_1) e^{-\frac{E_1^2}{2\sigma^2}} dE_1 \quad (5.3)$$

where  $\sigma$  is the average localization potential depth.  $g_0(E)$  is the density of states for an ideal QW. This relation allows for the calculation of inhomogeneous broadening  $\Gamma_{ih}$ , and we can derive  $\Gamma_{ih} \approx 2.35\sigma$  for undoped QWs. We applied Eqn. (5.2) to fit the temperatures dependence curves of sample G and sample H (Figure 5.10(a) and Figure 5.10(b)).

The inhomogeneous broadenings are estimated to be  $51 \pm 3$  meV and  $94 \pm 2$  meV for sample G and sample H, respectively. The doped sample H has a much larger inhomogeneous broadening since the doping enhances impurity scattering, which contributes to inhomogeneous broadening as well. The related average localization potential depth is  $21 \pm 1$  meV for undoped sample G. This potential depth is smaller than reported values for m-plane InGaN/(Al)GaN QWs. For example, Liulio *et al.* reported an average localization depth of 46 meV for a non-polar m-plane 2.5 nm InGaN QW [73]. C-plane QWs may have a larger average localization potential depth and it can be as large as 80 meV [74]. The small localization potential depth of our samples is due to the fact that our undoped superlattice (sample G) has smaller low-temperature FWHM than previously reported values for m-plane InGaN/(Al)GaN QWs. The improvement of linewidth is likely due to the very different growth conditions used in our PAMBE as compared to previously reported growth conditions used in MOCVD. This shallow localization potential depth also agrees with the



(a) Temperature dependence of FWHM for samples G.



(b) Temperature dependence of FWHM for sample H.

**Figure 5.10.** Temperature dependence of FWHM for sample G (a) and sample H (b). Red lines are fitting curves based on the temperature dependence of total broadening (Eqn. (5.2)).

fact that PL signals of our superlattices are highly polarized (Figure 5.4), and the DLP calculated from polarized PL measurements is comparable to previous reported results.



Compared with undoped sample G, the doped sample H has a much larger inhomogeneous broadening. This is related to an average localization depth of  $40\pm 1$  meV. The Silicon doping inside barriers affects the alloy uniformity in QWs and barriers, and increases interface roughness, which results in enhancement of potential fluctuations experienced by excitons. Impurity scattering may also contribute to the inhomogeneous broadening in doped samples.

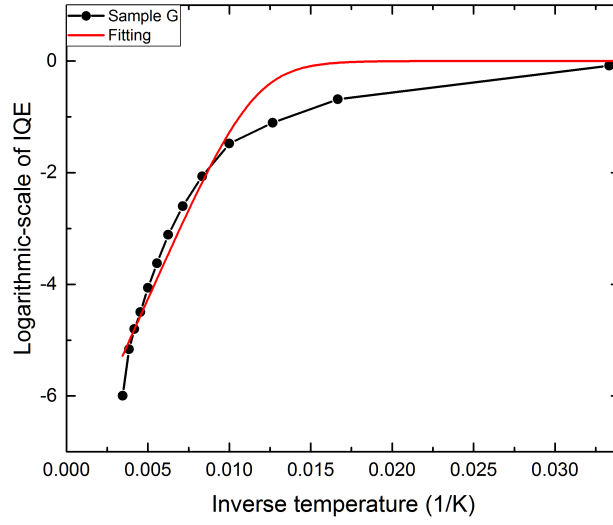
### 5.2.2 Thermal activation for non-radiative recombination

For localized luminescence centers, the related non-radiative recombination is multi-phonon recombination, which emits one or more phonons instead of photons when the exciton recombine. It originates in exciton-phonon coupling [2]. Therefore, at very low temperature, this non-radiative recombination can be neglected. However, as temperature increases, the thermal vibrations become significant. When the thermal energy gained by the exciton reaches a threshold, multi-phonon recombination takes place. This threshold is called activation energy. Once non-radiative recombination becomes dominant, we will see a large drop of IQE, as discussed in subsection 5.1.3. This phenomenon is called thermal quenching of PL. The relation between IQE and temperature is estimated as [2], [65], [75]

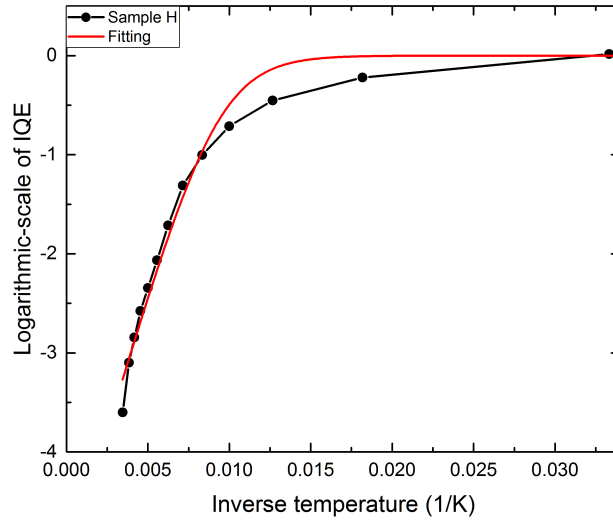
$$IQE = \frac{1}{1 + Ae^{-\frac{E_A}{k_B T}}} \quad (5.4)$$

where  $E_A$  is the activation energy.

We fitted the temperature dependence curves of IQE for sample G and H using the above relation (Figure 5.11). The obtained activation energies are 56.84 meV (sample G) and 48.36 meV (sample H). If we need thermal quenching to happen above room temperature, the activation energy is generally required to be larger than 100 meV. For example, ZnS has thermal quenching for temperatures larger than 310 K. The related activation energy is around 132 meV [2].



(a) Arrhenius plot of IQE for samples G.



(b) Arrhenius plot of IQE for sample H.

**Figure 5.11.** Arrhenius plot of IQE for sample G (a) and sample H (b). Red lines are fitting curves based on the relation of IQE and temperature (Eqn. (5.4)).

### 5.2.3 Discussion of TRPL spectra

TRPL of sample G is shown in Figure 5.12. The measurements were taken in the temperature range of 2 to 100 K. There are 2 decay times for sample G, which indicates 2 different localization centers (referred to as A and B). Dual localization centers have also been found in other non-polar m-plane InGaN/(Al)GaN QWs [73]. At 2 K, the fast decay time  $\tau_1$  is  $0.330 \pm 0.002$  ns, while the slow decay time  $\tau_2$  is  $2.18 \pm 0.06$  ns, approximately 7 times the fast decay time. In direct-bandgap semiconductors, the radiative recombination lifetime of free excitons has a magnitude of the order 1 ns [2]. So localization center B has weaker localization effect than A and the related recombination is more similar to recombination of free excitons. Figure 5.13 shows the TRPL of sample H. There is only one decay time for sample H, which indicates one localization center (referred to as C). At 2 K, the decay time  $\tau$  is  $0.283 \pm 0.002$  ns, slightly lower than  $\tau_1$ . These decay times are much shorter than those in polar c-plane structures, in agreement with the expectation that recombination is much faster in non-polar m-plane structures [65], [68], [76]. As temperature increases, bound excitons start to dissociate at around 100 K. The generated free excitons contribute to the increase of FWHM [52]. In sample G, free excitons will redistribute and relocalize between those 2 localization centers, resulting in a non-monotonic temperature dependence of FWHM above 150 K (Figure 5.10(a)).

Radiative recombination lifetime  $\tau_r$  and non-radiative recombination lifetime  $\tau_{nr}$  contribute to the total PL decay time  $\tau_{PL}$ . As introduced in Section 1.1 of Chapter 1, the relation among them is

$$\frac{1}{\tau_{PL}} = \frac{1}{\tau_r} + \frac{1}{\tau_{nr}} \quad (5.5)$$

The peak intensity of PL transients is approximately proportional to the radiative recombination rate [65], [77], [78]. At temperature lower than 5 K, major non-radiative recombination centers like Shockley-Read-Hall (SRH) recombination centers are hardly activated [68]. Therefore, the decay times we obtained at 2 K are a good approximation for radiative recombination lifetimes. As temperature increases, the decrease of PL intensity reflects the increase of radiative recombination lifetime (Figure 5.14). The decrease may be due to the increase of radiative recombination lifetime, but the total PL decay time decreases (Figure

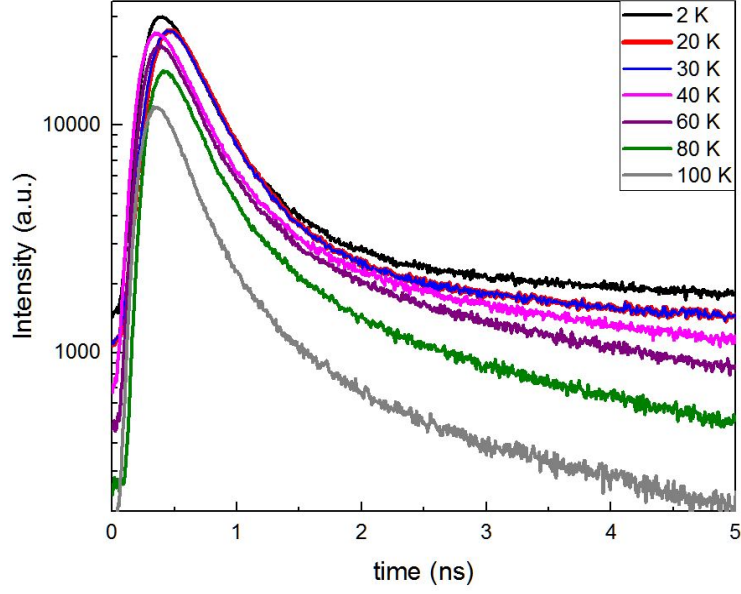


**Figure 5.12.** TRPL spectra for sample G.

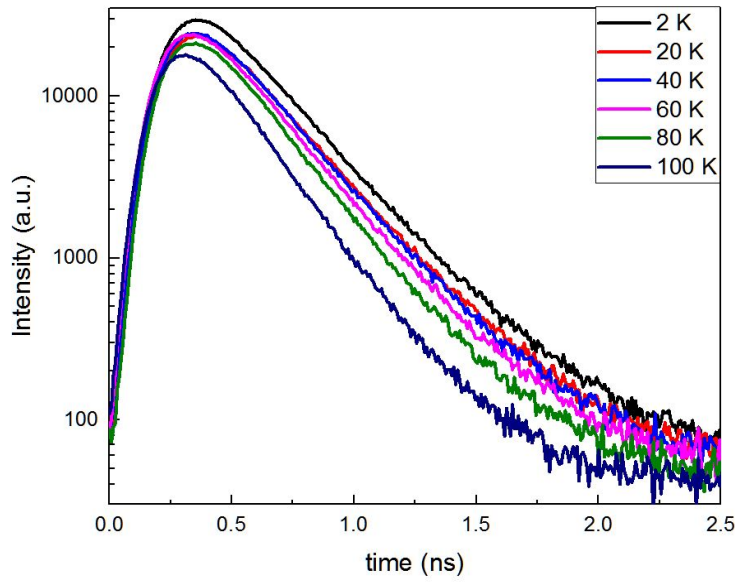


**Figure 5.13.** TRPL spectra for sample H.

5.15), which shows the non-radiative recombination lifetime decreases much more than the increase of radiative recombination lifetime. This indicates that localized excitons are thermally activated to the extended states and then get trapped by non-radiative recombination centers.

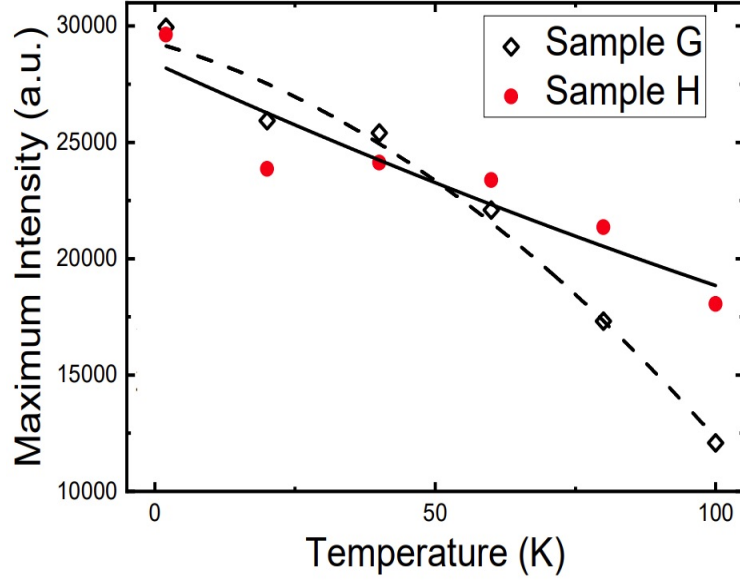


**Figure 5.14.** Temperature dependence of PL transient peak intensity for sample G and sample H. The lines are guides to the eye.

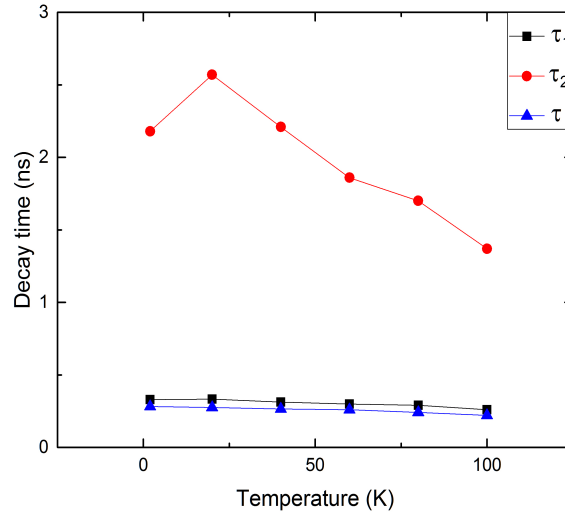


**Figure 5.15.** Temperature dependence of decay time  $\tau_1$  and  $\tau_2$  for sample G, and  $\tau$  sample H.

The density of the localization centers is obtained by fitting the temperature dependence of  $\tau_1$ . The model used in the fitting was proposed by Shahmohammadi *et al.* [79], [80]. In

this model, it is assumed that thermal equilibrium exists between free exciton and localized exciton populations based on Saha's law [81]. The decay time of excitons is written as

$$\tau_X = \frac{n_{loc} + n_{fr}}{\frac{n_{loc}}{\tau_{loc}} + \frac{n_{fr}}{\tau_{fr}}} \quad (5.6)$$

where  $\tau_{loc}$  is the time constant of localized excitons. It is set as the time constant measured at 2 K (0.33 ns).  $\tau_{fr}$  is the time constant of free excitons.  $n_{fr}$  and  $n_{loc}$  are the free exciton and localized exciton densities, respectively.

Based on 1.1,  $\tau_{fr}$  can be written as

$$\frac{1}{\tau_{fr}} = \frac{1}{\tau_r^{fr}} + \frac{1}{\tau_{nr}^{fr}} \quad (5.7)$$

where  $\tau_r^{fr}$  and  $\tau_{nr}^{fr}$  denote the radiative lifetime and non-radiative lifetime of free excitons, respectively. The radiative lifetime  $\tau_r^{fr}$  is assumed to have a linear relation with temperature T [79]:

$$\tau_r^{fr} = \frac{6Mk_B T}{\hbar^2 k_{\parallel}^2} \tau_0 \quad (5.8)$$

where  $k_{\parallel}$  is the in-plane wave vector of free excitons within the light cone and  $M$  is the effective mass of a free exciton.  $\frac{\hbar^2 k_{\parallel}^2}{2M}$  is approximately 0.1 meV [80].  $\tau_0$  is the radiative lifetime of free excitons at  $k_{\parallel} = 0$ . It is set as 10 ps [79], [80]. The non-radiative lifetime  $\tau_{nr}^{fr}$  is modeled as a thermally activated process. This relation with temperature T is given by

$$\tau_{nr}^{fr} = \tau_{nr,0} e^{-\frac{E_A}{k_B T}} \quad (5.9)$$

where  $E_A$  denotes the activation energy, which is about 200 meV.  $\tau_{nr,0}$  is the high temperature time constant, which is set as 100 ps.

The ratio between  $n_{fr}$  and  $n_{loc}$  is defined as

$$\frac{n_{fr}}{n_{loc}} = \frac{2M_X k_B T}{\pi \hbar^2 N_{loc}} e^{-\frac{E_{loc}}{k_B T}} \quad (5.10)$$

where  $M_X$  is the exciton mass, which is the sum of the mass of a hole and an electron. It is set as  $1.2m_0$ , where  $m_0$  is the rest mass of an electron [80].  $E_{loc}$  is the activation energy with which the radiative decay of localized excitons is thermally activated. It is assumed to be the average localization depth, which is estimated as 21 meV from our PL measurements.  $N_{loc}$  is the localization center density.

Finally, our experimental data is reproduced by a localization center density of about  $6 \times 10^{12} \text{ cm}^{-2}$ . This result is in agreement with previous reports [79].

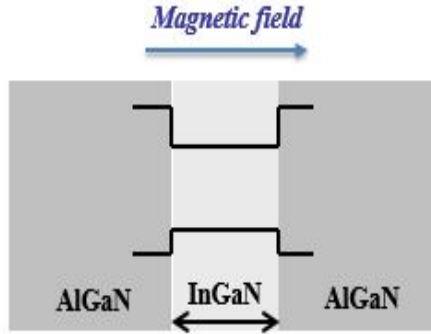


**Figure 5.16.** The direction of magnetic field applied to the superlattices.

At 2 K, we also measured the effect of magnetic field on TRPL of both sample G and sample H and then measured TRPL in order to estimate the localization of excitons at this low temperature. The field is applied along the growth direction (Figure 5.16). After optical excitation, a 2D electron gas exists in QWs. Due to Lorentz force, the in-plane movement of electrons will be restricted and thus localization of excitons will be increased [37]. On the other hand, the in-plane kinetic energy of electrons has a discrete energy spectrum under magnetic field. Therefore, resonant luminescence of free excitons will be reduced. At 10 T, the degree of degeneracy can be as large as  $1.21 \times 10^{15} \text{ m}^{-2}$ , which is much larger than the density of electrons from excitation. The lifetime to get trapped by localization center is comparable to the lifetime of free exciton recombination. So the reduced luminescence of free exciton increases the probability for electrons to get trapped by localization centers, resulting in enhancement of localization of carriers.

The TRPL in magnetic field for sample G and sample H is shown in Figure 5.17 and Figure 5.18, respectively. The magnetic field varies in the range of 0 T-10 T. The trend of

magnetic field dependence of PL transient peak intensity is opposite for sample G and sample H. Sample G has an increase of PL peak intensity, indicating an increase of radiative recombination rate. We attribute this increase to an increased overlap of the electron and hole wave functions. Sample H has a decrease of PL peak intensity, which indicates an increase of non-radiative recombination rate. The increased localization in doped sample H probably leads to an enhancement of non-radiative recombination associated with the additional doping, which may be due to additional structural defects and/or Auger recombination.

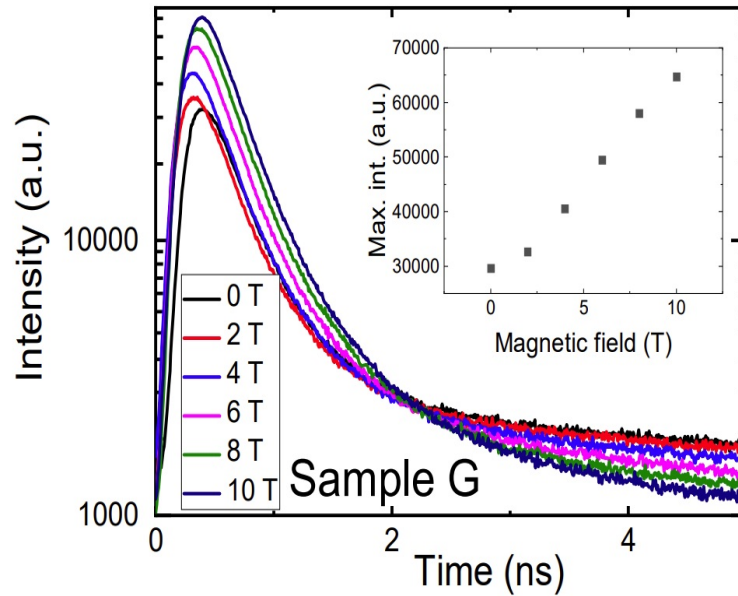


**Figure 5.17.** TRPL spectra in magnetic field for sample G. The inset is the magnetic field dependence of PL transient peak intensity.

As the magnetic field increases,  $\tau_1$  and  $\tau$  decrease slightly, while  $\tau_2$  decreases significantly (Figure 5.19). Over the field range from 0 T-10 T,  $\tau_1$  and  $\tau$  decrease about 2%, while  $\tau_2$  decreases about 26%. Therefore, the localization of excitons in localization center A and C is not affected by the magnetic field. For localization center B, not all excitons are localized in the ground state but may also be in the extended state. Thus, the increased magnetic field improves the localization effect, and  $\tau_2$  decreases as a result of decrease of radiative recombination lifetime.

Sample G and sample H have similar structures. The simulation suggests that their PL peaks are close to each other, and we did observe similar PL peak energies for both



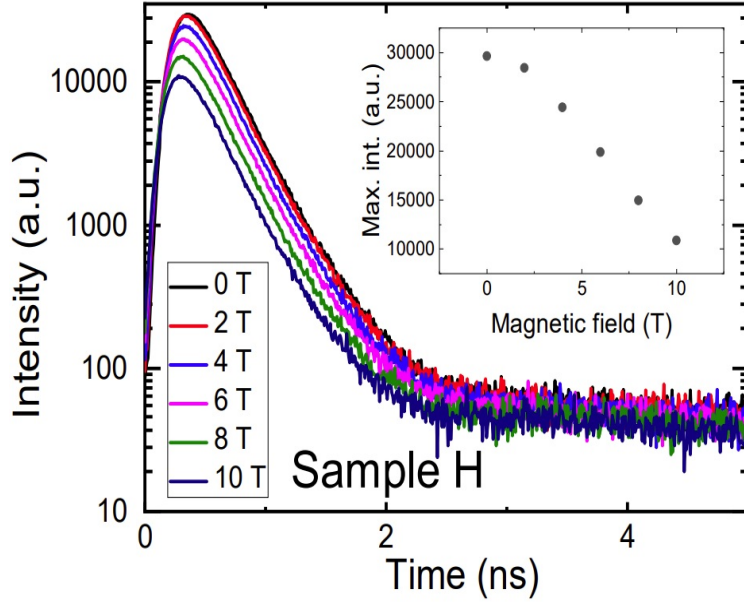


**Figure 5.18.** TRPL spectra in magnetic field for sample H. The inset is the magnetic field dependence of PL transient peak intensity.

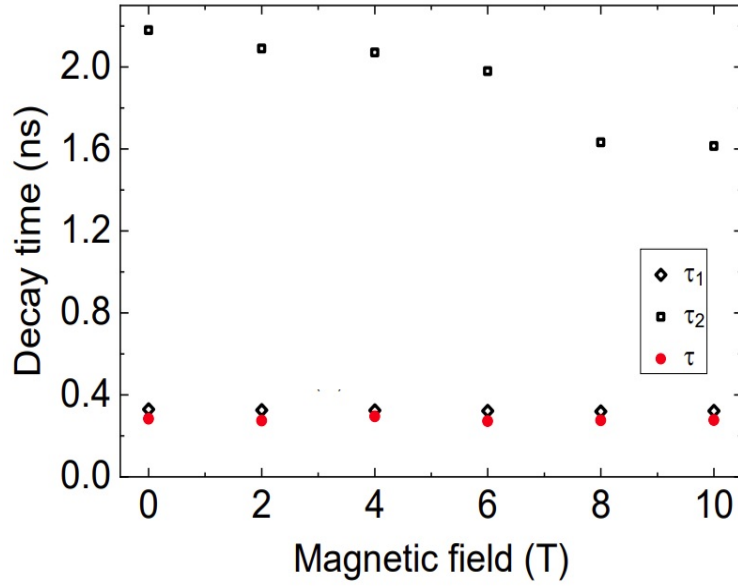


**Figure 5.19.** Magnetic field dependence of decay time  $\tau_1$  and  $\tau_2$  for sample G, and  $\tau$  sample H.

of them. The agreement of measured PL energies confirms that they have the intended identical layer structures. The decay times,  $\tau_1$  and  $\tau$ , of localization centers A and C are close to each other, and they have similar temperature and magnetic field dependence curves.

In contrast, the decay time  $\tau_2$  of localization center B is much larger. Every decay time decreases as temperature increases (Figure 5.15). However, the change of  $\tau_1$  and  $\tau$  is less dramatic than  $\tau_2$ . Over the temperature range from 2 K-100 K, both  $\tau_1$  and  $\tau$  decrease about 22%, while  $\tau_2$  decreases about 38%. Therefore, A and C are likely the same type of localization centers inside the InGaN QWs, and this type of localization center is dependent on the layer structure. We believe that they originate from In-rich regions.

The localization center B has a different origin than localization center A and C. If localized excitons are formed by electrons and holes at different sites, the decay time can be tens to hundreds of nanoseconds [52]. In some wide m-plane InGaN QWs, the decay time was reported to be several or tens of nanoseconds [65]. The tight binding model [41] has shown that the electron can be spread over the entire QW, and the diameter of the spreading region may be as large as 5 nm, which is larger than our QW size. Therefore, the localization center B is likely due to alloy fluctuations in barriers that localize electrons and holes at different in-plane sites. As temperature increases, the related decay time  $\tau_2$  has a faster decrease than the other two decay times due to non-radiative recombination in the barriers.

In doped sample H, the doping sheets act as blocking layers. These layers further confine the electron and hole wavefunctions, and prevent carriers inside QWs from getting trapped by the recombination sites in barriers. Thus, for sample H we did not observe a second decay time, which is characterized by the decay time  $\tau_2$  of localization center B in undoped sample G. Also, due to the blocking layers, the PL transient peak intensity of sample H decreases slower than that of sample G (Figure 5.14), because fewer carriers get trapped by non-radiative recombination centers by thermal activation.

### 5.3 Summary

PL investigation was performed on nearly strain-balanced non-polar m-plane InGaN/Al-GaN superlattices. This is the first time when their PL is reported. Like InGaN thin films, the measured PL peak energies are systematically smaller than calculated peak energies. The discrepancy is much larger for superlattices than thin films. We attribute this to the

In composition fluctuation inside QWs. On the other hand, the overestimation of strain is a possible alternative explanation. Unlike many other polar c-plane QWs, PL signal from defect band was not observed in our non-polar m-plane superlattices.

The broadening mechanism of InGaN/AlGaN superlattices is not affected by the incorporation of In. It is likely determined by the structures and doping profiles. As density of dopant increases, the FWHM increases due to the increased scattering from impurities. The low-temperature FWHM of our undoped superlattice is comparable with previously reported values for non-polar InGaN/(Al)GaN QWs grown by MOCVD.

The regions with high In composition act as localization centers for excitons. The delocalization, redistribution, and relocation of excitons when temperature increases lead to non-monotonic temperature dependence curves of PL peak position and FWHM. An average localization potential depth of  $21 \pm 1$  meV was revealed. This depth is much smaller than that in polar structures or some previously reported non-polar InGaN/(Al)GaN QWs grown by MOCVD. The small localization potential depth contributes to narrow spectral width, and the degree of polarization is not reduced. At 2 K, the fast decay time is about 0.3 ns, which is much shorter than that of polar c-plane structures or wide m-plane QWs. There are dual localization centers in undoped superlattices, while only single localization center exists in doped superlattices. The density of localization centers in undoped samples is estimated as  $6 \times 10^{12} \text{ cm}^{-2}$ . The change of decay pathway in doped samples is attributed to the doping sheets acting as blocking layers. Time-resolved photoluminescence in magnetic field indicates that magnetic field does not significantly affect the localization of carriers at low temperatures in centers A and C. In contrast, increasing magnetic field results in a decrease of the decay time of excitons localized by barrier fluctuations in centers C.

## 6. OUTLOOK OF FUTURE WORK

### 6.1 Improvement of the growth for non-polar m-plane In containing heterostructures

#### 6.1.1 Thick GaN buffer layer and InGaN underlayer

At room temperature, PL intensities are very weak for all non-polar m-plane InGaN thin films and InGaN/AlGaN superlattices. This indicates there are plenty of non-radiative recombination centers in our samples at room temperature. They trap more and more excitons when temperature goes up, which causes non-radiative recombination to become the dominant recombination process at room temperature. Since many devices operate at room temperature, a large number of non-radiative recombination centers is harmful for devices based on either interband or intersubband transition. Therefore, we are looking for methods to reduce density of non-radiative recombination centers and increase PL intensity at room temperature for In containing heterostructures.

At first, we proposed increasing the thickness of the buffer layer. The diffusion length of excitons for non-polar m-plane InGaN/GaN QWs is reported to be 200-500 nm [66]. It is much larger than the active region of our superlattices or the thickness of InGaN thin films, which makes it possible for a large number of excitons to diffuse over GaN buffer layer and get trapped by non-radiative recombination centers in the substrate at room temperature. So we grew a sample M with a 1 micron GaN buffer layer. Sample M has the same structure and doping profile as sample J. Figure 6.1 shows the PL spectra from 8.3 K to 290 K for sample M.

The intensity of PL signal at room temperature increases. However, the peak is not very obvious. The thick GaN buffer may sufficiently block the diffusion of excitons to the substrate, so PL signal is stronger. However, PL signal from defect band also shows up, then it becomes hard to extract the PL peak in the spectrum. Thus, the use of thick GaN buffer layer is not sufficient.

A recent report showed that defects in the GaN buffer layer cause the drop of PL signal at room temperature for c-plane InGaN/GaN superlattices [82]. They suggest to grow an InGaN underlayer to improve the homogeneity. PL signal of single c-plane  $\text{In}_{0.12}\text{Ga}_{0.88}\text{N}/\text{GaN}$

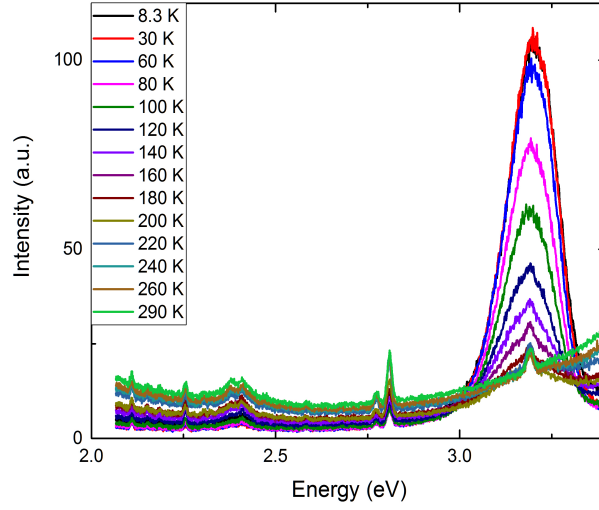


**Figure 6.1.** PL spectra at temperatures from 8.3 K to 290 K for sample M.

quantum well at room temperature was observed after the underlayer was inserted [82]. Thus, we proposed this method of InGaN underlayer insertion for our samples, especially non-polar m-plane InGaN/AlGaN superlattices.

We grew sample L with an  $\text{In}_{0.07}\text{Ga}_{0.93}\text{N}$  underlayer. The thickness of this underlayer is about 30 nm. Figure 6.2 provides the structure of sample L. It has the same QW structure and doping profile as sample J. The steady state PL measurement was taken from 8.3 K to

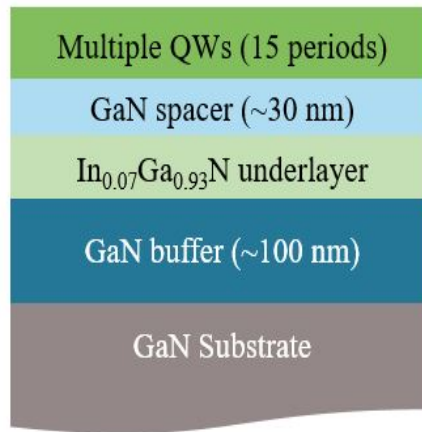


**Figure 6.2.** Sketch of structure for sample L.

290 K (Figure 6.3). At low temperatures, there are 2 peaks around 3.1 eV. The right one

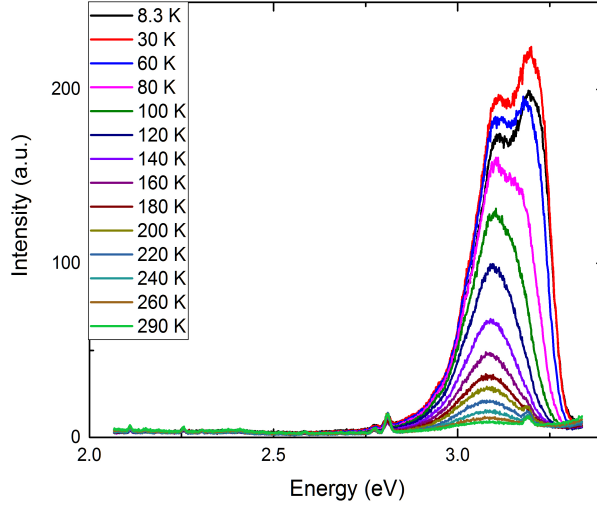


**Figure 6.3.** PL spectra at temperatures from 8.3 K to 290 K for sample L.

is from the InGaN underlayer and the left one is from the QWs. Since the In compositions of the underlayer (7%) and the QWs (9%) are close to each other, the 2 peaks have close energies and they overlap. They merge together as temperature goes up. The PL signal from the defect band was not observed in this case.

Unfortunately, we still observe a large drop of PL intensity as temperature increases. The IQE drops more than 96% when temperature reaches room temperature. This result indicates that non-radiative recombination is not sufficiently blocked at room temperature. This is likely due to the difference of band structure between non-polar m-plane and polar c-plane heterostructures. The band tilting of c-plane structure has already enhanced the localization of excitons. The insertion of InGaN underlayer assists this localization effect and the diffusion of excitons are sufficiently blocked. However, the symmetric band structure of m-plane heterostructures will not help localization of excitons and then the insertion of InGaN underlayer does not improve PL at room temperature.

### 6.1.2 Growth conditions for AlGa<sub>N</sub> barrier

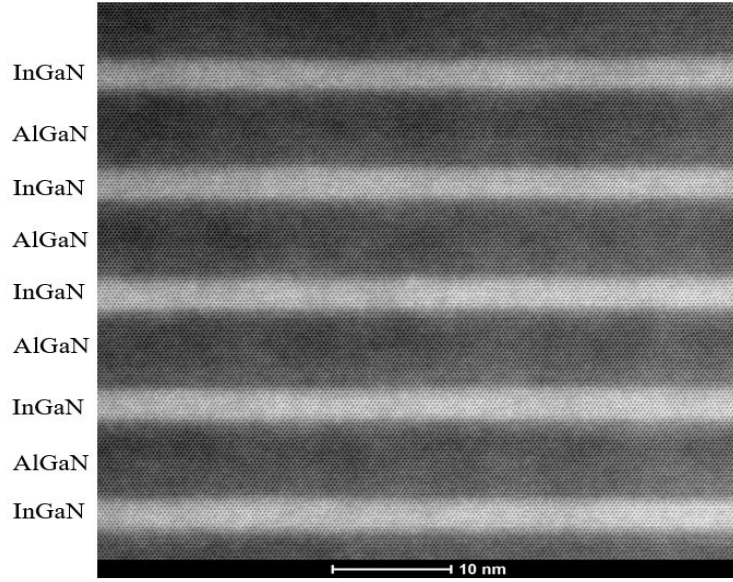
Our current growth conditions for non-polar m-plane superlattices introduce an unintentional GaN layer at the interface of QW and barrier. Both simulation and experiment show that this layer hardly affects the interband transition in QWs. However, it may affect intersubband transitions. The presence of this GaN layer reduces the energies of confined states in QWs. We hope our nearly strain-balanced superlattices can be used for devices based on either interband transition or intersubband transition. Therefore, we try to improve our growth conditions to get rid of this unintentional GaN layer.

The current growth for AlGa<sub>N</sub> barriers is done under Gallium-rich conditions. The application of excess Ga is typical to optimally grow AlGa<sub>N</sub> barrier at high temperature. This growth condition helps reduce inhomogeneity and produces a sharper interface of QW and barrier. However, this excess Ga cannot be thermally desorbed from surface at low temperature, which results in the formation of the unintentional GaN layer [29]. Some previous reports show that growth of AlGa<sub>N</sub> with In surfactant will lead to reduced inhomogeneity [83] and density of defects [84]. This kind of growth also promotes two-dimensional growth [85]. Therefore, we would like to apply this growth method for AlGa<sub>N</sub> barriers of our superlattices.

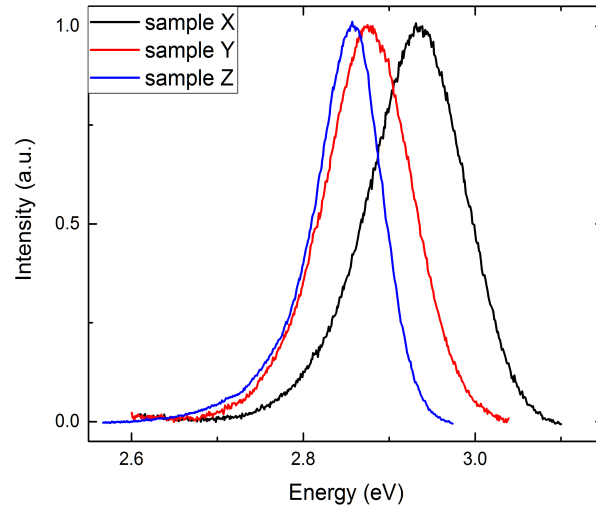
We grew 3 nearly strain-balanced InGa<sub>N</sub>/AlGa<sub>N</sub> superlattices with different growth conditions for the AlGa<sub>N</sub> barrier: stoichiometric (sample X), Gallium-rich (sample Y), and Indium surfactant (sample Z). All samples have 15 periods of QWs. From HRXRD, the In composition is 15.5% and the Al composition is 22%. The QW thickness is around 2.8 nm, and the barrier thickness is about 7 nm. A 10 s delta-doping was applied to all samples.

Figure 6.4 provides the HAADF-STEM image of sample Z grown with Indium surfactant. By careful examination of this image, we do not find any unintentional GaN layer. The material in QWs and barriers looks uniform. The interface between QW and barrier is sharp and well-defined.

We took steady state PL measurements for these 3 superlattices. The PL spectra at 80 K are shown in Figure 6.5. The PL peak positions are different among these 3 samples, although their In compositions obtained from HRXRD are the same. The peak position of



**Figure 6.4.** HAADF-STEM image of sample Z. The darker layers are AlGaN, while the lighter layers are InGaN.



**Figure 6.5.** PL spectra of samples X-Z at 80 K. The PL curves of samples X-Z were reduced by a factor of 250.63, 378.07, and 612.73, respectively.

sample X is away from that of sample Y and sample Z. This indicates that there is larger In composition fluctuation in samples Y and Z than sample X, even though Ga-rich and In surfactant growth conditions are optimized compared with stoichiometric growth condition.



The FWHMs of samples X-Z are 138 meV, 126 meV, and 91 meV, respectively. The In surfactant sample Z has an at least 30% narrower PL peak at 80 K, indicating that the material is more homogeneous and non-radiative recombination centers are fewer. Moreover, the PL peak intensity of sample Z is at least twice as that of samples X and Y.

In conclusion, growth of AlGaIn barrier with In surfactant successfully eliminates the formation of unintentional GaN layer identified in superlattices grown with Ga-rich conditions. PL peak intensity is improved and the peak becomes sharper. These improvements are likely due to the enhanced adatom mobility at the growth front underneath the In adlayer [29].

## 6.2 Summary

Effort was taken to improve PL intensity at room temperature. The insertion of InGaIn underlayer does not function well for non-polar m-plane superlattices, even though it works for polar c-plane QWs. A thick GaN buffer layer helps increase PL intensity at room temperature, but it introduces many other luminescence centers, which makes it hard to extract PL signal from QWs at room temperature.

The growth of AlGaIn barrier needs to be optimized further. The In surfactant condition avoids the formation of unintentional GaN layer. A superlattice grown under this condition has higher PL intensity and sharper PL peak.

With the knowledge obtained from PL investigation for the material quality and optical properties of the nearly strain-balanced structures, we expect this type of structure will contribute to provide solutions for many challenging problems in design of opto-electronic devices based on intersubband transition or interband transitions.

## REFERENCES

- [1] K. N. Shinde, S. Dhoble, H. Swart, and K. Park, *Phosphate Phosphors for Solid-State Lighting*. Berlin Heidelberg: Springer-Verlag, 2013.
- [2] I. Pelant and J. Valenta, *Luminescence Spectroscopy of semiconductors*. New York: Oxford University Press, 2016.
- [3] G. Bourdon, I. Robert, I. Sagnes, and I. Abram, “Spontaneous emission in highly excited semiconductors: Saturation of the radiative recombination rate,” *JOURNAL OF APPLIED PHYSICS*, vol. 92, no. 11, 2002.
- [4] H. Bebb and E. Williams, *Photoluminescence I. Theory, In Semiconductors and Semimetals*. New York: Academic Press, 1972.
- [5] C. Kittel, *Introduction to Solid State Physics*. New York: John Wiley, 1979.
- [6] A. Mooradian and H. Y. Fan, “Recombination emission in insb,” *Phys. Rev.*, vol. 148, pp. 873–885, 2 Aug. 1966. DOI: [10.1103/PhysRev.148.873](https://doi.org/10.1103/PhysRev.148.873). [Online]. Available: <https://link.aps.org/doi/10.1103/PhysRev.148.873>.
- [7] D. G. Thomas, M. Gershenson, and F. A. Trumbore, “Pair spectra and ”edge” emission in gallium phosphide,” *Phys. Rev.*, vol. 133, A269–A279, 1A Jan. 1964. DOI: [10.1103/PhysRev.133.A269](https://doi.org/10.1103/PhysRev.133.A269). [Online]. Available: <https://link.aps.org/doi/10.1103/PhysRev.133.A269>.
- [8] C. Weisbuch and H. Benisty, “Microcavities in ecole polytechnique fédérale de lausanne, ecole polytechnique (france) and elsewhere: Past, present and future,” *physica status solidi (b)*, vol. 242, no. 11, pp. 2345–2356, Sep. 2005, ISSN: 1521-3951. DOI: [10.1002/pssb.200560972](https://doi.org/10.1002/pssb.200560972). [Online]. Available: <https://doi.org/10.1002/pssb.200560972>.
- [9] E. S. Koteles, J. Lee, J. P. Salerno, and M. O. Vassell, “Elastic scattering of exciton polaritons by neutral impurities,” *Phys. Rev. Lett.*, vol. 55, pp. 867–870, 8 Aug. 1985. DOI: [10.1103/PhysRevLett.55.867](https://doi.org/10.1103/PhysRevLett.55.867). [Online]. Available: <https://link.aps.org/doi/10.1103/PhysRevLett.55.867>.
- [10] E. Rashba and G. Gurgenishvili, “Edge absorption theory in semiconductors,” *Sov.Phys.-Solid State*, vol. 4, p. 759, 1962.
- [11] M. Voos, R. Leheny, and J. Shah, *Radiative recombination. In: Handbook on Semiconductors*. North Holland: Amsterdam, 1980.
- [12] E. F. Schubert, *Light-Emitting Diodes*, 2nd ed. Cambridge University Press, 2006. DOI: [10.1017/CBO9780511790546](https://doi.org/10.1017/CBO9780511790546).

- [13] C. Zhou, A. Ghods, V. G. Saravade, P. V. Patel, K. L. Yunghans, C. Ferguson, Y. Feng, B. Kucukgok, N. Lu, and I. T. Ferguson, "Review—the current and emerging applications of the III-nitrides," *ECS Journal of Solid State Science and Technology*, vol. 6, no. 12, Q149–Q156, 2017. DOI: [10.1149/2.0101712jss](https://doi.org/10.1149/2.0101712jss).
- [14] H. Morkoç, S. Strite, G. B. Gao, M. E. Lin, B. Sverdlov, and M. Burns, "Large-band-gap sic, III-V nitride, and II-V znse-based semiconductor device technologies," *Journal of Applied Physics*, vol. 76, no. 3, pp. 1363–1398, 1994. DOI: [10.1063/1.358463](https://doi.org/10.1063/1.358463). [Online]. Available: <https://doi.org/10.1063/1.358463>.
- [15] N. Ikeda, Y. Niiyama, H. Kambayashi, Y. Sato, T. Nomura, S. Kato, and S. Yoshida, "GaN power transistors on Si substrates for switching applications," *Proceedings of the IEEE*, vol. 98, no. 7, pp. 1151–1161, Jul. 2010, ISSN: 0018-9219. DOI: [10.1109/JPROC.2009.2034397](https://doi.org/10.1109/JPROC.2009.2034397).
- [16] H. Ishida, R. Kajitani, Y. Kinoshita, H. Umeda, S. Ujita, M. Ogawa, K. Tanaka, T. Morita, S. Tamura, M. Ishida, and T. Ueda, "GaN-based semiconductor devices for future power switching systems," in *2016 IEEE International Electron Devices Meeting (IEDM)*, Dec. 2016, pp. 20.4.1–20.4.4. DOI: [10.1109/IEDM.2016.7838460](https://doi.org/10.1109/IEDM.2016.7838460).
- [17] Z. Liu, J. Ma, X. Yi, E. Guo, L. Wang, J. Wang, N. Lu, J. Li, I. Ferguson, and A. Melton, "P-InGaN/AlGaIn electron blocking layer for InGaIn/GaN blue light-emitting diodes," *Applied Physics Letters*, vol. 101, no. 26, p. 261 106, 2012. DOI: [10.1063/1.4773187](https://doi.org/10.1063/1.4773187). [Online]. Available: <https://doi.org/10.1063/1.4773187>.
- [18] M. Beeler, E. Trichas, and E. Monroy, "III-nitride semiconductors for intersubband optoelectronics: A review," *Semiconductor Science and Technology*, vol. 28, no. 7, p. 074 022, Jun. 2013. DOI: [10.1088/0268-1242/28/7/074022](https://doi.org/10.1088/0268-1242/28/7/074022).
- [19] A. Helman, M. Tchernycheva, A. Lusson, E. Warde, F. H. Julien, K. Moumanis, G. Fishman, E. Monroy, B. Daudin, D. Le Si Dang, E. Bellet-Amalric, and D. Jalabert, "Intersubband spectroscopy of doped and undoped GaN/AlN quantum wells grown by molecular-beam epitaxy," *Applied Physics Letters*, vol. 83, no. 25, pp. 5196–5198, 2003. DOI: [10.1063/1.1635985](https://doi.org/10.1063/1.1635985). [Online]. Available: <https://doi.org/10.1063/1.1635985>.
- [20] T. Kotani, M. Arita, and Y. Arakawa, "Observation of mid-infrared intersubband absorption in non-polar m-plane AlGaIn/GaN multiple quantum wells," *Applied Physics Letters*, vol. 105, no. 26, p. 261 108, 2014. DOI: [10.1063/1.4905212](https://doi.org/10.1063/1.4905212). [Online]. Available: <https://doi.org/10.1063/1.4905212>.
- [21] C. Edmunds, J. Shao, M. Shirazi-HD, M. J. Manfra, and O. Malis, "Terahertz intersubband absorption in non-polar m-plane AlGaIn/GaN quantum wells," *Applied Physics Letters*, vol. 105, no. 2, p. 021 109, 2014. DOI: [10.1063/1.4890611](https://doi.org/10.1063/1.4890611). [Online]. Available: <https://doi.org/10.1063/1.4890611>.

- [22] M. Shirazi-HD, R. E. Diaz, T. Nguyen, J. Jian, G. C. Gardner, H. Wang, M. J. Manfra, and O. Malis, “Kinetic instability of AlGa<sub>N</sub> alloys during mbe growth under metal-rich conditions on m-plane GaN miscut towards the -c axis,” *Journal of Applied Physics*, vol. 123, no. 16, p. 161 581, 2018. DOI: [10.1063/1.5011413](https://doi.org/10.1063/1.5011413). [Online]. Available: <https://doi.org/10.1063/1.5011413>.
- [23] D. Li, L. Tang, C. Edmunds, J. Shao, G. Gardner, M. J. Manfra, and O. Malis, “Repeatable low-temperature negative-differential resistance from Al<sub>0.18</sub>Ga<sub>0.82</sub>N/GaN resonant tunneling diodes grown by molecular-beam epitaxy on free-standing GaN substrates,” *Applied Physics Letters*, vol. 100, no. 25, p. 252 105, 2012. DOI: [10.1063/1.4729819](https://doi.org/10.1063/1.4729819). [Online]. Available: <https://doi.org/10.1063/1.4729819>.
- [24] H. Machhadani, Y. Kotsar, S. Sakr, M. Tchernycheva, R. Colombelli, J. Mangeney, E. Bellet-Amalric, E. Sarigiannidou, E. Monroy, and F. H. Julien, “Terahertz inter-subband absorption in GaN/AlGa<sub>N</sub> step quantum wells,” *Applied Physics Letters*, vol. 97, no. 19, p. 191 101, 2010. DOI: [10.1063/1.3515423](https://doi.org/10.1063/1.3515423). [Online]. Available: <https://doi.org/10.1063/1.3515423>.
- [25] C. Edmunds, L. Tang, M. Cervantes, M. Shirazi-HD, J. Shao, A. Grier, A. Valavanis, J. D. Cooper, D. Li, G. Gardner, D. N. Zakharov, Z. Ikonić, D. Indjin, P. Harrison, M. J. Manfra, and O. Malis, “Comparative study of intersubband absorption in AlGa<sub>N</sub>/GaN and AlIn<sub>N</sub>/GaN superlattices: Impact of material inhomogeneities,” *Phys. Rev. B*, vol. 88, p. 235 306, 23 Dec. 2013. DOI: [10.1103/PhysRevB.88.235306](https://doi.org/10.1103/PhysRevB.88.235306). [Online]. Available: <https://link.aps.org/doi/10.1103/PhysRevB.88.235306>.
- [26] T. Paskova, D. A. Hanser, and K. R. Evans, “GaN substrates for III-nitride devices,” *Proceedings of the IEEE*, vol. 98, no. 7, pp. 1324–1338, Jul. 2010, ISSN: 0018-9219. DOI: [10.1109/JPROC.2009.2030699](https://doi.org/10.1109/JPROC.2009.2030699).
- [27] T. D. Moustakas and R. Paiella, “Optoelectronic device physics and technology of nitride semiconductors from the UV to the terahertz,” *Reports on Progress in Physics*, vol. 80, no. 10, p. 106 501, Sep. 2017. DOI: [10.1088/1361-6633/aa7bb2](https://doi.org/10.1088/1361-6633/aa7bb2).
- [28] T. Nguyen, M. Shirazi-Hosseini-Dokht, Y. Cao, R. E. Diaz, G. C. Gardner, M. J. Manfra, and O. Malis, “Intersubband transitions in nonpolar m-plane AlGa<sub>N</sub>/GaN heterostructures,” *physica status solidi (a)*, vol. 215, no. 13, p. 1 700 828, 2018. DOI: [10.1002/pssa.201700828](https://doi.org/10.1002/pssa.201700828). [Online]. Available: <https://onlinelibrary.wiley.com/doi/abs/10.1002/pssa.201700828>.
- [29] B. Dzuba, A. Senichev, T. Nguyen, Y. Cao, R. E. Diaz, M. J. Manfra, and O. Malis, “Indium surfactant assisted epitaxy of non-polar (1010) AlGa<sub>N</sub>/InGa<sub>N</sub> multiple quantum well heterostructures,” *Journal of Applied Physics*, vol. 128, no. 11, p. 115 701, 2020. DOI: [10.1063/5.0020263](https://doi.org/10.1063/5.0020263). [Online]. Available: <https://doi.org/10.1063/5.0020263>.

- [30] A. Senichev, B. Dzuba, T. Nguyen, Y. Cao, M. A. Capano, M. J. Manfra, and O. Malis, “Impact of growth conditions and strain on indium incorporation in non-polar m-plane (10 $\bar{1}0$ ) InGa $\bar{N}$  grown by plasma-assisted molecular beam epitaxy,” *APL Materials*, vol. 7, no. 12, p. 121 109, 2019. DOI: [10.1063/1.5121445](https://doi.org/10.1063/1.5121445). [Online]. Available: <https://doi.org/10.1063/1.5121445>.
- [31] Y. Cao, B. Dzuba, B. A. Magill, A. Senichev, T. Nguyen, R. E. Diaz, M. J. Manfra, S. McGill, C. Garcia, G. A. Khodaparast, and O. Malis, “Photoluminescence study of non-polar m-plane InGa $\bar{N}$  and nearly strain-balanced InGa $\bar{N}$ /AlGa $\bar{N}$  superlattices,” *Journal of Applied Physics*, vol. 127, no. 18, p. 185 702, 2020. DOI: [10.1063/5.0003740](https://doi.org/10.1063/5.0003740). [Online]. Available: <https://doi.org/10.1063/5.0003740>.
- [32] M. Funato and Y. Kawakami, “Excitonic properties of polar, semipolar, and nonpolar InGa $\bar{N}$ /Ga $\bar{N}$  strained quantum wells with potential fluctuations,” *Journal of Applied Physics*, vol. 103, no. 9, p. 093 501, 2008. DOI: [10.1063/1.2903592](https://doi.org/10.1063/1.2903592). [Online]. Available: <https://doi.org/10.1063/1.2903592>.
- [33] A. Kaneta, M. Funato, and Y. Kawakami, “Nanoscopic recombination processes in InGa $\bar{N}$ /Ga $\bar{N}$  quantum wells emitting violet, blue, and green spectra,” *Phys. Rev. B*, vol. 78, p. 125 317, 12 Sep. 2008. DOI: [10.1103/PhysRevB.78.125317](https://link.aps.org/doi/10.1103/PhysRevB.78.125317). [Online]. Available: <https://link.aps.org/doi/10.1103/PhysRevB.78.125317>.
- [34] D. Kundys, D. Sutherland, M. J. Davies, F. Oehler, J. Griffiths, P. Dawson, M. J. Kappers, C. J. Humphreys, S. Schulz, F. Tang, and R. A. Oliver, “A study of the optical and polarisation properties of InGa $\bar{N}$ /Ga $\bar{N}$  multiple quantum wells grown on a-plane and m-plane Ga $\bar{N}$  substrates,” *Science and Technology of Advanced Materials*, vol. 17, no. 1, pp. 736–743, 2016, PMID: 27933113. DOI: [10.1080/14686996.2016.1244474](https://doi.org/10.1080/14686996.2016.1244474). [Online]. Available: <https://doi.org/10.1080/14686996.2016.1244474>.
- [35] C. Mounir, U. T. Schwarz, I. L. Koslow, M. Kneissl, T. Wernicke, T. Schimpke, and M. Strassburg, “Impact of inhomogeneous broadening on optical polarization of high-inclination semipolar and nonpolar In $_x$ Ga $_{1-x}$ N/Ga $\bar{N}$  quantum wells,” *Phys. Rev. B*, vol. 93, p. 235 314, 23 Jun. 2016. DOI: [10.1103/PhysRevB.93.235314](https://link.aps.org/doi/10.1103/PhysRevB.93.235314). [Online]. Available: <https://link.aps.org/doi/10.1103/PhysRevB.93.235314>.
- [36] J. Shao, L. Tang, C. Edmunds, G. Gardner, O. Malis, and M. Manfra, “Surface morphology evolution of m-plane (11 $\bar{0}0$ ) gan during molecular beam epitaxy growth: Impact of Ga/N ratio, miscut direction, and growth temperature,” *Journal of Applied Physics*, vol. 114, no. 2, p. 023 508, 2013. DOI: [10.1063/1.4813079](https://doi.org/10.1063/1.4813079). [Online]. Available: <https://doi.org/10.1063/1.4813079>.

- [37] T. R. Merritt, M. A. Meeker, B. A. Magill, G. A. Khodaparast, S. McGill, J. G. Tischler, S. G. Choi, and C. J. Palmström, “Photoluminescence lineshape and dynamics of localized excitonic transitions in InAsP epitaxial layers,” *Journal of Applied Physics*, vol. 115, no. 19, p. 193 503, 2014. DOI: [10.1063/1.4876121](https://doi.org/10.1063/1.4876121). [Online]. Available: <https://doi.org/10.1063/1.4876121>.
- [38] R. Oliva, S. J. Zelewski, Ł. Janicki, K. R. Gwóźdź, J. Serafińczuk, M. Rudziński, E. Özbay, and R. Kudrawiec, “Determination of the band gap of indium-rich InGaN by means of photoacoustic spectroscopy,” *Semiconductor Science and Technology*, vol. 33, no. 3, p. 035 007, Feb. 2018.
- [39] I. Vurgaftman and J. R. Meyer, “Band parameters for nitrogen-containing semiconductors,” *Journal of Applied Physics*, vol. 94, no. 6, pp. 3675–3696, 2003. DOI: [10.1063/1.1600519](https://doi.org/10.1063/1.1600519). [Online]. Available: <https://doi.org/10.1063/1.1600519>.
- [40] Y. P. Varshni, “Temperature dependence of the energy gap in semiconductors,” *Physica*, vol. 34, pp. 149–154, 1967. DOI: [10.1016/0031-8914\(67\)90062-6](https://doi.org/10.1016/0031-8914(67)90062-6).
- [41] S. Schulz, D. P. Tanner, E. P. O’Reilly, M. A. Caro, T. L. Martin, P. A. J. Bagot, M. P. Moody, F. Tang, J. T. Griffiths, F. Oehler, M. J. Kappers, R. A. Oliver, C. J. Humphreys, D. Sutherland, M. J. Davies, and P. Dawson, “Structural, electronic, and optical properties of  $m$ -plane InGaN/GaN quantum wells: Insights from experiment and atomistic theory,” *Phys. Rev. B*, vol. 92, p. 235 419, 23 Dec. 2015. DOI: [10.1103/PhysRevB.92.235419](https://link.aps.org/doi/10.1103/PhysRevB.92.235419). [Online]. Available: <https://link.aps.org/doi/10.1103/PhysRevB.92.235419>.
- [42] D. S. Arteev, A. V. Sakharov, E. E. Zavarin, W. V. Lundin, A. N. Smirnov, V. Y. Davydov, M. A. Yagovkina, S. O. Usov, and A. F. Tsatsulnikov, “Investigation of statistical broadening in InGaN alloys,” *Journal of Physics: Conference Series*, vol. 1135, p. 012 050, Dec. 2018. DOI: [10.1088/1742-6596/1135/1/012050](https://doi.org/10.1088/1742-6596/1135/1/012050).
- [43] E. F. Schubert, E. O. Göbel, Y. Horikoshi, K. Ploog, and H. J. Queisser, “Alloy broadening in photoluminescence spectra of  $\text{Al}_x\text{Ga}_{1-x}\text{As}$ ,” *Phys. Rev. B*, vol. 30, pp. 813–820, 2 Jul. 1984. DOI: [10.1103/PhysRevB.30.813](https://link.aps.org/doi/10.1103/PhysRevB.30.813). [Online]. Available: <https://link.aps.org/doi/10.1103/PhysRevB.30.813>.
- [44] W. Shan, W. Walukiewicz, E. E. Haller, B. D. Little, J. J. Song, M. D. McCluskey, N. M. Johnson, Z. C. Feng, M. Schurman, and R. A. Stall, “Optical properties of  $\text{In}_x\text{Ga}_{1-x}\text{N}$  alloys grown by metalorganic chemical vapor deposition,” *Journal of Applied Physics*, vol. 84, no. 8, pp. 4452–4458, 1998. DOI: [10.1063/1.368669](https://doi.org/10.1063/1.368669). [Online]. Available: <https://doi.org/10.1063/1.368669>.



- [45] C. Zhao, R. Zhang, B. Liu, D. Fu, H. Chen, M. Li, Z. Xie, X. Xiu, S. Gu, and Y. Zheng, “The temperature dependence of optical properties of InGaN alloys,” *Science China Physics, Mechanics and Astronomy*, vol. 55, no. 3, pp. 396–399, Mar. 2012. DOI: [10.1007/s11433-012-4651-7](https://doi.org/10.1007/s11433-012-4651-7). [Online]. Available: <https://doi.org/10.1007/s11433-012-4651-7>.
- [46] H. Wang, Z. Ji, S. Qu, G. Wang, Y. Jiang, B. Liu, X. Xu, and H. Mino, “Influence of excitation power and temperature on photoluminescence in InGaN/GaN multiple quantum wells,” *Opt. Express*, vol. 20, no. 4, pp. 3932–3940, Feb. 2012. DOI: [10.1364/OE.20.003932](https://doi.org/10.1364/OE.20.003932). [Online]. Available: <http://www.opticsexpress.org/abstract.cfm?URI=oe-20-4-3932>.
- [47] S. F. Chichibu, A. Uedono, T. Onuma, B. A. Haskell, A. Chakraborty, T. Koyama, P. T. Fini, S. Keller, S. P. DenBaars, J. S. Speck, U. K. Mishra, S. Nakamura, S. Yamaguchi, S. Kamiyama, H. Amano, I. Akasaki, J. Han, and T. Sota, “Origin of defect-insensitive emission probability in in-containing (Al,In,Ga)N alloy semiconductors,” *Nature. Mater.*, vol. 5, pp. 810–816, Sep. 2006. DOI: [10.1038/nmat1726](https://doi.org/10.1038/nmat1726).
- [48] Y.-H. Cho, G. H. Gainer, A. J. Fischer, J. J. Song, S. Keller, U. K. Mishra, and S. P. DenBaars, ““S-shaped” temperature-dependent emission shift and carrier dynamics in InGaN/GaN multiple quantum wells,” *Applied Physics Letters*, vol. 73, no. 10, pp. 1370–1372, 1998. DOI: [10.1063/1.122164](https://doi.org/10.1063/1.122164). [Online]. Available: <https://doi.org/10.1063/1.122164>.
- [49] D. Sutherland, T. Zhu, J. T. Griffiths, F. Tang, P. Dawson, D. Kundys, F. Oehler, M. J. Kappers, C. J. Humphreys, and R. A. Oliver, “Optical studies of non-polar m-plane (1 $\bar{1}$ 00) InGaN/GaN multi-quantum wells grown on freestanding bulk GaN,” *physica status solidi (b)*, vol. 252, no. 5, pp. 965–970, 2015. DOI: [10.1002/pssb.201451563](https://doi.org/10.1002/pssb.201451563). [Online]. Available: <https://onlinelibrary.wiley.com/doi/abs/10.1002/pssb.201451563>.
- [50] T. Zhu, D. Gachet, F. Tang, W. Y. Fu, F. Oehler, M. J. Kappers, P. Dawson, C. J. Humphreys, and R. A. Oliver, “Local carrier recombination and associated dynamics in m-plane InGaN/GaN quantum wells probed by picosecond cathodoluminescence,” *Applied Physics Letters*, vol. 109, no. 23, p. 232 103, 2016. DOI: [10.1063/1.4971366](https://doi.org/10.1063/1.4971366). [Online]. Available: <https://doi.org/10.1063/1.4971366>.
- [51] F. Szmulowicz, M. O. Manasreh, C. E. Stutz, and T. Vaughan, “Temperature and many-body effects on the intersubband transition in a GaAs/Al<sub>0.3</sub>Ga<sub>0.7</sub>As multiple quantum well,” *Phys. Rev. B*, vol. 50, pp. 11 618–11 623, 16 Oct. 1994. DOI: [10.1103/PhysRevB.50.11618](https://doi.org/10.1103/PhysRevB.50.11618). [Online]. Available: <https://link.aps.org/doi/10.1103/PhysRevB.50.11618>.

- [52] S. Marcinkevičius, K. M. Kelchner, S. Nakamura, S. P. DenBaars, and J. S. Speck, “Optical properties of extended and localized states in m-plane InGaN quantum wells,” *Applied Physics Letters*, vol. 102, no. 10, p. 101 102, 2013. DOI: [10.1063/1.4794904](https://doi.org/10.1063/1.4794904). [Online]. Available: <https://doi.org/10.1063/1.4794904>.
- [53] R. Ivanov, S. Marcinkevičius, M. D. Mensi, O. Martinez, L. Y. Kuritzky, D. J. Myers, S. Nakamura, and J. S. Speck, “Polarization-resolved near-field spectroscopy of localized states in  $m$ -plane  $\text{In}_x\text{Ga}_{1-x}\text{N}/\text{GaN}$  quantum wells,” *Phys. Rev. Applied*, vol. 7, p. 064 033, 6 Jun. 2017. DOI: [10.1103/PhysRevApplied.7.064033](https://doi.org/10.1103/PhysRevApplied.7.064033). [Online]. Available: <https://link.aps.org/doi/10.1103/PhysRevApplied.7.064033>.
- [54] T. K. Uždavinyš, D. L. Becerra, R. Ivanov, S. P. DenBaars, S. Nakamura, J. S. Speck, and S. Marcinkevičius, “Influence of well width fluctuations on recombination properties in semipolar InGaN quantum wells studied by time- and spatially-resolved near-field photoluminescence,” *Opt. Mater. Express*, vol. 7, no. 9, pp. 3116–3123, Sep. 2017. DOI: [10.1364/OME.7.003116](https://doi.org/10.1364/OME.7.003116). [Online]. Available: <http://www.osapublishing.org/ome/abstract.cfm?URI=ome-7-9-3116>.
- [55] S. Marcinkevičius, K. M. Kelchner, S. Nakamura, S. P. DenBaars, and J. S. Speck, “Optical properties and carrier dynamics in  $m$ -plane InGaN quantum wells,” *physica status solidi c*, vol. 11, no. 3-4, pp. 690–693, 2014. DOI: [10.1002/pssc.201300430](https://doi.org/10.1002/pssc.201300430). [Online]. Available: <https://onlinelibrary.wiley.com/doi/abs/10.1002/pssc.201300430>.
- [56] K. M. Kelchner, L. Y. Kuritzky, K. Fujito, S. Nakamura, S. P. DenBaars, and J. S. Speck, “Emission characteristics of single InGaN quantum wells on misoriented non-polar  $m$ -plane bulk GaN substrates,” *Journal of Crystal Growth*, vol. 382, pp. 80–86, 2013, ISSN: 0022-0248. DOI: <https://doi.org/10.1016/j.jcrysgro.2013.08.013>. [Online]. Available: <http://www.sciencedirect.com/science/article/pii/S002202481300554X>.
- [57] M. Sawicka, P. Wolny, M. Kryśko, H. Turski, K. Szkudlarek, S. Grzanka, and C. Skierbiszewski, “Comparative study of semipolar  $(202\bar{1})$ , nonpolar  $(101\bar{0})$  and polar  $(0001)$  InGaN multi-quantum well structures grown under N- and In-excess by plasma assisted molecular beam epitaxy,” *Journal of Crystal Growth*, vol. 465, pp. 43–47, 2017, ISSN: 0022-0248. DOI: <https://doi.org/10.1016/j.jcrysgro.2017.02.045>. [Online]. Available: <http://www.sciencedirect.com/science/article/pii/S0022024817301252>.
- [58] P. Dawson, S. Schulz, R. A. Oliver, M. J. Kappers, and C. J. Humphreys, “The nature of carrier localisation in polar and nonpolar InGaN/GaN quantum wells,” *Journal of Applied Physics*, vol. 119, no. 18, p. 181 505, 2016. DOI: [10.1063/1.4948237](https://doi.org/10.1063/1.4948237). [Online]. Available: <https://doi.org/10.1063/1.4948237>.



- [59] S. Kusanagi, Y. Kanitani, Y. Kudo, K. Tasai, A. A. Yamaguchi, and S. Tomiya, “InGaN quantum wells with improved photoluminescence properties through strain-controlled modification of the InGaN underlayer,” *Japanese Journal of Applied Physics*, vol. 58, no. SC, SCCB28, May 2019. DOI: [10.7567/1347-4065/ab0f11](https://doi.org/10.7567/1347-4065/ab0f11).
- [60] A. Pesach, E. Gross, C.-Y. Huang, Y.-D. Lin, A. Vardi, S. E. Schacham, S. Nakamura, and G. Bahir, “Non-polar m-plane intersubband based InGaN/(Al)GaN quantum well infrared photodetectors,” *Applied Physics Letters*, vol. 103, no. 2, p. 022 110, 2013. DOI: [10.1063/1.4813395](https://doi.org/10.1063/1.4813395). [Online]. Available: <https://doi.org/10.1063/1.4813395>.
- [61] A. Hospodková, J. Oswald, M. Zíková, J. Pangrác, K. Kuldová, K. Blažek, G. Ledoux, C. Dujardin, and M. Nikl, “On the correlations between the excitonic luminescence efficiency and the QW numbers in multiple InGaN/GaN QW structure,” *Journal of Applied Physics*, vol. 121, no. 21, p. 214 505, 2017. DOI: [10.1063/1.4984908](https://doi.org/10.1063/1.4984908). [Online]. Available: <https://doi.org/10.1063/1.4984908>.
- [62] M. Zíková, A. Hospodková, J. Pangrác, T. Hubáček, J. Oswald, K. Kuldová, F. Hájek, G. Ledoux, and C. Dujardin, “Influence of Si doping of GaN layers surrounding InGaN quantum wells on structure photoluminescence properties,” *Journal of Crystal Growth*, vol. 506, pp. 8–13, 2019, ISSN: 0022-0248. DOI: <https://doi.org/10.1016/j.jcrysgro.2018.10.013>. [Online]. Available: <http://www.sciencedirect.com/science/article/pii/S0022024818304998>.
- [63] A. Hospodková, M. Nikl, O. Pacherová, J. Oswald, P. Brůža, D. Pánek, B. Foltynski, E. Hulicius, A. Beitlerová, and M. Heuken, “InGaN/GaN multiple quantum well for fast scintillation application: Radioluminescence and photoluminescence study,” *Nanotechnology*, vol. 25, no. 45, p. 455 501, Oct. 2014. DOI: [10.1088/0957-4484/25/45/455501](https://doi.org/10.1088/0957-4484/25/45/455501).
- [64] N. Ben sedrine, T. Esteves, J. Rodrigues, L. Rino, M. Correia, M. Sequeira, A. Neves, E. Alves, M. Bockowski, P. R Edwards, K. O'Donnell, K. Lorenz, and T. Monteiro, “Photoluminescence studies of a perceived white light emission from a monolithic InGaN/GaN quantum well structure,” *Scientific Reports*, vol. 5, p. 13 739, Sep. 2015. DOI: [10.1038/srep13739](https://doi.org/10.1038/srep13739).
- [65] S. Marcinkevičius, K. M. Kelchner, L. Y. Kuritzky, S. Nakamura, S. P. DenBaars, and J. S. Speck, “Photoexcited carrier recombination in wide m-plane InGaN/GaN quantum wells,” *Applied Physics Letters*, vol. 103, no. 11, p. 111 107, 2013. DOI: [10.1063/1.4820839](https://doi.org/10.1063/1.4820839). [Online]. Available: <https://doi.org/10.1063/1.4820839>.
- [66] V. Liuolia, S. Marcinkevičius, Y.-D. Lin, H. Ohta, S. P. DenBaars, and S. Nakamura, “Dynamics of polarized photoluminescence in m-plane InGaN/GaN quantum wells,” *Journal of Applied Physics*, vol. 108, no. 2, p. 023 101, 2010. DOI: [10.1063/1.3460278](https://doi.org/10.1063/1.3460278). [Online]. Available: <https://doi.org/10.1063/1.3460278>.

- [67] A. Pinos, S. Marcinkevičius, J. Yang, Y. Bilenko, M. Shatalov, R. Gaska, and M. S. Shur, "Aging of AlGa<sub>N</sub> quantum well light emitting diode studied by scanning near-field optical spectroscopy," *Applied Physics Letters*, vol. 95, no. 18, p. 181 914, 2009. DOI: [10.1063/1.3262964](https://doi.org/10.1063/1.3262964). [Online]. Available: <https://doi.org/10.1063/1.3262964>.
- [68] Y. Xing, L. Wang, D. Yang, Z. Wang, Z. Hao, C. Sun, B. Xiong, Y. Luo, Y. Han, J. Wang, and H. Li, "A novel model on time-resolved photoluminescence measurements of polar InGa<sub>N</sub>/Ga<sub>N</sub> multi-quantum-well structures," *Scientific Reports*, vol. 7, p. 45 082, 2017. DOI: [10.1038/srep45082](https://doi.org/10.1038/srep45082).
- [69] Y. Iwata, R. G. Banal, S. Ichikawa, M. Funato, and Y. Kawakami, "Emission mechanisms in Al-rich AlGa<sub>N</sub>/Al<sub>N</sub> quantum wells assessed by excitation power dependent photoluminescence spectroscopy," *Journal of Applied Physics*, vol. 117, no. 7, p. 075 701, 2015. DOI: [10.1063/1.4908282](https://doi.org/10.1063/1.4908282). [Online]. Available: <https://doi.org/10.1063/1.4908282>.
- [70] C. H. Chiu, S. Y. Kuo, M. H. Lo, C. C. Ke, T. C. Wang, Y. T. Lee, H. C. Kuo, T. C. Lu, and S. C. Wang, "Optical properties of a-plane InGa<sub>N</sub>/Ga<sub>N</sub> multiple quantum wells on r-plane sapphire substrates with different indium compositions," *Journal of Applied Physics*, vol. 105, no. 6, p. 063 105, 2009. DOI: [10.1063/1.3083074](https://doi.org/10.1063/1.3083074). [Online]. Available: <https://doi.org/10.1063/1.3083074>.
- [71] S. J. Xu, L. X. Zheng, S. H. Cheung, M. H. Xie, S. Y. Tong, and H. Yang, "Comparative study on the broadening of exciton luminescence linewidth due to phonon in zinc-blende and wurtzite Ga<sub>N</sub> epilayers," *Applied Physics Letters*, vol. 81, no. 23, pp. 4389–4391, 2002. DOI: [10.1063/1.1526450](https://doi.org/10.1063/1.1526450). [Online]. Available: <https://doi.org/10.1063/1.1526450>.
- [72] P. G. Eliseev, P. Perlin, J. Lee, and M. Osiniński, "'blue" temperature-induced shift and band-tail emission in InGa<sub>N</sub>-based light sources," *Applied Physics Letters*, vol. 71, no. 5, pp. 569–571, 1997. DOI: [10.1063/1.119797](https://doi.org/10.1063/1.119797). [Online]. Available: <https://doi.org/10.1063/1.119797>.
- [73] V. Liuolia, A. Pinos, S. Marcinkevičius, Y. D. Lin, H. Ohta, S. P. DenBaars, and S. Nakamura, "Carrier localization in m-plane InGa<sub>N</sub>/Ga<sub>N</sub> quantum wells probed by scanning near field optical spectroscopy," *Applied Physics Letters*, vol. 97, no. 15, p. 151 106, 2010. DOI: [10.1063/1.3502482](https://doi.org/10.1063/1.3502482). [Online]. Available: <https://doi.org/10.1063/1.3502482>.
- [74] V. Liuolia, S. Marcinkevičius, A. Pinos, R. Gaska, and M. S. Shur, "Dynamics of carrier recombination and localization in AlGa<sub>N</sub> quantum wells studied by time-resolved transmission spectroscopy," *Applied Physics Letters*, vol. 95, no. 9, p. 091 910, 2009. DOI: [10.1063/1.3222972](https://doi.org/10.1063/1.3222972). [Online]. Available: <https://doi.org/10.1063/1.3222972>.

- [75] T. Lin, H. C. Kuo, X. D. Jiang, and Z. C. Feng, “Recombination pathways in green InGa<sub>N</sub>/Ga<sub>N</sub> multiple quantum wells,” *Nanoscale Research Letters*, vol. 12, p. 137, 2017. DOI: [10.1186/s11671-017-1922-2](https://doi.org/10.1186/s11671-017-1922-2).
- [76] M. Pophristic, F. H. Long, C. Tran, I. T. Ferguson, and R. F. Karlicek, “Time-resolved photoluminescence measurements of quantum dots in InGa<sub>N</sub> multiple quantum wells and light-emitting diodes,” *Journal of Applied Physics*, vol. 86, no. 2, pp. 1114–1118, 1999. DOI: [10.1063/1.370865](https://doi.org/10.1063/1.370865). [Online]. Available: <https://doi.org/10.1063/1.370865>.
- [77] E. Berkowicz, D. Gershoni, G. Bahir, E. Lakin, D. Shilo, E. Zolotoyabko, A. C. Abare, S. P. Denbaars, and L. A. Coldren, “Measured and calculated radiative lifetime and optical absorption of In<sub>x</sub>Ga<sub>1-x</sub>N/GaN quantum structures,” *Phys. Rev. B*, vol. 61, pp. 10 994–11 008, 16 Apr. 2000. DOI: [10.1103/PhysRevB.61.10994](https://doi.org/10.1103/PhysRevB.61.10994). [Online]. Available: <https://link.aps.org/doi/10.1103/PhysRevB.61.10994>.
- [78] O. Brandt, H. Yang, and K. H. Ploog, “Impact of recombination centers on the spontaneous emission of semiconductors under steady-state and transient conditions,” *Phys. Rev. B*, vol. 54, R5215–R5218, 8 Aug. 1996. DOI: [10.1103/PhysRevB.54.R5215](https://doi.org/10.1103/PhysRevB.54.R5215). [Online]. Available: <https://link.aps.org/doi/10.1103/PhysRevB.54.R5215>.
- [79] M. Shahmohammadi, W. Liu, G. Rossbach, L. Lahourcade, A. Dussaigne, C. Bougerol, R. Butté, N. Grandjean, B. Deveaud, and G. Jacopin, “Enhancement of auger recombination induced by carrier localization in ingan/gan quantum wells,” *Phys. Rev. B*, vol. 95, p. 125 314, 12 Mar. 2017. DOI: [10.1103/PhysRevB.95.125314](https://doi.org/10.1103/PhysRevB.95.125314). [Online]. Available: <https://link.aps.org/doi/10.1103/PhysRevB.95.125314>.
- [80] P. Corfdir, J. Levrat, A. Dussaigne, P. Lefebvre, H. Teisseyre, I. Grzegory, T. Suski, J.-D. Ganière, N. Grandjean, and B. Deveaud-Plédran, “Intrinsic dynamics of weakly and strongly confined excitons in nonpolar nitride-based heterostructures,” *Phys. Rev. B*, vol. 83, p. 245 326, 24 Jun. 2011. DOI: [10.1103/PhysRevB.83.245326](https://doi.org/10.1103/PhysRevB.83.245326). [Online]. Available: <https://link.aps.org/doi/10.1103/PhysRevB.83.245326>.
- [81] P. Corfdir, J. Levrat, G. Rossbach, R. Butté, E. Feltn, J.-F. Carlin, G. Christmann, P. Lefebvre, J.-D. Ganière, N. Grandjean, and B. Deveaud-Plédran, “Impact of biexcitons on the relaxation mechanisms of polaritons in iii-nitride based multiple quantum well microcavities,” *Phys. Rev. B*, vol. 85, p. 245 308, 24 Jun. 2012. DOI: [10.1103/PhysRevB.85.245308](https://doi.org/10.1103/PhysRevB.85.245308). [Online]. Available: <https://link.aps.org/doi/10.1103/PhysRevB.85.245308>.
- [82] C. Haller, J.-F. Carlin, G. Jacopin, D. Martin, R. Butté, and N. Grandjean, “Burying non-radiative defects in InGa<sub>N</sub> underlayer to increase InGa<sub>N</sub>/Ga<sub>N</sub> quantum well efficiency,” *Applied Physics Letters*, vol. 111, no. 26, p. 262 101, 2017. DOI: [10.1063/1.5007616](https://doi.org/10.1063/1.5007616). [Online]. Available: <https://doi.org/10.1063/1.5007616>.

- [83] P. Pramanik, S. Sen, C. Singha, A. S. Roy, A. Das, S. Sen, A. Bhattacharyya, D. Kumar, and D. Sridhara Rao, “Controlling the compositional inhomogeneities in  $\text{Al}_x\text{Ga}_{1-x}\text{N}/\text{Al}_y\text{Ga}_{1-y}\text{N}$  MQWs grown by PA-MBE: Effect on luminescence properties,” *Journal of Crystal Growth*, vol. 439, pp. 60–65, 2016, ISSN: 0022-0248. DOI: <https://doi.org/10.1016/j.jcrysgro.2016.01.004>. [Online]. Available: <https://www.sciencedirect.com/science/article/pii/S002202481600018X>.
- [84] T. M. Al tahtamouni, A. Sedhain, J. Y. Lin, and H. X. Jiang, “Si-doped high Al-content AlGa<sub>N</sub> epilayers with improved quality and conductivity using indium as a surfactant,” *Applied Physics Letters*, vol. 92, no. 9, p. 092105, 2008. DOI: [10.1063/1.2890416](https://doi.org/10.1063/1.2890416). [Online]. Available: <https://doi.org/10.1063/1.2890416>.
- [85] Q. Dai, X. Zhang, Z. Liang, G. Yang, Z. Wu, S. Chen, J. Zhao, C. Meng, J. Wang, and Y. Cui, “Effects of indium surfactant on growth and characteristics of (11 $\bar{2}$ 2) plane AlGa<sub>N</sub>-based multiple quantum wells,” *Opt. Mater. Express*, vol. 8, no. 1, pp. 24–29, Jan. 2018. DOI: [10.1364/OME.8.000024](https://doi.org/10.1364/OME.8.000024). [Online]. Available: <http://www.osapublishing.org/ome/abstract.cfm?URI=ome-8-1-24>.

## A. PL MEASUREMENT SETUP

### A.1 Sample placement

The sample is mounted on the sample holder as shown in Figure A.1. The active region needs to be put upside. Screw A is for mounting the sample, while screw B is for insuring that the thermal sensor is attached to the sample holder firmly.

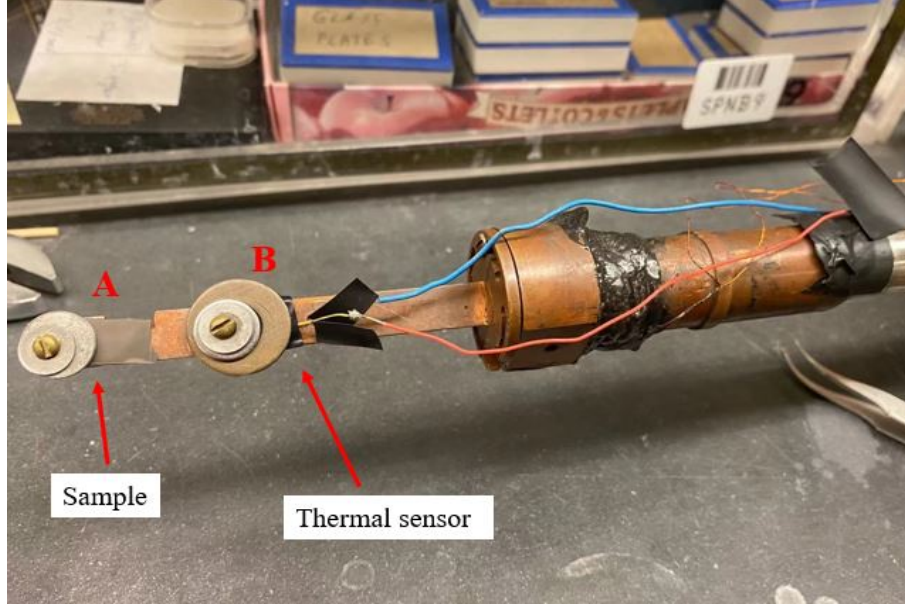


**Figure A.1.** A sample is mounted on the sample holder.

### A.2 Steady state PL measurement

The PL setup is shown in Figure A.2. The following measurement steps will be described based on the use of laser as the excitation source for PL measurement at low temperatures. If the Xenon lamp is used, the steps are similar.

1. Mount the sample and put it in the cryostat. Then mount the cryostat as shown in Figure A.2;
2. Turn on the laser and adjust the mirrors to insure the laser is shed on the sample;

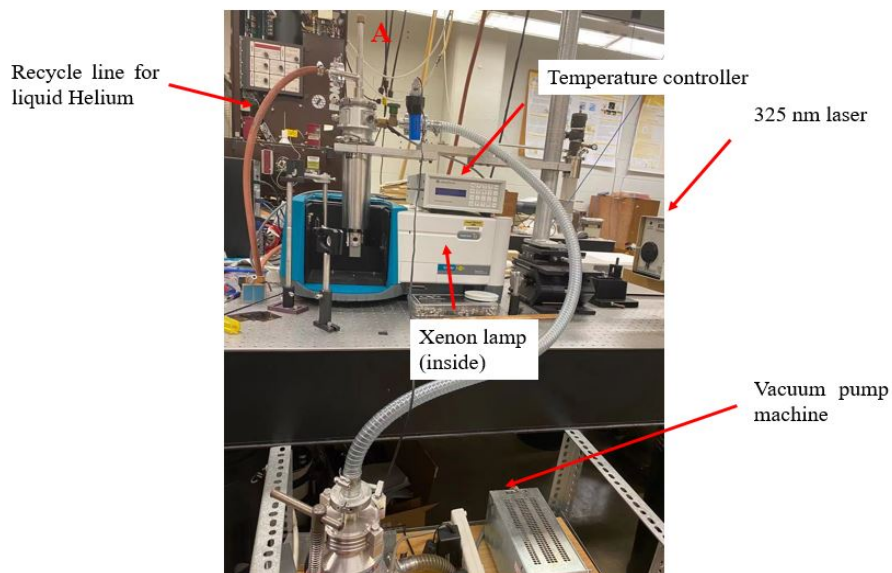


**Figure A.2.** The setup for steady state PL measurement.

3. Rotate the sample holder to align the sample placement. The reflection light from the laser should be avoided to be collected by the detector. Based on the experience, the placement in Figure A.3 can guarantee best PL collection. If the Xenon lamp is used, this step is not necessary;

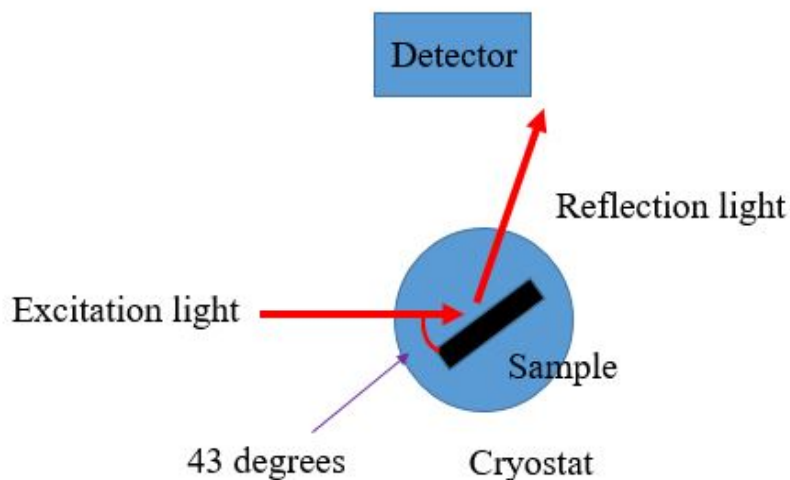


**Figure A.3.** Empirical sample placement.



4. Seal the cryostat and connect the temperature controller to the port shown in Figure [A.4](#);

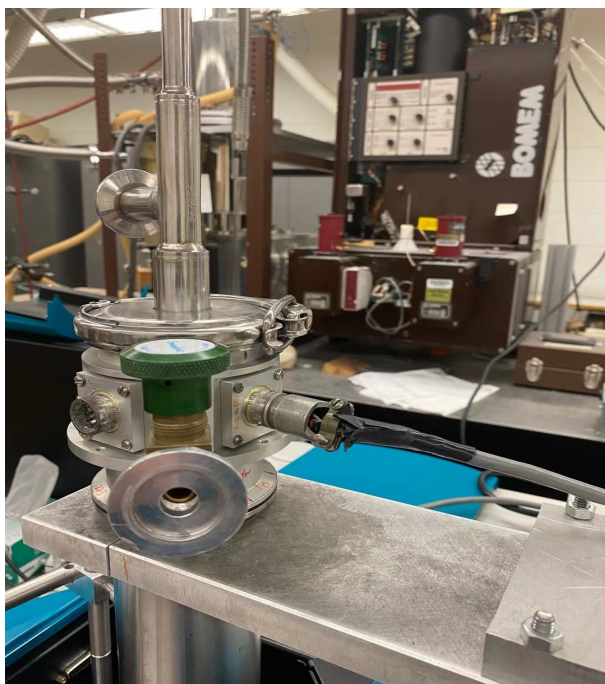


**Figure A.4.** Connection of the temperature controller.

5. Vacuum the system;
6. Cool down the system using liquid Helium or liquid Nitrogen. Then use the temperature controller to set the temperature of the sample;
7. Choose function "Bio/Chemi-luminescence" in software "Scan". Then set appropriate scan range, emission slit, scan rate and gate time.
8. Turn off the room light, and then run the software to collect the PL spectrum;

## VITA

### EDUCATION:

Phd in Physics	Purdue University	2021
MS in Physics	Purdue University	2019
BS Honors in Applied Physics	Xi'an Jiaotong University	2015

### PUBLICATIONS:

1. Brandon Dzuba, Trang Nguyen, Yang Cao, Rosa E. Diaz, Michael J. Manfra, Oana Malis, "Overcoming anomalous suppression of m-plane AlGa<sub>N</sub> growth by molecular-beam epitaxy using indium as a surfactant", Journal of Applied Physics. 130(2021) 105702.
2. Trang Nguyen, Brandon Dzuba, Yang Cao, Alexander Senichev, Rosa Diaz, Michael Manfra, and Oana Malis, "Mid-infrared intersubband absorption in strain-balanced non-polar (In)AlGa<sub>N</sub>/InGa<sub>N</sub> multi-quantum wells", Optical Material Express. 11(2021) 3284.
3. Brandon Dzuba, Alexander Senichev, Trang Nguyen, Yang Cao, Rosa Diaz, Michael Manfra, and Oana Malis, "Indium Surfactant Assisted Epitaxy of Non-polar (10 $\bar{1}0$ ) AlGa<sub>N</sub>/InGa<sub>N</sub> Multiple Quantum Well Heterostructures", Journal of Applied Physics. 128(2020) 115701.
4. Yang Cao, Brandon Dzuba, Brenden Magill, Alexander Senichev, Trang Nguyen, Rosa Diaz, Michael Manfra, Stephen McGill, Carlos Garcia, Giti Khodaparast, and Oana Malis, "Photoluminescence study of non-polar m-plane InGa<sub>N</sub> and nearly strain-balanced InGa<sub>N</sub>/AlGa<sub>N</sub> superlattices", Journal of Applied Physics. 127(2020) 185702.
5. Alexander Senichev, Brandon Dzuba, Trang Nguyen, Yang Cao, Michael A. Capano, Michael J. Manfra, and Oana Malis, "Impact of growth conditions and strain on Indium incorporation in non-polar m-plane (10 $\bar{1}0$ ) InGa<sub>N</sub> grown by plasma-assisted molecular beam epitaxy", APL Materials. 7(2019) 121109.



6. Xuejing Wang, Trang Nguyen, Yang Cao, Jie Jian, Oana Malis, and Haiyan Wang, “AlN-based hybrid thin films with self-assembled plasmonic Au and Ag nanoinclusions”, *Applied Physics Letter*. 114(2019) 023103.
7. Alexander Senichev, Trang Nguyen, Rosa E Diaz, Brandon Dzuba, Mohammadali Shirazi, Yang Cao, Michael J Manfra, and Oana Malis, “Evolution of Indium segregation in metal-polar In<sub>0.17</sub>Al<sub>0.83</sub>N lattice-matched to GaN grown by plasma assisted molecular beam epitaxy”, *Journal of Crystal Growth*. 500(2018) 52-57.
8. Trang Nguyen, MohammadAli Shirazi-Hosseini-Dokht, Yang Cao, Rosa E. Diaz, Geoffrey C. Gardner, Michael J. Manfra, and Oana Malis, “Intersubband Transitions in Nonpolar m-Plane AlGa<sub>N</sub>/Ga<sub>N</sub> Heterostructures”, *Physica Status Solidi A*. 215(2018) 1700828.

#### **PRESENTATIONS:**

1. "Photoluminescence study of non-polar m-plane InGa<sub>N</sub> and near strain-balanced AlGa<sub>N</sub>/InGa<sub>N</sub> superlattices", American Physical Society March Meeting (March 2020)
2. "Photoluminescence study of non-polar m-plane InGa<sub>N</sub> and near strain-balanced AlGa<sub>N</sub>/InGa<sub>N</sub> superlattices", 62nd Electronic Materials Conference (June 2020)
3. "Photoluminescence study of carrier localization and recombination in nearly strain-balanced non-polar m-plane InGa<sub>N</sub>/AlGa<sub>N</sub> superlattices", American Physical Society March Meeting (March 2021)